DEFORMABLE MODEL AND ITS APPLICATION IN ANATOMY GUIDED CORTICAL RECONSTRUCTION OF MR IMAGE OF BRAIN

Thesis submitted by **Somojit Saha** for the fulfilment of the degree of

DOCTOR OF PHILOSOPHY (Engineering)

Department of Computer Science & Engineering
Faculty Council of Engineering and Technology
Jadavpur University
Kolkata-700032, India

November, 2015

DEFORMABLE MODEL AND ITS APPLICATION IN ANATOMY GUIDED CORTICAL RECONSTRUCTION OF MR IMAGE OF BRAIN

Thesis submitted for the fulfilment of the degree of

DOCTOR OF PHILOSOPHY (Engineering)

Jadavpur University

by

Somojit Saha

Under the supervision of

Prof. Avijit Kar
Department of Computer Science & Engineering,
Jadavpur University,
Kolkata, West Bengal - 700032

Prof. Sarit Kumar Das
Director, IIT Ropar, Punjab-140001
Former Professor of Department of Mechanical Engineering, IIT Madras
Chennai - 600036

November, 2015

JADAVPUR UNIVERSITY

KOLKATA – 700032, INDIA

INDEX No. 173/09/E

1. Title of the Thesis:

DEFORMABLE MODEL AND ITS APPLICATION IN ANATOMY GUIDED CORTICAL RECONSTRUCTION OF MR IMAGE OF BRAIN

2. Name Designation & Institution of the Supervisor:

Dr. Avijit Kar
Professor
Department of Computer Science & Engineering
Jadavpur University
Jadavpur, West Bengal - 700032, India

Dr. Sarit Kumar Das

Director
Department of Mechanical Engineering,
Indian Institute of Technology Ropar
Punjab - 140001, India

Former Professor of Department of Mechanical Engineering,
IIT Madras, Chennai - 600036

3. List of Publications of the Author Related to the Thesis

International Conference

[1] "Accurate cortical reconstruction in narrow sulci with a novel external force field"; *17th International Conference on Medical Image Processing and Analysis 2015, WASET, Dubai, UAE (Accepted)*

[2] "Anatomy guided hybrid deformable model for reconstruction of brain cortex from MR image"; *CompBio'10, IASTED Technology Conference 2010, Cambridge, Massachusetts, USA*

[3] "High Resolution MR Image of Brain With Signal Attenuation of Gray Matter"; *IST 2010, IEEE Instrumentation and Measurement Society, Thessaloniki, Greece*

[4] "A New Segmentation Technique for Brain and Head from High Resolution MR Image Using Unique Histogram Features", *IPTA2010 (IEEE & EURASIP), Paris, France*

[5] "Segmentation of MR Image of Brain: A New Method Using Unique Histogram Features and Prior Knowledge of Brain Anatomy", *IPCV 2010, WORLDCOMP, Las Vegas, Nevada, USA*

[6] "An improved algorithm for automated segmentation of the head contour from MR image", *VIIP 2009, IASTED Cambridge, UK*

Communicated to International Conference

[1] "A novel external force for propagation of deformable contour into deep sulci of brain for fully automated cortical reconstruction from MR image", *BIOIMAGING 2016 (SCITEPRESS digital library), Rome, Italy*

Communicated to International Journal

[1] "Gray Matter Attenuated Inversion Recovery (GrAIR) for High Contrast MR Image of Brain"; *Journal of Magnetic Resonance Imaging, Wiley online library, Online ISSN: 1522-2586*

4. List of Patents

Nil

5. List of Presentations in International Conferences

[1] "Anatomy guided hybrid deformable model for reconstruction of brain cortex from MR image"; *CompBio'10, IASTED Technology Conference 2010, Cambridge, Massachusetts, USA*

[2] "An improved algorithm for automated segmentation of the head contour from MR image", *VIIP 2009, IASTED Cambridge, UK*

CERTIFICATE FROM THE SUPERVISORS

*This is to certify that the thesis, entitiled "**DEFORMABLE MODEL AND ITS APPLICATION IN ANATOMY GUIDED CORTICAL RECONSTRUCTION OF MR IMAGE OF BRAIN**", submitted by Somojit Saha, M.B.B.S., who got his name registered (**Reg. No.D-7/E/110/09**) on 16th February, 2009, for the award of Ph.D. (Engineering) degree of Jadavpur University is absolutely based upon his own work under our supervision and that neither his thesis nor any part of the thesis has been submitted for any degree/diploma or any other academic award anywhere before.*

1. _____

Signature of the Supervisor

and date with Office Seal

2. _____

Signature of the Supervisor

and date with Office Seal

Acknowledgements

First of all I would like to thank my mentor, Prof. Dr. Avijit Kar for supervising my research and for giving me the opportunity to work with him. I am grateful to him for supporting not only my work but also helping me at every moment whenever I face any doubts throughout this journey.

I would like to thank my co-advisor, Prof. Dr. Sarit Kumar Das for his great help during my research. He was always with me to give wise and encouraging advices when needed.

I express my gratitude to Rohit Kamal Chatterjee, Assistant Professor, B.I.T. Meshra, Kolkata Centre for giving time and attention to my work and also for his relevant comments and encouraging compliments.

I should not forget to thank Satyaki Bhattacharya, Ph.D. scholar at Notre Dame University, U.S.A. for his precious help in my research work.

A special thank to people without whom this Ph.D. would not be possible. First of all, I would like to thank Prof. Chandan Mazumder for being more than a teacher during this period of doubts. I would like to thank Amal Chakraborty for his kindness and great support to motivate us to overcome the hurdle with patience in any situation. Thank you for your support and friendship that turned this difficult period into a positive one.

I take this opportunity to thank all my family specially my cousins Debodatta Saha and Debojit Saha for their influence and support in my life that made the man I am today.

I also express my gratitude to ER & IPR, DRDO, Govt. of India for funding most of the research of this thesis.

I am also grateful to Defence Research and Development Organization (DRDO), Govt. of India for financial support for the present work.

And last but not the least, I thank my friends and juniors from CDC lab and BHW lab that made easier this journey in daily life: Pramila Pradhan, Dr. T. L. Rajak, Sayan, Chayan, Subhajit Das, Avisek Sen, Anirban Sengupta, Subhasis Barman. I apologize to everyone whose names I forgot to mention.

Thank you everyone.

Somojit Saha
November,2015
Jadavpur, W.B., India
PIN 700 032

Abstract

Reconstruction of cerebral cortex or its parametric representation from MR image is on one hand, a challenging problem in computational neuroanatomy, on the other hand its an extremely important tool in diverse applications. Complete parametric description of the cortical boundaries using model-free, low level image processing techniques produce inefficient results because of inherent biological intricacies and attributes of image acquisition. While many acceptable and encouraging results have been obtained using deformable model-based approach, a fully automatic and standard algorithm with accurate outcome is still an open area of research. The focus of this dissertation is to investigate hybridization of the existing deformable models with extensive use of the knowledge of neuroanatomy to meet the target of *full automation* with *minimum computation* and highly *accurate* cortical reconstruction for such applications as functional mapping or morphometric analysis. Shortcomings of the proposed models for cortical reconstruction in the available literature include varied amount of human interaction, approximations and assumptions, heuristic tuning of several parameters and above all, the questionability of true representation of the cortical surface.

In this research, one of my main contributions is optimization of image acquisition parameters for improved image quality, reducing computational burden in post-hoc processing. My other contribution is a novel Advanced Anatomy Guided Hybrid Deformable (AAGHD) model for cortical reconstruction. There are four major contributing factors in this model. First, there is hybridization of different existing deformable models as well as hybridization of low level and high level processing techniques. Second, the model is fully automatic, starting with initialization of the deformable contour progressing through various stages even into the deepest sulcul folds. Third, a novel external force field has been designed overcoming the problem of partial volume effect, especially at narrow, deep sulcul folds. Fourth, the reconstructed cortical boundary converges completely with CSF/Gray matter interface i.e. the true cortical boundary. Our model has been validated on real MR images of brain from various 1.5 T MR scanners.

CONTENT

PART VI – CONCLUSION

List of Figure

List of Table

PART I
INTRODUCTION

CHAPTER 1

INTRODUCTION

CONTENTS

1.1 Deformable Models and its Necessity

Deformable models, introduced in computer vision by Terzopoulos *et al.* [1, 2, 3] are physics-based techniques which have been used extensively in the medical image processing because of their unique capacity for extracting image information, incorporating a priori knowledge as well to accomplish given objectives with great fineness. In this approach a flexible boundary model is placed automatically or manually in the vicinity of the structure to be segmented, and the model is allowed to evolve iteratively to fit the contour of the structure with some explicit converging criterion. Deformable models have been conceptualized from Lagrangian models of solids which follow Hamilton's principle for monogenic systems for which all forces are (except the forces of constraint) derivable from a generalized scalar potential that may be function of the coordinates, velocities and time [4]. As Lagrangian models of solids complement Eulerian models of fluids in continuum mechanics, similarly, parametric deformable models complement its geometric counterparts by means of level set method [2, 5] or elastic or fluid transformation models [6] in continuum mechanical analysis. After initialization, deformable model evolves as a function of local image properties, intrinsic constraints and a priori knowledge of the target object and it mimics various generic behaviour of natural non-rigid materials in response to applied forces, such as continuity, smoothness, elasticity etc. In this approach, the parameters of standard geometric primitives become generalized coordinates in Lagrangian formulations that govern their automatic evolution in response to simulated forces [7]. The name of this physics-based model roots from the use of elastic theory at a physical level. Actually, initial deformable contour

simulates an elastic model of a continuous, flexible contour which is imposed upon an image to match an object boundary. By varying elastic parameters, the strength of prior assumptions can be controlled. These models are subjected to external forces that impose constraints derived from image data and they actively shape and move models to achieve maximal consistency with imaged objects of interest. In medical image analysis, deformable model is highly useful in segmenting, matching and tracking anatomic structures by exploiting constraints derived from the image data along with a priori knowledge about the location, size and shape of these structures. In the area of image segmentation, deformable model can be regarded as a problem of boundary mapping, that is, mathematical description of object boundaries from the images. Deformable model can also be applied directly in motion tracking, shape modelling, object recognition, image registration and warping though image segmentation is fundamental to all such applications.

Segmentation can be regarded as the task of image partitioning into regions based on specified homogeneity criteria. In medical imaging, the segmentation of anatomic structures is partitioning of the original set of image points into subsets corresponding to meaningful anatomic regions and their surroundings. These tasks require the anatomic structures in the original image to be reduced to a compact, analytic representation of their shapes. In medical imaging, automated delineation of different image components is used for analyzing anatomical structure and tissue types, spatial distribution of function and activity, and identification of pathological regions. Segmentation can also be used as an initial step for visualization and compression [3]. Given the extremely complicated nature of segmentation in general and its pivotal role in image processing, innumerable algorithms have been developed. Typically, segmentation of an object is achieved either by identifying all pixels or voxels that belong to the object or by locating those that form its boundary. The former is based primarily on the intensity of pixels as well as the texture that can be associated with each pixel. Techniques that locate boundary pixels use the image gradient, which has high values at the edge of objects. The fundamental concepts and techniques used for region-based and edge-based segmentation, include global and adaptive thresholding, watershed segmentation, gradient operators, region growing and multispectral segmentation techniques. Since segmentation requires classification of pixels, it is treated as a pattern recognition problem and addressed with related techniques. One such approach is fuzzy clustering, a technique based on fuzzy models and membership functions. Another approach is neural networks, where the classification is based on distributed nonlinear parallel processing.

Segmenting structures from medical images and reconstructing a compact geometric representation of these structures is difficult because of the sheer size of the datasets and the complexity and variability of the anatomic shapes of interest. Furthermore, the shortcomings typical of sampled data, such as sampling artifacts, spatial aliasing and noise, may cause the boundaries of structures to be indistinct and disconnected. The challenging problem in segmentation is to segment regions with boundary insufficiencies, that is, missing edge or lack of texture contrast between regions of interest (ROIs) and background and also to integrate boundary elements from those regions into a coherent and consistent model of the structure. Traditional low-level image processing techniques that consider only local information can make incorrect assumptions during this integration process and generate infeasible object boundaries. Segmentation using traditional low-level image processing techniques, such as thresholding, region growing, edge detection and mathematical morphology operations require considerable amounts of expert interactive guidance. Furthermore, automating these model-free approaches is difficult because of the shape complexity and variability across individual subjects. In general, the underconstrained nature of the segmentation problem limits the efficacy of approaches that consider local information only. Noise and other image artifacts can produce incorrect regions of boundary discontinuities in objects recovered by these methods [3, 8].

Deformable model-based segmentation scheme provides a mechanism that is considerably different from traditional techniques and pattern recognition methods and largely overcomes many of their limitations. The main reason of their immense popularity in medical image analysis is their robustness, primarily due to the constraints of the models. These connected and continuous geometric models consider an object boundary as a whole and can make use of a priori knowledge of object shape to constrain the segmentation problem. It is particularly suited for segmentation of images that have artifacts, noise and weak boundaries between structures. The inherent continuity and smoothness of the models can compensate for noise, gaps and other irregularities in object boundaries. Furthermore, parametric representations of the models provide compact and analytical description of object shape. These properties lead to an efficient, robust, accurate and reproducible technique for linking sparse or noisy local image features into a complete and consistent model of the object. The most important aspect of segmentation with deformable models is the possibility of incorporating prior information on the shape of the object. Specific shape information can be used when the shapes of the structures of interest are consistent. If shapes are likely to

vary significantly, generic shape constraints are needed. A maximum a posteriori (MAP) formulation and related distributions are used for specific shape constraints, while the level set method and thickness constraints are used for the generic shape constraints. It drastically decreases the labour intensiveness of medical image processing task through automation and increases significantly their reproducibility, while still allowing for interactive guidance or editing by the experts.

1.2 Gross Anatomy of Human Brain

The brain lies in the cranial cavity and is continuous with the spinal cord through the foramen magnum. It is surrounded by three layers of meninges: the dura mater, the archnoid mater and the pia mater. The brain is composed of an inner core of white matter, which is surrounded by an outer covering of gray matter. Certain important masses of gray matter are situated deeply within the white matter, called subcortical gray matter. The cerebrum, the largest part of the brain, consists of two cerebral hemispheres, which are connected by a mass of white matter called the corpus callosum. The surface layer of each hemisphere, the cortex is composed of gray matter. The cerebral cortex is thrown into folds, or gyri, separated by fissures, or sulci. The surface area of the cortex is greatly increased by this means. Most of the cerebral cortex is concealed from view in the walls of the sulci. Although the patterns of the various sulci vary from brain to brain, some are sufficiently constatnt to serve as descriptive landmarks. The deepest sulci are the lateral sulcus (sylvian fissure) and the central sulcus (Rolandic fissure). These two and an imaginary T-shaped line divide the hemisphere into four lobes, named frontal, parietal, occipital and temporal. The lips (opercula) of the lateral culcus can be pulled apart to expose the insula.

The meninges surround the brain and suspend it in the protective jacket provided by the Cerebro Spinal Fluid (CSF). The meninges comprise the tough dura mater or pachymenix (Gr. Thick membrane), and the leptomeninges (Gr. Slender membranes) consisting of the arachnoid mater and pia mater. Between the arachnoid and the pia is the subarachnoid space filled with CSF. Dura mater is tough layer of fibrous tissue, fussed with the inner periosteum of the skull except where it is reflected into the interior of the vault or is stretched scross the skull base. Wherever it separates from the periosteum, the intervening space contains venous sinuses. Two major dural folds extend into the cranial cavity and help to stabilize the brain. These are the falx cerebri and the tentorium cerebelli. The falx cerebri occupies the longitudinal fissure between the cerebral hemispheres. Along the vault of the skull it encloses

the superior sagittal sinus. Its free border contains the inferior sagittal sinus. The crescentic tentorium cerebelli arches like a tent above the posterior cranial fossa, being lifted up by the falx cerebri in the midline. The attached margin of the tentorium encloses the transverse sinuses and the superior petrosal sinuses. The two U-shaped limbs of the tentorium are linked by a sheet of dura, the diaphragm sellae. The arachnoid (Gr. Spidery) is a thin, fibrocellular layer in direct contact with the dura mater. Innumerable arachnoid trabeculae cross the space to reach the pia mater. The pia mater invests the brain closely, following its contours and lining the various sulci. Like the arachnoid, it is fibrocellular.

Fig 1.1: Human brain showing highly convoluted cortical surface
(Courtesy: www.wisegeek.com)

The cavity present within each cerebral hemisphere is called the lateral ventricle. The lateral ventricles communicate with the third ventricle through the interventricular foramina. The principal source of the CSF is the secretion of the choroid plexuses into the ventricles of the brain. From the lateral ventricles, the CSF enters the third ventricle. It descends to the fourth ventricle and then into the subarachnoid space. From the subarachnoid space at the base of the brain, the CSF ascends and bathes the surface of the cerebral hemisphere before

being returned to the blood through the arachnoid granulations, pinhead pouches of arachnoid mater projecting through the dural wall of the major venous sinuses [9, 10].

1.3 MR Image of Brain

MRI is a tomographic imaging technique that produces images of internal physical & chemical characteristics of an object from externally measured NMR signal.Tomography comes from the Greek word Tomas ($\tau o \mu o s$) means 'Cut'. Tomography means creating images of the internal (anatomical or functional) organization of an object without physically cutting open. Tomography imaging principles are rooted in physics, mathematics, computer Science and Engineering. Radon first addressed the Tomography imaging issue in 1917 but it was unnoticed for 50 years. 60s & 70s were the formative years of Tomography, when X Ray Tomography & MRI were developed. Categorically there are three kinds of tomography, namely emission tomography (MRI/PET/SPECT), transmission tomography (acoustic tomography) and diffraction tomography (acoustic tomography). MRI is a form of emission tomography (like PET/ SPECT). It outputs a multidimensional data array (or image) representing spatial distribution of some measured physical quantity like other modalities. Unlike others it produces 2D sectional images at any orientation, 3D volumetric images, or even 4D images presenting Special Spectral distributions. It operates in the RF range, so there is no harmful effect. The most important feature of this technique is richness in information content. Its image pixel value depends on the intrinsic parameters, namely nuclear spin density (ρ), spin – lattice relaxation time (T_1), spin- spin relaxation time (T_2), molecular motions (Diffusion & perfusion), susceptibility effects and chemical shift differences. These parameters can be regulated by another set of operator- selectable parameters.

Imaging process involves two transformations, data collection called imaging equation or forward problems and measured data are processed into image formation, known as image reconstruction equation or inverse problem. Core part of the MRI principle is similarly consists of two aspects, first one is NMR phenomena, observed by Felix Block at Stanford and Edward Purcell at Harvard in 1946 and the second one is image formation using NMR signals by the spatial information encoding principles, called zeumatography, developed by Paul Lauterbur in 1972 [11].

Detail discussion of the principle of MRI is beyond scope of this thesis, still salient features of NMR phenomenon and signal generation is discussed in the Appendix A.

Flow chart for principle of MRI

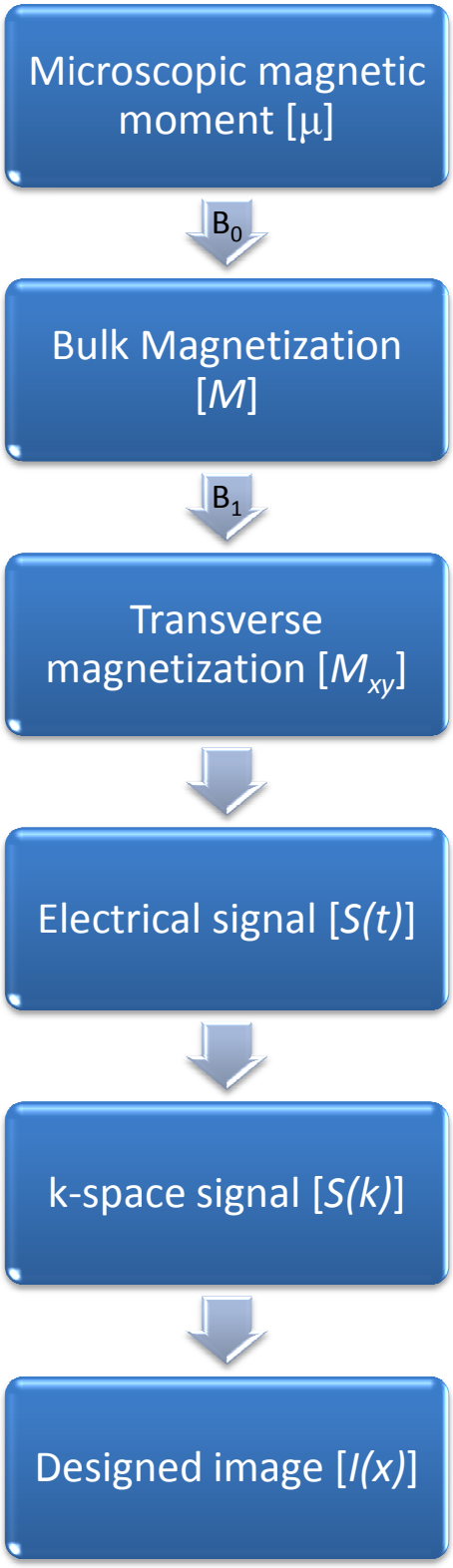

Figure 1.2: Flow chart for principle of MRI

Magnetic gradient system is used to encode special information into the transient responses of a spin system upon RF excitation.

1.4 Cortical Reconstruction: Challenge and Importance

Human cerebral cortex reconstruction or parametric representation of the cerebral cortex from MR image is a challenge in computational neuroanatomy because of its highly convoluted, complex structures and marked variability within and across individuals. Apart from these inherent biological attributes of the anatomic shapes of interest, post-hoc processing in MRI data is limited by factors like image contrast, resolution, SNR, RF field inhomogeneity, sampling artefact and partial volume effect etc. which make the structure boundaries indistinct and discontinuous [3]. That is why integration of cortical boundaries into a coherent mathematical description using model-free, low level image processing techniques such as thresholding, edge detection and linking, region growing, relaxation labeling and mathematical morphology operations produce inefficient results; also because these techniques consider local information only and suffer highly from manual interpretations [1, 3, 12]. Deformable model-based segmentation approach can overcome many of the limitations of traditional image processing techniques [1]. Researchers have tried to implement both types of deformable models in cortical reconstruction as it is a fundamental step for activities like brain image registration [13, 14], image-guided neurosurgery [15, 16], brain geometry analysis [17, 18], functional mapping by means of co-registration of the functional data with the structural image data [19, 20], spatial normalization of brain image [12, 21, 22, 23], cross subject elastic matching or warping for disease analysis [6, 25, 26] and so on. Many acceptable and encouraging results have been achieved but a standard and fully automatic algorithm for accurate result is still an open area of research. Complete automation is a subject of specific application and the demand of accuracy also varies with the application. While coarse reconstruction of the cortex with consistent curves and points are enough for image registration, such kind of approximation may not be tolerated in case of functional mapping or morphometric analysis. In one hand, computational anatomy is gradually sharpening itself to meet the demands of more automation and more precision, on the other hand application of these techniques to explore the natural science of cognition by means of functional analysis of brain or understanding of disease process or development of more advanced techniques is getting an impetus which present more and more challenges to these techniques. It is now time to consider the problem of cortical reconstruction from the perspective of objective rather than put forward a

generalized approach. Optimization between computational resources and levied computational burden is another constraint of this highly complex application. We have addressed the problem by means of hybridization of the existing deformable models with extensive use of knowledge of neuroanatomy to meet the target of *full automation* with *minimum computation* and highly *accurate result* for applications like functional mapping or morphometric analysis.

1.5 Thesis Organization

This thesis has been organized with the following sections with content relevant to development of the proposed reconstruction algorithm. Part II is more or less a traditional literature survey of basic deformable models and its advancement for more complex application along with precise application of those models for cortical reconstruction. This part includes merits as well as demerits of such techniques in the present application and also silhouettes basic hitting points of our approach. Part III details a novel image acquisition protocol and part IV details the proposed novel external force field. In part V, we have detailed the algorithm of Advanced Anatomy Guided Hybrid Deformable (AAGHD) model for cortical reconstruction. The thesis concludes with highlights of the major contributions and scope of future work in part VI. Source of MR image signal and derivation of highly used Euler-Lagrange equation are to be found in Appendix A and B respectively.

PART II
RELATED WORK AND OUR APPROACH

CHAPTER 2

CORTICAL RECONSTRUCTION WITH DEFORMABLE MODELS

CONTENTS

2.1 Overview of Deformable Models

The theory of continuous multidimensional deformable models based on deformation energies in the form of generalized splines was introduced by Terzopoulos in 1986. In 1986, Kass *et al*. introduced parametrically defined deformable model known as "snake" or "active contour model", which can be regarded as a special case of the general multidimensional deformable theory in two-dimensional image domain [27]. This revolutionary invention opened a new frontier in the field of computer vision and inspired researchers to explore the exciting approach with deeper contemplation. Trail of that giant wave is still propagating and researchers are contributing to the archive of deformable models to address more and more challenging problems in the application of real life. Work of these researchers have been highlighted in this section along with the mathematical foundations.

2.1.1 Basic deformable models and its mathematical basis

Geometry, classical mechanics and approximation theory are the three fundamental contributing pillars of the mathematical foundations of deformable models. Though

deformable model geometry incorporates geometric representations with many degrees of freedom (e.g. splines), it is still highly manageable as the degrees of freedom are not allowed to evolve independently because of imposed constraints according to some physical principles. The physical interpretation views deformable models as elastic bodies which respond naturally to applied forces and constraints. Deformable models are broadly classified into two general approaches, the parametric and the geometric models, depending on the definition of the model in the shape domain. Hybridization of these *parametric* and *geometric* models produces a third category of deformable model, namely, the *geodesic* model. Again, parametric model encompasses two forms - *Energy-Minimizing snake* and *Dynamic snake* depending on the applications - statically to single image or dynamically to temporal image sequences respectively. Deformable model can be viewed as a problem of model fitting process in a probabilistic framework and it gives rise to *probabilistic* deformable models.

Parametric model or Active contour model

Parametric model is used in boundary mapping of an object in images, assuming that, the boundaries are piecewise continuous or smooth. Mathematical foundation of this active contour model is derived from the theory of optimal approximation involving functionals [2].

Energy-minimizing deformable model or Classical snake

Classical snake is a thin elastic band that is placed on an image to be deformed in order to reach a state of minimal (local) energy to delineate the object boundary.

Description

Geometrically, the deformable contour is an explicit, parametric contour represented in the image plane $(x, y) \in \Re^2$ as $v(s) = (x(s), y(s))^{\mathrm{T}}$, where x and y are the coordinate functions and coordinate values are continuous functions of a scalar parameter, $s \in [0,1]$ in the parametric domain. $(x(0), y(0))$ represents one end of the curve and $(x(1), y(1))$ the other end. A closed curve is defined by $(x(0), y(0))$ and $(x(1), y(1))$ as the same point, i.e., $x(0) = x(1)$ and $y(0) = y(1)$.The shape of the contour is subject to an image, *I(x,y)* and it is typically determined by variational formulation expressed as

$$\mathrm{E} = \int_s \mathrm{E}_{\mathrm{int}}(v(s)) + \mathrm{E}_{ext}(v(s))ds. \qquad (2.1)$$

The functional can be viewed as a representation of the energy of the contour, and the final shape of the contour corresponds to the minimum of this energy. The first term, the internal deformation energy prescribes a *priori* knowledge about the model such as its elasticity and rigidity and can be expressed as

$$\mathbf{E}_{\text{int}} = \int_0^1 \left\{ w_1(s)\left|\frac{\partial v}{\partial s}\right|^2 + w_2(s)\left|\frac{\partial^2 v}{\partial s^2}\right|^2 \right\} ds. \qquad (2.2)$$

The term $\frac{\partial v}{\partial s}$ indicates roughly the change we get in the coordinate locations of the curve as a result of unit change in the parameter *s*. The first derivative of *v* corresponds to the first-order smoothness of the curve, that is, distance between successive points on the curve, while the second derivative determines smoothness in a direction normal to the curve. Parameters $w_1(s)$ and $w_2(s)$ dictate the simulated physical characteristics of the contour and regulate the relative importance of the two smoothness terms. Sometimes these tunable parameter values can be computed automatically using minimax principle [28, 29]. The minimization of the energy in (2.1) and (2.2) forces the curve toward minimum length and maximum smoothness. The second term in (2.1) is the external force derived from the image information and it couples the snake to the image by attracting the snake to edges, mostly as a function of gradient magnitude. A popular formulation for the energy term deriving the external image forces is as follows:

$$\mathbf{E}_{ext}(v(s)) = -c\int_0^1 \left|\nabla[G_\sigma * I(x,y)](v(s))\right|^2 ds \qquad (2.3)$$

where c controls the magnitude of the potential and $\nabla[G_\sigma * I(x,y)](v(s))$ is the image gradient along the curve v(s), which is derived by convolved the image with a Gaussian smoothing filter whose characteristic width σ controls the spatial extent of the local minima of the external force. By minimizing this external potential, the summed up image gradient along the curve is maximized, which means the parametric snake is attracted by strong edges that correspond to pixels with local-maxima image gradient values [8].

Initialization

Being dependent on image gradient information, parametric snake is highly sensitive to image noise or spurious edges and this property of the snake mandates to be initialized close

to the object boundary. Initialization of active contour can be viewed as an inverse problem [28]. In the case of active contour initialization, the *effects* are the external force vectors that are *caused* by the object boundary. Our aim is to approximate this object boundary given the external force vectors. Initialization can be done by one of the three ways.

1. Naïve initialization: As no prior knowledge of image content or any image attributes are used in this initialization (e.g. snake at the image boundary or as a simple geometric shape), there is very little possibilities of convergence with the correct object boundary with this type of initial contour even after an inordinate number of iterations.

2. Manual initialization: A coarsely approximated object boundary is provided by the user and that acts like an active contour to be refined for more accurate object boundary by an active contour algorithm. Such manual interaction is tedious, time-consuming, difficult and may not be possible in some application.

3. Automatic initialization: This is best suited for a given problem for some specific application, rather than any general strategy. Once objective has been designed, low-level primary image processing (e.g. Automated histogram based segmentation, mathematical morphology) may help to form the initial contour of the region of interest (ROI) [30]. *Centres of divergence* (CoD) [31], *force field segmentation* (FFS) [32] and Poisson inverse gradient (PIG) initialization [33] are a few examples of general automated methods of snake initialization. CoD places small circular initial contours at points of zero vector divergence within a given external force field. Major shortcoming of this method is over-segmentation and it requires significant post-processing in the form of region merging. FFS quantizes the external force vector field into predetermined directional unit vectors and forms connected components in between opposing vectors to define the initialization for a system of snakes. This approach is sensitive to clutter and broken edges and generally leads to spurious contours. PIG initialization solves the inverse problem of determining the object boundary that produced a given external force field. Lines of constant value within the energy field (*isolines*) are determined and isoline of minimum energy level serves as active contour initialization.

Evolution and convergence

As the name suggests, energy-minimizing active contour is evolved to minimize some energy to be at rest at minimum energy state. In case of noise free synthetic image, after initialization on the image surface (*I(x,y)*), the snake eventually crawls down the *negative of squared gradient surface* and settles at its valley. This intuitive statement can be expressed mathematically in attempting to minimize the external energy functional only. But, in real-life image, noise disrupts the smoothness in the gradient magnitude surface and the snake is hindered by the impediments created by the noise. To overcome this problem in evolution of the curve, in basic deformable model, Kass, Witkin and Terzopoulos had introduced the internal energy terms stated in equation (2.2). That's why this snake is also popularly known as KWT snake. Considering an object boundary as smooth or piecewise smooth, final contour is desired to be smooth. From equation (2.2) we can note that a contour with lower internal energy should have average lower magnitudes, the first and the second derivative of *v* with respect to the parameter *s*. In accordance with the calculus of variations, the contour v(s) that minimizes the energy E must satisfy the condition that functional derivatives of the total energy functional (2.1) equals to zero, also known as the Euler-Lagrange equation

$$\frac{\partial}{\partial s}\left(w_1 \frac{\partial v}{\partial s}\right) - \frac{\partial^2}{\partial s^2}\left(w_2 \frac{\partial^2 v}{\partial s^2}\right) - \nabla \mathrm{E}_{ext} = 0 \qquad (2.4)$$

The equation is solved with the help of numerical techniques by discretizing the equation and solving the discrete system iteratively. Gradient descent method is one of the popular numerical methods to solve this equation. Originally, Kass et al. proposed resolution minimization method, where partial derivatives were estimated by the finite-difference method. Later on, Amini et al.[34] proposed dynamic programming approaches to solve this problem.

This classical energy-minimizing contour can be analyzed in probabilistic framework by approaching with Bayesian theorem [1, 3, 28] which is known as the probabilistic deformable model.

Dynamic deformable model

To make this classical energy-minimizing snake a time-varying dynamic model, the parametric contour has to be treated as a function of *s* as well as a function of time *t*. So, $v(s) = (x(s), y(s))^{\mathrm{T}}$ of the static classical deformable contour becomes

$v(s,t) = (x(s,t), y(s,t))^{\mathrm{T}}$ for the dynamic model. To add inertial and damping forces during evolution, the contour is to be introduced with a mass density $\mu(s)$ and a damping density $\gamma(s)$ [1] along with the internal force similar to the static deformable contour. The equation of motion for such contour can be expressed as follows:

$$\mu \frac{\partial^2 v}{\partial t^2} + \gamma \frac{\partial v}{\partial t} - \frac{\partial}{\partial s}\left(w_1 \frac{\partial v}{\partial s} \right) + \frac{\partial^2}{\partial s^2}\left(w_2 \frac{\partial^2 v}{\partial s^2} \right) = -\nabla \mathrm{E}_{ext}(v(s,t)) \tag{2.5}$$

Equilibrium is achieved when all forces are balanced and the contour comes to rest by means of $\partial v/\partial t = \partial^2 v/\partial t^2 = 0$. This dynamic deformable contour not only quantifies shape of the object but also measures its temporal changes.

Geometric active contour or Implicit snake

Geometric active contour models that can adjust with the image topology and can delineate an arbitrary number of ROI, have been proposed by Caselles *et al.* [35] and Malladi *et al.* [36] based on curve evolution theory. Mathematical foundation of this model comes from Euclidean curve shortening flow that is the Euclidean perimeter shrinks as quickly as possible when the curve evolves with a velocity profile which is a function of the curvature. Such type of flow confirms that the curves are increasingly smooth or regular over time. Convergence problem of this evolving (expands or shrinks) curve to the boundary object can be approached using the level sets model [5]. The level set approach to image segmentation is based on the fact that the intersection of a smooth three-dimensional surface and a plane yield a closed set of curves [28]. In this approach, an implicit function $\phi(x, y, t)$ is the height of the surface at position (x, y) and at time/level t. The 3rd dimension is considered as the "level" of ϕ. In an image $I(X)$ where X is a point in $\Re^2$ or $\Re^3$ this implicit function can be parametrically expressed as $C(p,t)$ where p is a geometric parameter ($p \in [0..1]$) and the desired contour at convergence is $C(p)$. The function ϕ happens to be identical to C(p) on the level 0.

$$\phi\,(x, y, 0) = C(p) \tag{2.6}$$

This is the so-called zero level set. The flow of the contours can be described by a partial differential equation as

$$\frac{\partial C(p,t)}{\partial t} = g\left(\left\|\nabla G_\sigma * I\right\|\right)F(\kappa)\vec{N} \qquad (2.8)$$

g-function is essential to reach the right contour and it acts as a "stopping term". To force the speed of the contour to zero at the boundary, g-function may be chosen to be small near an edge, and can be designed as

$$g\left(\left\|\nabla G_\sigma * I\right\|\right) = \frac{1}{1+\left\|\nabla G_\sigma * I\right\|^m}, \quad m = 1 or\, 2 \qquad (2.9)$$

G_σ is the Gaussian smoothing filter with scale-space parameter σ, though other smoothing filters can be used. κ denotes the curvature of the curve *C(p,t)* at *(p,t)* and can be expressed as

$$\kappa = div\left(\frac{\nabla C}{\left\|\nabla C\right\|}\right) \qquad (2.10)$$

$\vec{N}$ is the unit normal vector (inward or outward) along *C(p,t)* and *F(κ)* is evolution speed function, expressed as

$$F(\kappa) = \nu + \kappa, \quad \nu \geq 0 \qquad (2.11)$$

where, *v* is a constant stabilizer for the convergence speed and considered as the inflation term [37] essential to keep the evolution moving in proper direction by determining shrinkage or expansion of the contour according to its sign.

In brief, g-function states that the evolving contour *C(p,t)* expands or shrinks with the speed *F(κ)* along the normal direction of *C(p,t)* up to the level zero set by the criterion e.g. edge map or intensity gradient. Apart from intensity other stopping terms like texture, optical flow, stereo disparity etc. can also be considered [37].

Geodesic active contour

Concepts of classical energy-minimizing active contour and geometric active contour have been unified to produce a new active contour, named geodesic active contour, proposed by Caselles, Kimmel, Sapiro and Kichenassamy [37, 38]. An extra term is added to the overall speed function, called "doublet" in order to attract the contour very quickly to the boundary, and, if necessary, to push the contour backwards if it passes the edge. The level set version of the speed function of this model on $\Re^2$ can be expressed as follows

$$\frac{\partial C(p,t)}{\partial t} = g\left(\left\|\nabla G_\sigma * I\right\|\right)(\nu + \kappa)\vec{N} - \left(\nabla g.\vec{N}\right)\vec{N} \tag{2.12}$$

In geometric active contour, due to the formulation of the image force (g-function), it never comes to a complete stop, and heuristic stopping procedures are essential to turn off evolution of the contour. The contour evolution is slower when the g-function is small but the curve does not necessarily stop completely at the boundary, since it never reaches equilibrium. But, in geodesic snake, the additive term $\left(\nabla g.\vec{N}\right)\vec{N}$ balances the other term close to the boundary and causes the curve to stop there.

2.1.2 Modification to potentiate the basic models

The basic concept of parametric deformable models lies on the *designing* of the external force field which comes from the image data, *parameterizing* the contour in terms of internal energy or flexibility and *optimizing* the contour in terms of evolution or way of interaction between internal energy and the external force field which results convergence of the contour to the object boundary. These three sections are the source of all of the potentialities as well as limitations of the deformable models after addressing the problem of *initialization* which is highly application dependent. Further advancement of this deformable model can be roughly categorized in the development in these three sections.

Improved designing of the external force field:

As the sole objective of deformable models is delineation of the object boundary, edge map of the given image is the primary source of the external force field. The gradient of the edge map has vectors pointing towards the edges with a large magnitudes close to the edges but nearly zero in the homogenous region of the image. As a consequence, capture range of this force filled is very small which demands initialization of the contour very close to the desired object boundary. Several attempts have been made to increase the capture range of the force filled. Gradient Vector Flow (GVF) proposed by Chenyang Xu and Prince [12, 39] has addressed this problem by extending the gradient map further away from the edges using a computational diffusion process. GVF is the vector field $V(x,y)=[u(x,y),v(x,y)]$ which minimizes the following energy functional

$$E = \iint \mu\left(u_x^{\,2} + u_y^{\,2} + v_x^{\,2} + v_y^{\,2}\right) + \left|\nabla f\right|^2 \left|V - \nabla f\right|^2 dxdy \tag{2.13}$$

where, ∇f is the gradient of the edge map and μ is a controlling parameter that controls the degree of smoothness of the field *V*. The first integrand keeps the field, *V*, smooth, while the second integrand encourages the field to resemble the edge force where the latter is strong [28]. GVF field can be found by solving the following Euler equation

$$\begin{aligned}&\mu\nabla^2 u-\left(f_x^{\,2}+f_y^{\,2}\right)(u-f_x)=0\\&\mu\nabla^2 v-\left(f_x^{\,2}+f_y^{\,2}\right)(v-f_y)=0\end{aligned} \tag{2.14}$$

Diffusion of the edge map in the GVF field is indifferent to initial contour and despite its capacity to extend the capture range of the vector field of the edge map, never ensures the correct boundary delineation. To make this vector field sensitive to the initial contour, Dirichlet boundary condition has been incorporated into the GVF by N. Ray *et al.* to produce enhanced gradient vector flow field (EGVF) [40]. The corresponding Euler equation for EGVF is as follows:

$$\begin{aligned}&\mu\nabla^2 u-\left(f_x^{\,2}+f_y^{\,2}\right)(u-f_x)=0\\&\mu\nabla^2 v-\left(f_x^{\,2}+f_y^{\,2}\right)(v-f_y)=0\\&when\ \ (x,y)\in(\Omega/C),(u,v)=\lambda n_{\partial C}\\&and\ \ (x,y)\in\partial C,\nabla u.n_{\partial C}=0\ \ and\ \ \nabla v.n_{\partial C}=0\end{aligned} \tag{2.15}$$

where additionally the symbol Ω denotes the image domain, *C* denotes the domain enclosed by the initial active contour, Ω*C* denotes the set difference of Ω and *C*, ∂C is the boundary of *C*, and $n_{\partial C}$ is unit outward normal to the boundaries ∂C, λ is a positive parameter for Dirichlet boundary condition.

B. Li and S. T. Acton [41] proposed Vector field convolution (VFC) to increase the capture range by means of diffused force field with the help of convolution technique. A prefixed vector kernel is convolved with the edge map to form external force field. The prefixed isotropic vector kernel **k** is defined as

$$\mathbf{k}\,(x,y) = m(x,y)\,\mathbf{n}(x,y) \tag{2.16}$$

where $m(x, y)$ is the magnitude of the vector at (x, y), and $\mathbf{n}(x, y)$ is the unit vector pointing to the origin at the centre of the matrix **k**. The VFC external force field $v(x, y)$ is yield by the convolution of the vector field kernel $\mathbf{k}(x, y)$ and the edge map $f(x, y)$

$$v\,(x,y) = f\,(x,y) * \mathbf{k}(x,y) \tag{2.17}$$

Improved parameterization for internal energy

The flexibility of a parametric contour depends on pattern of parameterization of the contour. Local deformation behaviour of the curve i.e. deformation of only a portion of the curve within a local neighbourhood of the point can be better explained by the concept of splines. Fugeiredo et al. has introduced the spline snakes which adaptively modify the number of control points in snakes represented by B-spines.

Improvement for better convergence

All attempts of redesigning of the external force field or parameterization of the contour for controlling the flexibility are aimed to proper convergence of the contour with the true object boundaries. Despite all attempts, convergence to the true object boundaries is a big problem due to local minima of the model's energy or spurious edge in the image due to some artifact (e.g. sampling artifact) or noise.

This problem is addressed inherently by the GVF force field by Xu and Prince [12, 39]. The controlling parameter μ of the smoothing term in (2.13) regulates the tradeoff between smooth vector field and the gradient of edge map and to be set according to the presence of the noise in the image to overcome the edginess due to noise.

An internal "inflation" force is used by Cohen and Cohen [42] to expand the snake model through spurious edges due to noise toward the real edges of the structure. A typical external force for this balloon model can be expressed as follows

$$E_{ext} = k_1 \vec{n}(s) - k \frac{\nabla P}{\|\nabla P\|}\big(v(s)\big) \qquad (2.18)$$

where $n(s)$ is the unit vector normal to the curve at point $v(s)$ and k_1 is the amplitude of this force and k is the amplitude of the factor coming from potential P. P may be function of derived image information or any others, like distance of a point on v and the nearest edge [42]. Since the balloon force inflates the snake everywhere with an equal amount of force irrespective of the image data, the snake may "leaks" through edges having weak gradient magnitude [12, 28].

While edge-based image information is insufficient for accurate boundary tracking of ROI and trapped by the insignificant edges, many researchers consider integration of region-based

information into deformable contour to decrease sensitivity to insignificant edges and initial model placement. Rougon and Preteux [43] have incorporated mathematical morphology in the active contour model as deformable marker. Gauch *et al*. [44] introduced hybrid boundary-based and region-based deformable model to exploit merits of both of the approaches. Amit Chakraborty and James S. Duncan [45] have introduced game theoretic approach for region-based segmentation with probabilistic deformable model considering the segmentation problem as a two-person nonzero-sum noncooperative game. Poon *et al.* [46] use a discriminant function to incorporate region-based image features into the image forces. The discriminant function allows the inclusion of additional image features in the segmentation and serves as a constraint for global segmentation consistency. Herlin *et al.* [47] has introduced deformable region model in the mathematical environment of Markov Random Field (MRF) and stochastic process. T. Chen and D. Metaxas [48] have also integrated MRF and deformable models for segmentation problem. S. C. Zhu *et al*. [49] has introduced the concept of unification of snake/balloon model, region growing and Bayes/Minimum Description Length (MDL) in an algorithm named "Region Competition". A generalized energy function which combines active contour and region growing is proposed here and the objective function is minimized to converge to a local minimum. R. Ronfard [50] used region-based model where the parametric model partitions the image into ROI and background with different statistics approximated with Gaussian distributions and their difference drives the model evolution. The statistical model of ROI, I_{ROI} and that of the background, I_b are compared with the image I by means of minimization of the mean square error. Energy formulation of this model is as follows

$$E_{MSE}(X) = \iint_{ROI} \left\| I_{ROI}(X) - I(X) \right\|^2 dX + \iint_{b} \left\| I_b(X) - I(X) \right\|^2 dX, \quad X = (x, y) \qquad (2.19)$$

S. R. Gunn and M. S. Nixon [51] used a dual active contour combined with a local shape model. One contour expands from inside the target feature while the other contracts from the outside. The contour *v* evolved in this model according to the following equation.

$$v_i^{t+1} = v_i^t + \frac{1}{2}\left(\lambda \frac{e_i}{h} + (1-\lambda) F_i \right) + g(t) \frac{u_i - v_i^t}{\left| u_i - v_i^t \right|} \qquad (2.20)$$

where *u* is the other contour and *g(t)* is the strength of the adaptive driving force and F is the external force derived from image information. The internal energy of the contour at v_i, is the

energy associated with the force e_i, normalised by the average space step, h, rendering the energy scale invariant and λ is a regularizing parameter.

Further development of the basic parametric model have been done for better convergence with the topologically complex structures like long tubular shape or bifurcation or sudden change of any topology or boundary concavity in narrow fold like shape and so on. T. McInerney and D. Terzopoulos [52] proposed "Topology adaptive snakes" or "T-Snakes" defined in affine cell image decomposition (ACID) framework to allow more topological flexibility over the classical snake. ACID divides the image domain into a grid of discrete cells and it automatically reparameterizes the T-snakes as they evolve with a new set of nodes by computing the intersection points of the model with the ACID grid. This allows the model to split or merge and adapt to the topology of the target image. S. Bischoff and L. P. Kobbelt [53] addressed a similar problem with "restricted snake" or "r-snakes" by restricting the movement of the contour vertices to the grid-lines and thus employ parameterization independent evolution rules. C. Xu and Prince also extended their GVF model to Generalized Gradient Vector Flow (GGVF) model for better convergence of the contour with the boundary concavity, especially at long, thin boundary indentation. It synthesizes a medial property of a shape together with its boundary information. With help of the edge map, GGVF field v is defined as the equilibrium solution of the following vector partial differential equation

$$v_t = g(|\nabla f|)\nabla^2 v - h(|\nabla f|)(v - \nabla f) \qquad (2.21)$$

Spatially varying weighting functions $g(\cdot)$ and $h(\cdot)$ are applied to the smoothing and the data term in comparison with GVF field. For better progression of the deformable contour in long, thin indentation where two edges are in close proximity, weighting functions are selected such that $g(\cdot)$ gets smaller as $h(\cdot)$ becomes larger [12, 54].

Though, further development of the basic geometric and geodesic deformable models has also taken place these review does not mention here as those models do not influence the algorithm developed in this thesis.

2.2 Review of Cortical Reconstruction

2.2.1 An overview

Parametric mapping of the human cerebral cortex generates extreme academic interest for its complex convoluted structure and also because of vast application in medical practice and research leading to experimenting with all variants of deformable models. Besides, several researchers have tried to design specialized deformable models aimed at solving this specific problem only. In 2-D image slice a deformable curve and in 3-D volume data a deformable surface, as the case may be, is used which deforms and progresses as a continuous smooth contour to represent the cortex. As classical deformable models have difficulties progressive into deeper parts of the convoluted cortical folds, most researches have tried to implement deformable models designed in line with the cortical boundary. Basic similarity in all these approaches is classification of the brain tissue with low level image processing which is crucial for initializing the deformable contour and guidance for convergence, followed by estimation of the initial contour and its deformation into the cortical topography.

A. Dale and M. Sereno (in 1993) proposed a cortical reconstruction algorithm for functional localization of cerebral activity by using a deformable model called "shrink wrapping". In this voxel based approach, initial contour is estimated by a recursively flood-filling algorithm to determine the topology of gray-white matter border. This continuous surface is refined by relaxing it against the original 3-D image by means of curve evolution under influence of the local repulsive force field calculated as a function of the deviation of the given pixel value from the expected pixel value of the gray matter in inversion recovery pulse sequence [19].

D. McDonald *et al.* (in 1994) designed an iterative algorithm for simultaneous deformation of multiple surfaces with inter-surface proximity constraints and self-intersection avoidance for cortical reconstruction using cost function minimization [55].

J.F. Mangin et al. (in 1995) proposed an algorithm for construction of an attributed relational graph (ARG) representing the cortical topography from 3D skeleton of the object derived from union of gray matter and CSF [56]. The algorithm is based on homotopically deformable region principle which can be considered as halfway between deformable contour and Markovian segmentation approach.

Davatzikos and Prince (in 1995) used Active Contour Algorithm for Ribbon (ACAR) for modelling the cross section of brain cortex from 2D image plane [57]. External force for the ACAR model is designed on assuming the cortex as a fixed width ribbon like structure and placing a disk centred on the active contour which experiences a driving force proportionate to its distance from the spine of the ribbon. Though the model fails to delineate

the deep sulcual fold, it has been extended with the aids of *control point* based approach to overcome this limitation.

Davatzikos and Bryan (in 1996) implemented deformable surface model in 3D volume data similar to ACAR model of 2D to obtain a shape representation of cortex [58]. DFSA algorithm is used in this model for convergence of the contour in multiscale formulation. At low resolution, DFSA converges very fast to a surface which captures the gross shape of the outer cortex. A finer representation of the outer cortical structure is then captured at a higher resolution.

Kapur *et al.* (in 1996) also used a snake approach, along with Expectation/Maximization (EM) segmentation and mathematical morphology [59]. EM segmentation used for an intensity-based correction and classification of the data into major tissue classes, binary morphology and connectivity used for incorporation of relative topological information, and balloon-based deformable contours of Cohen et al. [42] for refinement of a rough estimate of the morphological operation.

Teo *et al.* (in 1997) [60] incorporated knowledge of cortical anatomy with deformable models, in which white matter and CSF regions were first segmented by posterior anisotropic diffusion, then the connectivity of the white matter was verified. Finally, a connected representation of the gray matter was created by growing out from the white matter boundary.

Though most researchers used specialized deformable model for application of cortical reconstruction, a generalized deformable model was also used to address this problem. GGVF model of Xu *et al.* (in 1997) has been designed for better convergence with boundary concavity and better propagation into long indentation where adjacent edges are close enough. Considering the similarity of the convoluted cortical folds with these attributes the GGVF deformable surface in conjunction with fuzzy membership functions of specific tissue class has been implemented for cortical reconstruction. After tissue classification with fuzzy c means, an isosurface is computed on the basis of white matter membership function to obtain an initial estimator. Using deformable surface, this initial surface moves towards the central cortical layer halfway between the gray/white and gray/CSF boundaries [12, 61] under the influence of GGVF with an extra pressure force.

Topologically adaptive snake (T-Snakes) of McInerney and Terzopoulos (in 1998) is also implemented to segment gray/white interface while its inflation force is weighted with the statistics of the white matter pixel intensity [52].

Apart from these parametric deformable models, Zeng *et al.* (in 1999) implemented geometric deformable models by developing a coupled surfaces approach for automatically

segmenting a volumetric cortical layer from 3D image. They used a set of coupled differential equations, each equation determining the evolution or propagation of a surface within a level set framework [62, 63]. Starting from concentric spheres, the outer and inner surfaces propagate outwards looking for image features of CSF/gray boundary (outer cortical surface) and gray/white boundary (inner cortical surface) respectively, while maintaining a nearly constant thickness in between. Prior to this deformation, a local operator (using the gray level information gives a measure of the likelihood of a voxel lying on the boundary of two adjacent tissues) is used to determine the gray level transition crucial to set level at zero[63].

2.2.2 Potentialities and limitations

Despite so many attempts and approaches, fully automated reconstruction of the outer cortical surface is still a big challenge. Though all approaches address the challenge with success to a great extent, question of automation, close initialization of the deformable models and validation of the end result are still under investigation. All approaches suffer from varied amount of human interaction, approximation and assumption, heuristic tuning of several parameters and above all, a questionable representation of the true surface.

The model of A. Dale and M. Sereno is marked with its potentiality for easy visualization of deep sulcal folds by means of "flattening" of the cortical surface by gradual elimination of the data term from the external force field. But initialization in this model has been done at Gray matter/white matter interface and the curve evolved to CSF/Gray interface which makes the model highly sensitive to magnetic field inhomogeneity nearly obliterating the gray-white demarcation. Besides, data term of the force field is not derived solely from the image data as it depends on some statistically referred pixel value of the gray matter of inversion recovery pulse sequence. This reference is not an inherent feature of the image itself and highly dependent on the validity of related studies and may vary even with different acquisition parameters of the same pulse sequence.

Algorithm of McDonald *et al.* is not only computationally expensive but also requires tuning a number of weighting factors in the cost function [3, 55].

In the model proposed by J.F. Mangin, the method is concern about topology of the cortex ignoring the topology along with cortical volume. To avoid partial volume effect in the narrow sulci, approaches to determine Gray matter/white matter interface rather than CSF/Gray interface. Apart from this overall approach in this model, the precise technique is

also constrained with several factors. Thinning algorithm for skeletonization is highly sensitive to image noise and as a generic structural model of the cortical tomography based on only eight data sets is used as reference topography; the algorithm is inefficient in recognizing more variable sulci [56].

Deformable ribbon of Davatzikos *et al.* is highly encouraging for topological mapping of the cortex and feature extraction from the curvature map and depth map for automatic identification, labelling and matching of the cortical fold [58]. Vaillant and Davatzikos (in 1997) extended this model for parametric representation of the sulcal medial surface to extract sulcal ribbons and characteristics of the cortical shape [64]. But the designed external force propels the active contour towards spine of the ribbon instead of boundary between two objects. In this application it delineates the cortical topology halfway in the cortical thickness. It can not parameterise the CSF/Gray matter interface. Though the topology of the cortex is well maintained and can be used in cortical feature extraction, it may not be suitable for volumetric quantification or functional mapping. In the question of automation, the manual placement of the initializing curve is a limitation, and so could be the tuning of the weights on the external forces [65]. In the *control point* based approach, human inteventions are needed to force the ribbon into the deep sulcal folds [3, 57, 58]. DFSA algorithm of Davatzikos and Bryan is a computationally demanding iterative process and manual intervention is required for close initialization in order to reduce the computational burden.

Although volume measurement may be reliable with the approach of Kapur *et al.,* the shape of the outer surface is a poor representation of the true surface [3, 59]. Use of morphological operation has introduced lot of approximation and empirically tuning of the parameters. It needs manual supervision and intervention if morphological operation fails to remove all non-brain tissues connected to cortex before refinement with the deformable model. Parameters of the internal energy are also dependent of the performance of the morphological operator and needs slice specific manual adjustment.

The process of voxel growing in the model of Teo *et al*. is extremely dependent on precise knowledge of anatomy and most adversely, the user dependent parameter of the number of layers of gray matter is not uniform all over the cortex and varies according to the resolution of the image. It is only applicable for specific functional area at a time. If this selected parameter does not match properly with the resolution of the image, there is high chance of loss of cortical volume in the reconstructed image volume.

Due to medial property of the GGVF deformable surface of Xu *et al.,* it retrieves the central cortical layer but not the outer cortical surface. It may be useful for feature based

image registration but it can not meet other purposes like functional mapping or morphometric analysis. Besides this, the method depends on human interaction for extraction of intracranial tissue from entire brain image, for computation and acceptance of the isosurface as initial estimator of the cortical surface and depends on tuning of a number of parameters empirically [12, 61].

T-snake segments the Gray/White interface with minimum manual intervention, maintaining its topological details, but not the CSF/Gray interface of outer cortical surface.

Because of level set implementation of the model of Zeng *et al*., segmentation algorithm has the advantage of handling highly convoluted structures. Coupled surface approach prevents the inner surface from collapsing into CSF and prevents the outer surface from penetrating non-brain tissue. However, the model is not free from manual intervention in terms of initialization of concentric spheres as starting point of coupled surface and also in the pre-processing. Performance of this model to determine the deep sulcal fold or other features is less dependent on the deformation method but depends more on the local operator that is the determinant of the transition of tissue classes. This operator indirectly depends on the voxel statistics. Apart from that, inter-subject variability of the cortical thickness and regional gradient of the cortical thickness (front to back progressively decreasing) can not balance automation of the process with accuracy of the result [9, 10, 66].

From the limitations of the existing cortical reconstruction algorithm, we can see, maintaining entire brain volume without loss of tissue, preserving the detail topology of the brain cortex unaffected by the partial volume effect in the narrow deep sulci is still an open area of research especially the question of full automation.

2.3 Approaches to Overcome the Shortcomings

Considering potentialities and limitations of the existing deformable models applied for reconstruction of the outer cortical surface from MR image of brain we have developed a novel Advanced Anatomy Guided Hybrid Deformable (AAGHD) Model to make it fully automated with tuning of minimum number of parameters by hybridizing the essence of different deformable models. These models are interrelated with each other in a common space of a prior knowledge of the object shape and hybridized on a strong mathematical basis to address the ultimate objective.

2.3.1 Addressing the problem of image acquisition

We tried to identify the basis of the drawbacks of all existing models. Actually all deformable models with or without incorporation of a priori knowledge of brain anatomy highly depends on parameters derived from image information namely pixel values of the classified tissues, relative differences of their pixel values, edge maps, gradient and so on. Apart from structural variability of the complex brain structure, common source of error is lack of specific information from a particular tissue class. Different tissue classes may share the same information, most importantly the pixel value. If specific non-overlapping information does not reside in the image at acquisition level, mere post-hoc processing is not enough to distinguish different tissue classes depending on the image information. In spite of advances in post hoc processing, image acquisition plays a central role to meet the objectives. Once the objective is defined, image acquisition should be done in a way that leads to minimum computational overheads with maximum accuracy. For this application we have focused on the highest contrast between white and gray matters as well as CSF and gray matters at acquisition level to explicitly delineate the CSF/gray interface without any post-hoc enhancement. The acquisition protocol has been detailed in section III. The resulting images of this protocol have brilliant gray-white contrast which is evident in a unique feature of the histogram. In the histogram, pixels of specific brain structures namely CSF, gray and white matters, background and bones have so distinct gray levels that they group into dominant modes with prominent valleys in between. CSF is confined in the lowermost range of the gray scale and the gray matter, background, white matter and bones are distributed in that order towards the lighter direction of the gray scale.

We were also concerned with the image acquisition time along with image contrast. Higher acquisition time may not be feasible in practical scenario, even if it produces great image contrast. The typical acquisition time was highly comparable with the other protocol and discussed in section III in details. Though application of Compressed Sensing (CS) to MRI offers potentially significant scan time reductions, we could not apply this technique in our data acquisition session. The transform sparsity of MR images and the coded nature of MR acquisition are two key properties enabling CS in MRI. In MRI, CS is claimed to be able to make accurate reconstructions from a small subset of *k*-space, rather than an entire *k*-space grid.

2.3.2 Incorporation of prior knowledge of anatomy

We have exploited the most important aspect of deformable models that is the possibility of incorporating prior information on the shape of the object. Inherent structural complexity by means of highly convoluted shape and marked cross subject variability makes the task of reconstruction of cortex tough and challenging. Incorporation of concept of similarity or likeliness of this object with any other object for reconstruction will produce an approximate result only. Actually, cortex has a complex but well defined shape; leading to a description that cortex shapes like cortex. Accurate and fully automated reconstruction of this complex structure would require a high degree of application specificity as well as model specificity. Implementation of the mathematical model of the cortex itself as a template formed by exploiting the consistent features of the cortex are used in atlas based approaches. Instead of features of the cortex itself, its consistency regarding juxtaposition with the other tissue classes is used here to guide the reconstruction task. Tomographic image like MRI of a structurally normal brain provides only structural information of specific four tissue classes namely bones and soft tissue, CSF, gray matter and white matter along with background. By means of histogram statistics of the acquired image data, CSF has been easily classified and this *CSF map* which is typically confined in between meninges (part of the soft tissues) and cortical gray matter guides the deformable contours to converge with the outer surface of the gray matter.

2.3.3 Hybridization of potentialities of existing model

Failure of the existing models to address the problem accurately has encouraged designing other models and thereby it has produced a voluminous archive of deformable models. Instead of going for a new general approach, we have tried to find the positivity of hybridization of the different models for designing the algorithm specialized for cortical reconstruction only. After initial steps of tissue classification by means of histogram statistics, our model capitalizes on the merits of several existing deformable model to reconstruct the cortical topology accurately without loss of any brain volume. Hybridization techniques decompose the whole objective into multiple steps and analyze the ability of different models to meet the precise step along with their way of interactions on the mathematical basis to make it fully automatic in nature. While generalized approach is highly attractive to address the vast application range in the field of image processing, hybridization technique for specific application is attractive for its accuracy. In the proposed AAGHD

model we have fused the classical KWT snake along with GGVF model in the GGVF force field and a novel external force field. This hybridized deformable model is preceded by analysis of histogram statistics and followed by region growing operation for accurate result.

This hybridization idea actually stems from fusion idea. Fusion is the process or result of joining two or more things together to form a single entity. This idea can also be applied for computer algorithms. Fusion of algorithms is not consists of mere adding or subtracting of different algorithms, rather concatenation of idea of one algorithm with other in parts or as a whole to solve a predesigned problem synergistically. For our application, we have explored the potentialities of different algorithms and tried to fuse them with a prior knowledge of anatomy, rather than developing a general algorithm. In our model, we have fused low level processing with high level processing, again we have fused different deformable algorithms into single one, a new force field also fused with existing deformable algorithm and above all the entire process is fused all-round with a prior knowledge of anatomy. Extension of this fusion idea into machine learning has been discussed in section VI briefly, in the context of this model.

2.3.4 Designing of new force field

While hybridization of the existing deformable models with the proposed force field is not enough to meet the desired accuracy because of the inherent problem specific for the given application, we have designed a new external force to overcome the hindrance. The force field is designed for propagation of the parametric contour into deep narrow cortical fold where evolution of GGVF contour is restricted by the partial volume effect or sampling artifact. The objective of this force field is forceful propagation of the contour beyond spurious convergence due to partial volume effect in to narrow sulcal fold. This force field can be applied in general image processing to break the insignificant boundaries where strength of the boundaries is expressed parametrically with quantifying metrics.

PART III
MR IMAGE CONTRAST AND ACQUISITION

CHAPTER 3

MR IMAGE CONTRAST AND ACQUISITION

CONTENTS

3.1 MR Image Contrast

Contrast can be defined as the intensity difference between different quantities being measured by an imaging system. It also can refer to the physical quantity being measured [67]. In case of image, it refers to the ability of the image to display differences of image intensity for tissues having different properties. A high contrast image shows a large intensity difference between two tissues whose properties differ only slightly. In a low contrast image, two different tissues lying side by side are relatively difficult to distinguish because the intensities of the pixels are nearly equal [68].

MRI is capable of providing outstanding soft tissue contrast and imaging of flow effects [68]. Compared with other neuroimaging methods, MRI has extraordinary versatility for generating images of a wide range of different tissues. In MRI contrast is produced by controlling several different intrinsic parameters related to the chemical makeup of the tissues and extrinsic parameters not specifically related to the chemistry of the tissues. Intrinsic parameters are the relaxation constants T1, T2 and T2*, the proton density, the chemical shift and any flow within the tissue. Extrinsic parameters include the pulse timing represented by repetition time between subsequent radiofrequency excitation pulse (T_R), echo time following

the excitation pulse (T_E), inversion time (T_I), flip angle and more. Contrast can be categorized into two major classes, static contrasts and motion contrasts. Motion contrasts are sensitive to the movement of spins through space (e.g. diffusion, perfusion) and static contrasts are sensitive to the type, number, relaxation and resonance properties of atomic nuclei within a voxel. Typical static contrasts are based on density (e.g. proton density), relaxation time (e.g. T_1, T_2, T_2*), chemical concentration (e.g. lactate, acetylcholine) and even content of a particular molecular type (e.g. macromolecules).

The goal of MRI is to produce contrast between tissue type based on differences in the way these tissues respond to different manipulations of the net magnetic field vector by means of RF energy and gradient field switching. Switching of the various parameters leading to signals being produced from anatomic structures during the imaging process is accomplished through the use of pulse sequences [68]. The pulse sequence is the most critical part of image acquisition, since it defines what the characteristics of the image will be [68]. There are many different pulse sequence designs which produce useful tissue contrast. The most basic are the spin echo pulse sequence, the inversion recovery spin echo pulse sequence and the gradient echo pulse sequence. The critical parameters of a pulse sequence specify the strength, temporal order, polarity, duration and repetition rate of RF pulses and gradients. The parameters related to image acquisition that allow the contrast to be optimized are described throughout this chapter. They include the T_I, T_R, T_E, flip angle, slice thickness and more [68]. Among different contrasts, MR image influenced by static contrast is used mainly to determine brain anatomy due to their ability to illustrate basic tissue characteristics. As we are concern about structural brain anatomy, basic underlying source of image contrast i.e. spin density contrast and contrast based on relaxation times are highlighted in this section.

3.1.1 Spin-density contrast

For this contrast the image intensity is simply proportional to the local number density of spins contributing signal. Most of the spins are single proton nucleus of hydrogen (^{1}H), so this is referred to as proton density contrast. Proton-density images provide contrast based on the sheer number of protons in a voxel, which differs in different tissue types [67]. At equilibrium, the longitudinal magnetization will be greater for greater proton densities. To maximize proton-density contrast, T_1 and T_2 contrast have to be minimized [68]. In practice, a T_R greater than T_1 and a T_E less than T_2 satisfy the criteria [67]. In case of spin echo imaging, a long T_R is used so that the longitudinal magnetization differences between tissues

due to T_1 are mostly eliminated because the tissues have time to nearly return to equilibrium [68]. To preserve this information so that T_2 decay cannot strongly influence the resulting image contrast, a very short T_E is required [68]. If the TR used is much greater than the T1 value of the tissue being imaged (e.g. two to three times as long), the protons will be nearly fully recovered after each excitation. Likewise, if the T_E value is much less than the T2 value (e.g. one tenth as long), there will be minimal decay before image acquisition [67]. Figure 3.1 shows a proton-density weighted image of brain and figure 3.2 schematically diagrams a pulse sequence for generation of proton-density weighted image.

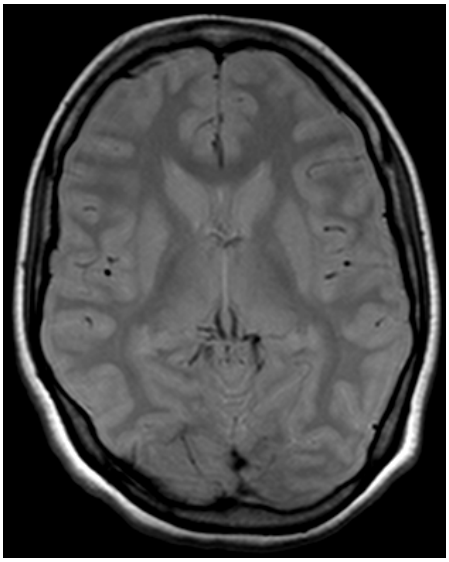

Figure 3.1: Proton-density weighted image at field strength of 1.5 T

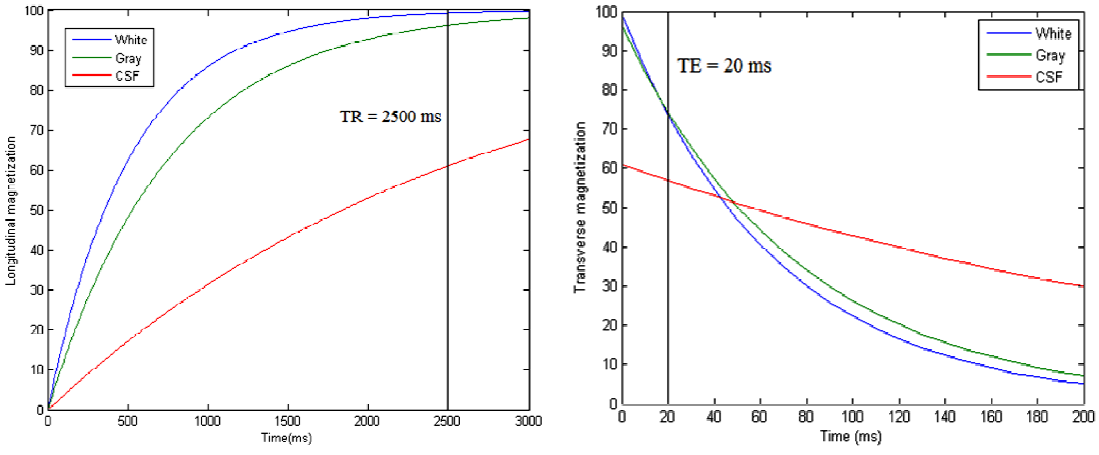

Figure 3.2: Selection of T_R and T_E for proton-density weighted brain image

Tissues with large numbers of protons include fats and fatty components, but there is no marked difference between white and gray matters of brain [67, 70]. This means that, if relying on proton density alone, MR images would show limited tissue contrast [70].

3.1.2 Contrast based on relaxation times

Different tissues in the head have different NMR relaxation times. Image contrast produced by exploiting these differences is derived from differences in T_1, T_2 or T_2* and these are known as T_1-weighted, T_2-weighted and T_2*-weighted images respectively. This type of contrast is achieved by regulating two fundamental sequence timing parameters: T_R and T_E. If consecutive excitations occur at time intervals not enough to allow full recovery of the longitudinal magnetization, the subsequent transverse magnetization, which translates to detectable MR signal, can be expressed as [11, 67]

$$M_{xy}(t) = M_0\left(1 - e^{-T_R/T_1}\right)e^{-t/T_2} \tag{3.1}$$

This equation shows that the MR signal depends not only on the original magnetization (i.e. proton density) but also on the properties of the tissue being imaged (i.e. T_1 and T_2 relaxation times). The term $(1-e^{-T_R/T_1})$ accounts for the incomplete recovery of the longitudinal magnetization, which will reach a steady state after repetitive excitations [67]. Approximate value of time constants T_1 and T_2 at a field strength of 1.5 T for three major tissue classes of brain are shown in Table 3.1 as per reference 1 and these values are used in our experiment mentioned in the following section.

	Gray matter	**White matter**	**Cerebrospinal fluid**
T_1	760 ms	510 ms	2650 ms
T_2	77 ms	67 ms	280 ms

Table 3.1: approximate values for the time constants T1 and T2 at field strength of 1.5 T

The second governing factor T_E is the time interval between excitation and data acquisition. In equation 3.1, we can replace the term *t* with T_E to give the MR signal for an image with a given T_E [67].

$$M_{xy}(t) = M_0\left(1 - e^{-T_R/T_1}\right)e^{-T_E/T_2} \tag{3.2}$$

Equation 3.2 shows the basis for manipulating the signal from a particular tissue type by regulating T_R and T_E.

T1-weighted contrast

Images are called T1-weighted if the relative signal intensity of voxels within the image depends on the T_1 value of the tissue. The tissue that has a shorter T_1 value recovers more rapidly and thus has greater MR signal. For any two tissues that differ in T_1, there is an optimal T_R value that maximally differentiates between them [67]. To achieve exclusive T_1 weighting, a spin echo pulse sequence is designed to reduce the contributions due to T_2 and spin density. This is achieved by using an intermediate T_R (usually less than 500-600 ms) and a short T_E (less than 20 ms) [68]. At very short T_R (shorter than the tissue T_1), there is no time for longitudinal magnetization to recover and thus no MR signal is recorded for either tissue and at very long T_R (greater than the tissue T_1), all longitudinal magnetization will be similar between the tissues [67]. Signal intensity modulated or weighted by a factor that depends on the ratio of T_R and T_1 [70]. At intermediate T_R, there are clear differences between them. Short T_E is essential to minimize T_2 contrast. When T_E is much less than T_2, the term e^{-T_E/T_2} from equation 3.2 becomes approximately equal to one. If T_E is short, then the T2 dephasing does not have time to occur and the differences due to T_1 are preserved in the magnitude of the signal converted to image intensities [68]. The proton density of the tissues always contributes to the contrast, because the number of spins in the imaging volume determines the original net magnetization. Observing the MR signal at Figure 3.3, it can be noted that, the shortest T_1 relaxation time is due to fatty tissue outside the skull as well as bone marrow (very light), while the longest is due to CSF (appears dark). Longitudinal recovery curves for major three tissue classes of brain at figure 3.4 shows that white matter returns to equilibrium faster than gray matter, which returns faster than CSF. It also shows that intermediate T_R differentiates them clearly and short T_E helps to maintain it.

T2-weighted contrast

The amount of signal loss depends on the time between excitation and data acquisition i.e. T_E. An optimal combination of TR and TE exists to maximize the T2 contrast of an image of a multi tissue organ. If T_E is very short, then little transverse magnetization will be lost

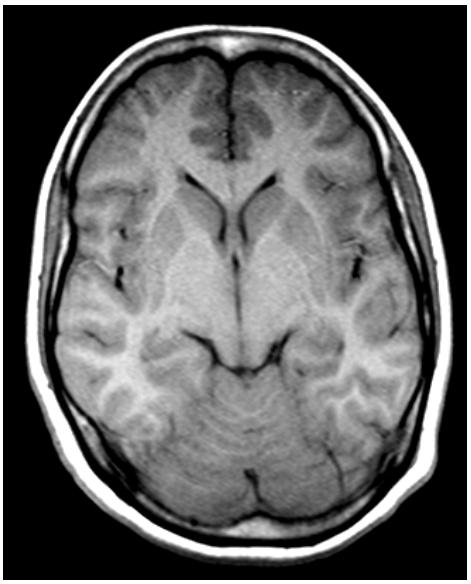

Figure 3.3: T1-weighted spin echo image at field strength of 1.5 T

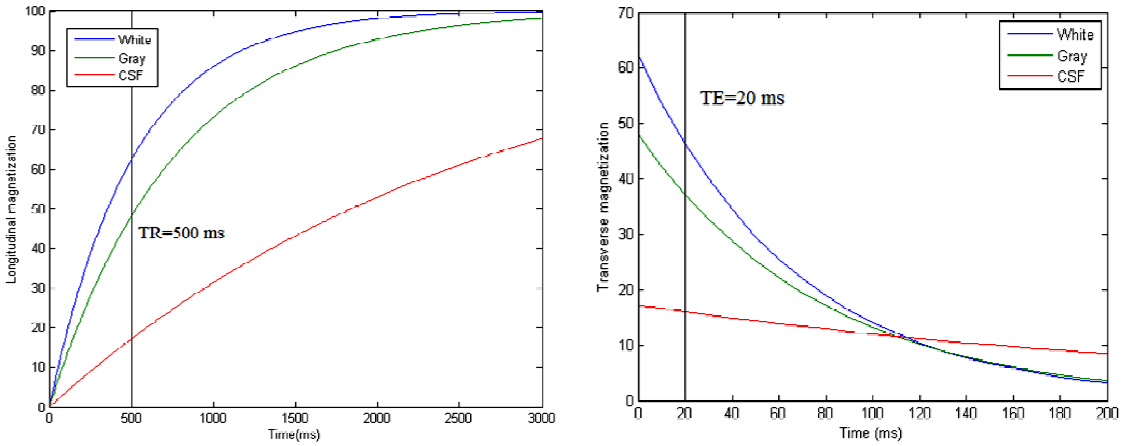

Figure 3.4: Selection of T_R and T_E values for T1-weighted brain image

regardless of T_2 and there will be no T_2 contrast. The same thing is true for too long T_E, as nearly all transverse magnetization will be lost by that time. At an intermediate TE (80-150 ms), the difference in transverse magnetization can be maximized [67]. Tissues that have long T_2 time constants will maintain phase coherence of the transverse magnetization, while other tissues with shorter T_2 relaxation times diphase in the transverse plane and loose signal intensity [68]. Figure 3.5 shows T2-weighted image with maximum signal from CSF as T_2 time constant is highest in comparison to other brain tissues. To minimize the T_1 contrast in

T_2 weighted image long T_R (2000-4000 ms) is essential to complete longitudinal recovery of all tissues by that time. If T_R is much greater than T_1, the term e^{-T_R/T_1} from equation 3.2 approaches 0 and can be eliminated. Figure 3.6 illustrates selection of long T_R and moderately long T_E is essential to generate image sensitive to T_2 contrast. Major disadvantage of T2 –weighted image is that, with extended TE the difference between the transverse relaxation curves of different tissues increases, leading to improved image contrast, but at the cost of decreased signal intensity and thereby decreased SNR [68].

Figure 3.5: T2- weighted image at field strength 1.5 T

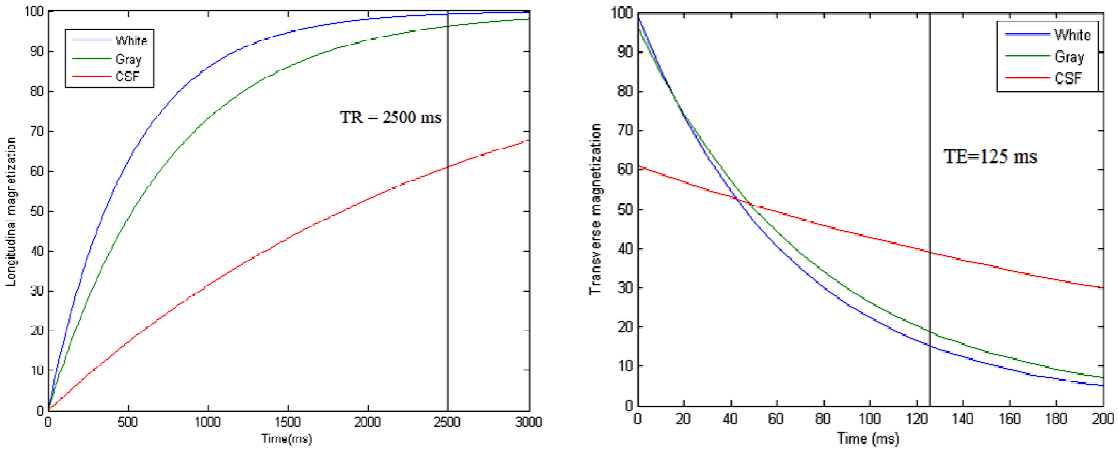

Figure 3.6: Selection of T_R and T_E for T2-weighted brain image

T_2* Contrast

It is often more a secondary property of the geometry of the sample rather than a primary property of the tissue [70]. The combined effect of transverse relaxation due to spin-spin interaction and changes in spin precession frequencies due to inhomogeneities in the magnetic field is given by the time constant T_2*. It forms the basis for BOLD-contrast fMRI and venogram of brain in case of anatomical imaging. T_2* images are sensitive to the amount of deoxygenated haemoglobin present, which changes according to the metabolic demands of active neurons [68]. T_2* contrast is also provided by pulse sequences with long T_R and intermediate T_E values but the pulse sequence must use magnetic field gradients to generate the signal echo. Usually gradient-echo sequences are used. In this case T_E is the time between the initial excitation of the spins and the centre of the gradient echo [70].

3.2 Signal Attenuation from Gray Matter

The goal of this acquisition protocol is to produce contrast between different brain tissues, namely CSF, gray matters and white matters based on differences in the way these tissues respond to different manipulations of the net magnetic field vector by means of RF energy and gradient field switching. The most commonly used structural contrast for anatomical images of the brain is T_1 weighting as there is marked differences of T_1 value between major three tissue classes of brain, namely CSF, gray matter and white matter. Inversion recovery which begins the sequence with a 180^0 inversion pulse boosts T_1 contrast by enhancing the differences of T_1 relaxation among different tissues [11, 67, 68, 69, 70]. In this pulse sequence there is an initial preparatory 180^0 RF pulse, followed by a standard spin echo pulse sequence after inversion time (T_I). This "inversion" of the magnetization and its subsequent recovery dictates the contrast in the images [69]. The choice of T_I changes the contributions of different tissues with different T_1 relaxation times to the image contrast. Depending on the choice of T_I and the particular T_1 relaxation times, the signal from certain tissues will be emphasized, and the signal from other tissues suppressed [69, 70]. In this sequence, longitudinal magnetization of any tissue, in crossing from a negative to a positive value, must pass through zero. If the MR signal is read out when the magnetization is near zero, little or no signal from a selected tissue to be detected based on T_1 relaxation time. This is called null or bounce-point or zero-crossing [11, 68]. Different variant of inversion recovery sequence

modified with this 'signal nulling effect' are STIR (Short Tau Inversion Recovery) and FLAIR (Fluid Attenuated Inversion Recovery) have been designed to suppress the signals emitted from fat and CSF respectively [68, 69]. Signal attenuation from gray matter is another modification of inversion recovery sequence in terms of signal suppression from the gray matters by exploiting this signal nulling effect.

3.2.1 Motivation

In spite of much advancement of MR pulse sequence designing, high contrast MR image of brain for high level image processing is still an open challenge. Apart from complexity and cross subject variability of the anatomic shapes of interest, in MRI, post-hoc processing is limited by factors like image contrast, resolution, SNR, RF field inhomogeneity, sampling artifact due to indistinct and discontinuous boundaries [3]. As a consequence, the spectrum of automated segmentation of brain and its substructures has been extended from histogram-based thresholding [71, 72] to implementation of parametric and geometric deformable contour [55, 56, 57, 58, 59, 60, 61, 62] and atlas-based reconstruction of cortical and subcortical structures [3, 6]. Though all approaches address the challenge with success to a great extent, question of automation, close initialization of the deformable models and validation of the end result are still under investigation. This issue is detailed in part II. Actually all approaches suffer from varied amount of human interaction, approximation and assumption, heuristically tuning of several parameters and above all the questionable representation of the true surface. Actually all mathematical models with or without incorporation of a priori knowledge of brain anatomy highly depends on parameters derived from image information namely pixel values of the classified tissues, relative differences of their pixel values, edge maps, gradient and so on. Apart from the structural variability of the complex brain structure, common source of error is lack of specific information from a particular tissue class. Different tissue classes may share the same information, most importantly the pixel value. If specific non-overlapping information does not resides in the image at acquisition level mere post-hoc processing is not enough to distinguish different tissue classes depending on the image information. In spite of advancement of post hoc processing, image acquisition plays the central role to meet the objectives. Automated segmentation of the gray structures of brain to reconstruct the cortical surface and

morphometric analysis of the subcortical gray structures are the primary challenge of brain image registration [13, 14], co-registration of structural image with functional neuroimaging like PET, SPECT or fMRI [19, 20], image guided neurosurgery [15, 16], brain geometry analysis [17, 18], temporal evaluation of neurodegenerative diseases and more advanced application of brain image. In order to address this challenge, we have attempted to design a standard acquisition protocol of MRI with maximum gray-white and gray-CSF contrast.

3.2.2 Mathematical basis for parameters selection

In MR image, pixel value is a multiparameter function depending on the intrinsic parameters related to the chemical makeup of the tissues, extrinsic equipment parameters as well as their way of interaction [11, 68]. Unalterable intrinsic tissue parameters are nuclear spin density (ρ), spin – lattice relaxation time (T_1), spin – spin relaxation time (T_2), T_2*, molecular motions, susceptibility effects, chemical shift difference etc. The changeable extrinsic parameters which have strong impact on the pixel value are FOV, slice thickness, spacing, matrix size, number of excitation, phase FOV, bandwidth, homogeneity of the static magnetic field and so on. To get full control over the pixel value we neither yield to the constraint of the intrinsic parameters nor depend on the extrinsic parameters. Rather we have explored the mathematical basis of their way of interaction to get the best possible result.

The acquisition protocol has been determined to maximize the contrast between white and gray structures with optimum SNR. Contrast between two classes of tissues can be expressed generally by contrast index $C_{AB} = \frac{|I_A - I_B|}{I_{ref}}$ where, I_A is image intensity of tissue A, I_B is image intensity of tissue B and I_{ref} is normalizing reference value. The contrast index for MRI is a multiparameter function as $C_{AB} = f(\rho, T_1, T_2, T_2^* ...)$, where, function f is dependent on the acquisition protocol. Depending on the chosen parameters, the contrast may be T_1 weighted, T_2 weighted or proton density (ρ) weighted.

To generate greater T_1 contrast we deal with the inversion recovery sequence. Since the goal of imaging is to differentiate between tissues having different relaxation times, T_1 weighting produces better gray-white contrast than T_2 weighting. T_1 differences between CSF-gray matters and gray matters-white matters are more distinct than T_2 differences between these tissue classes. Inversion recovery produces images that are highly sensitive to

T_1 relaxation times by preparing the magnetization with an additional 180^0 RF pulse before the body of the fast SE pulse sequence. Because the inversion pulse flips the net magnetization to the negative state, it effectively doubles the dynamic range of the signal [67]. MR images are usually reconstructed in a way that makes them insensitive to the phase of the signal. As a result, M_Z can only vary between 0 and 1. In case of phase-sensitive images M_Z can vary from -1 to 0 to 1; that is the dynamic range for T_1 contrast is doubled. Phase-sensitive images are more sensitive to image distortions produced by motion or magnetic field inhomogeneity [69]. In inversion-recovery spin echo sequence, T_1 weighted image *I* can be expressed as [11]

$$I = CM_Z^0\left(1-2\exp\left(-\frac{T_I}{T_1}\right)+2\exp\left(-\frac{T_R-T_E/2}{T_1}\right)-\exp\left(-\frac{T_R}{T_1}\right)\right)\exp\left(-\frac{T_E}{T_2}\right) \qquad (3.3)$$

C is a scaling constant that depends on the encoding and image reconstruction methods, M_Z^0 is bulk magnetization. Though this sequence can generate T_1 and T_2 weighted contrast, in practical scenario, for very small T_E the expression denotes T_1 weighting and the expression becomes:

$$I = CM_Z^0\left(1-2\exp\left(-\frac{T_I}{T_1}\right)+\exp\left(-\frac{T_R}{T_1}\right)\right) \qquad (3.4)$$

With this image equation, contrast between gray and white matters C_{GW} is given by

$$C_{GW} = C\left|\rho_G\left(1-2\exp\left(-\frac{T_I}{T_{1,G}}\right)+\exp\left(-\frac{T_R}{T_{1,G}}\right)\right)-\rho_W\left(1-2\exp\left(-\frac{T_I}{T_{1,W}}\right)+\exp\left(-\frac{T_R}{T_{1,W}}\right)\right)\right| \qquad (3.5)$$

where ρ_G and ρ_W are the spin densities for the gray and white matters respectively and $T_{1,G}$, $T_{1,W}$ are the T_1 times for gray and white matters respectively. Similarly CSF-gray matter contrast, C_{CG} is also function of T_I and T_R and can be expressed as

$$C_{CG} = C\left|\rho_G\left(1-2\exp\left(-\frac{T_I}{T_{1,G}}\right)+\exp\left(-\frac{T_R}{T_{1,G}}\right)\right)-\rho_{CSF}\left(1-2\exp\left(-\frac{T_I}{T_{1,CSF}}\right)+\exp\left(-\frac{T_R}{T_{1,CSF}}\right)\right)\right| \qquad (3.6)$$

Where, ρ_{CSF} and $T_{1,CSF}$ is the spin density and the T_1 time for CSF respectively. So, the contrast is a function of two independent variables, T_I and T_R. To find out the corresponding values of these variables for maximum gray-white contrast as well as gray-CSF contrast we have designed a sequence to suppress the signal from the gray matter.

Selection of T_I:

Unlike standard T_1 weighted spin echo sequences, T_1 contrast develops during inversion recovery is primarily dependent upon the interval T_I rather than T_R [69]. For inversion recovery sequence, to make selective tissue components to have zero intensity, appropriate T_I has to be:

$$T_I = \left[\ln 2 - \ln\left(1 + \exp\left(-\frac{T_R}{T_1^0} \right) \right) \right] T_1^0 \qquad (3.7)$$

Tissue with $T_I = T_1^0$ will contribute no signal in the final image. Our aim is to suppress the signal from gray matter for a given field strength with prefixed T_R value. Recovery of longitudinal magnetization of three major tissue classes of brain, namely white matter, gray matter and CSF is shown in Figure. 3.7 with zero-crossing of gray matter. We intended to select the T_I value at zero crossing of gray matter.

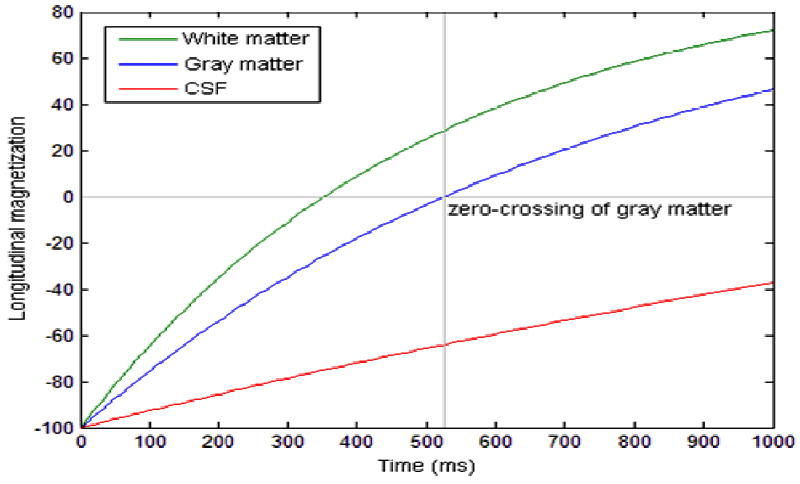

Figure 3.7: Recovery of longitudinal magnetization of three major tissues of brain in case of inversion recovery

Selection of T_R:

Choice of T_I has a modest dependency on T_R. The T_I needed to suppress a particular tissue's signal will be reduced if the T_R is shorter and conversely, increased if the T_R is longer. In general, long T_R is desirable to maximize tissue contrast and the SNR (within the constraints of an acceptable scan time, which is proportional to T_R.) [69]. For this purpose, putting the value of T_I of equation 3.7 with $T_1^0 = T_{1,G}$ in equation 3.5, multivariate function $C_{GW}(T_I, T_R)$ is reduced to a function of T_R only and expressed as:

$$C_{GW} = C\left|-\rho_W\left(1-\frac{2}{2^{T_{1,G}/T_{1,W}}}\left(1+\exp\left(-\frac{T_R}{T_{1,G}}\right)\right)^{\frac{T_{1,G}}{T_{1,W}}}+\exp\left(-\frac{T_R}{T_{1,W}}\right)\right)\right| \qquad (3.8)$$

For optimal contrast, we have $dC_{GW}/dT_R = 0$. On expansion the expression becomes:

$$2\exp\left(\frac{-T_R}{T_{1,G}}\right)\left(1+\exp\left(\frac{-T_R}{T_{1,G}}\right)\right)^{\left(\frac{T_{1,G}}{T_{1,W}}-1\right)}-\exp\left(\frac{-T_R}{T_{1,W}}\right)2^{\left(\frac{T_{1,G}}{T_{1,W}}\right)}=0 \qquad (3.9)$$

Using T_1 values for white and gray matters for specific field strength, the corresponding T_R value is to be solved numerically. For given field strength of 1.5 T, putting $T_{1,G} = 760$ ms and $T_{1,W} = 510$ ms [11] in equation 3.9 the equation for optimal value of T_R is solved. The curve produced in this attempt is shown in Figure 3.8. After $T_R = 0$ ms, the curve increases

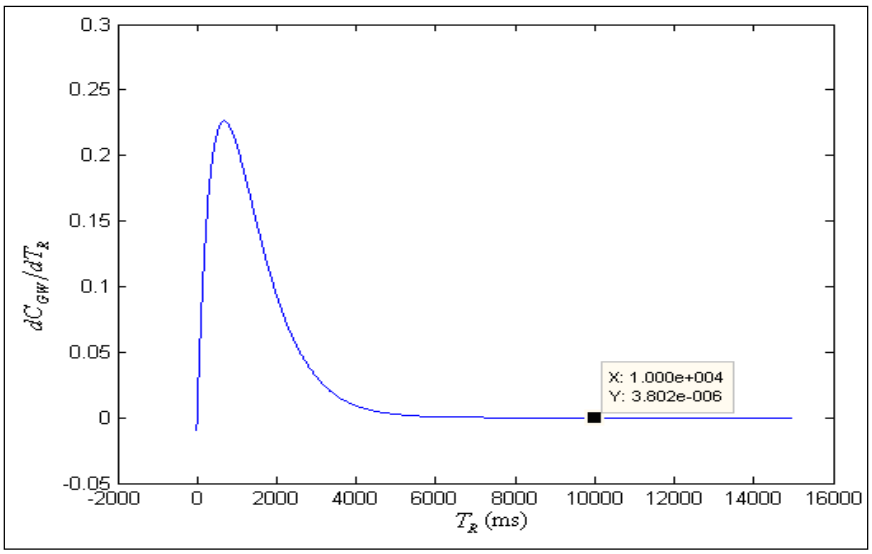

Figure 3.8: TR values for optimal contrast

monotonically up to its global maxima and becomes asymptotic in nature beyond that. $T_R = 0$ ms indicates minimum contrast. For maximum contrast higher value of T_R has been searched. As the total scan time is directly proportional to T_R, practically T_R could not be increased infinitely considering patient compliance. Though exact solution was not met, we fix the T_R value at 10,000 ms heuristically to optimize the image contrast and the total scan time. At T_R=10,000 ms value of expression in equation 3.9 is in the order of 10^{-6} and assumed to be 0 for practical purposes.

By using this T_R value we can get the appropriate T_I from equation 3.7. For T_R = 10,000 ms, corresponding T_I = 527 ms. These T_R and T_I are two essential inputs for final image equation.

Selection of T_E:

To minimize signal loss and T_2 effect in the output image, hardware compatible minimum T_E is used in this acquisition protocol. For practical purpose, T_E varies from 11 to 14 ms.

3.2.3 Analytical discussion on selected parameters

To control the pixel value of the image we have explored the mathematical dependency of the controlling parameters namely T_I, T_R and T_E to get the best possible result. Though the output image is T_1 weighted, proton density of the tissues always contributes to the contrast, because the number of spins in the imaging volume determines the original net magnetization [67]. As the T_R used is much greater than the T_1 value of the tissues being imaged, the protons will be nearly fully recovered after each excitation. Likewise, as the T_E value is much less than the T_2 value of the tissues, there will be minimal decay before image acquisition. As a consequence proton-density weighting is also attributed to the image along with T_1 weighting. The most crucial step is optimization of T_I value as T_1 contrast during inversion recovery, primarily dependent on this parameter. Since we focused on better visualization of gray matter in the output image, we were concern about greater contrast between gray and white matter for inner boundary of cortical gray matter and boundaries of all subcortical gray matters as well as contrast between CSF and gray matter for distinct boundary of outer cortical surface. T_I has to be selected in order to maximize gray-white contrast along with CSF-gray matter contrast as high as possible. To maximize gray-white contrast we have tried

to suppress signal from gray matter by selecting the T_I at its zero-crossing during recovery of longitudinal magnetization. As T_1 value of gray and white matters are markedly different, signal suppression of gray matter does not suppress any signal from the white matter. Now, the question is whether signal difference from white and gray matter with this T_I is maximum or optimum for overall image quality.

Optimum Gray-white contrast

For a given T_R and specific field strength, contrast between gray and white matter is a function of T_I. We can get the curve of gray-white contrast (C_{GW}) from equation 3.5 for field strength 1.5 T with pre-specified T_R value. The curve of gray-white contrast as a function of T_I is shown in Figure 3.9 with its maxima at T_I equals to 400 milliseconds approximately. This value of T_I is much higher than the T_I value of STIR sequence (175 milliseconds) or commonly used T_I value of conventional inversion recovery pulse sequence (150-250 milliseconds) and markedly lower than the T_I used in FLAIR sequence [68, 69]. As a consequence, gray-white contrast

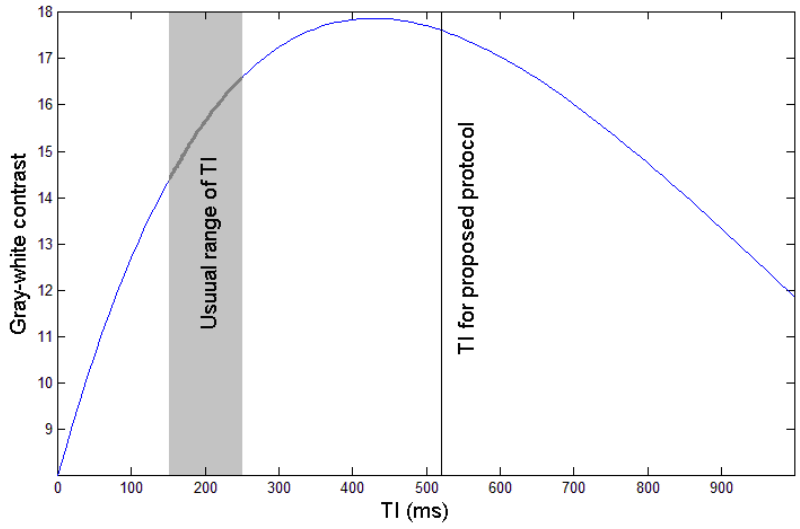

Figure 3.9: Gray-white contrast as a function of T_I

is away from its maximum value in the images from those sequences. Signal attenuation of gray matters with T_I value of 527 millisecond is also little away from maximum gray-white contrast though very close to it in comparison with other inversion recovery pulse sequences. Rationale of this deviation from the value of T_I for the maximum gray-white contrast can be better explained in the ground of CSF-gray matter contrast. Delineation of subcortical gray

matter solely dependent on gray-white contrast, but demarcation of cortical gray matter is dependent on both gray-white contrast as well as CSF-gray contrast for its inner and outer boundaries respectively.

Optimum CSF-gray contrast

For T_1 values of CSF and gray matter for specific field strength and for specified T_R, CSF-gray matter contrast, C_{CG} is also function of T_I and expressed in 3.6. The curve of C_{CG} is shown in Figure 3.10 for field strength 1.5 T and T_R value of 10,000 milliseconds. It is clearly shown in Figure 3.10 that for the maximum CSF-gray contrast, T_I is to be around eight hundred milliseconds. It is neither close to the commonly used T_I value for the conventional inversion recovery sequence or any of its modification namely STIR, FLAIR or even proposed acquisition protocol for signal suppression from gray matter. It is also noted from Fig. 3.9 that, T_I value of 800 ms produces very poor gray-white contrast (C_{GW}). So, maximum CSF-gray contrast can be achieved at the cost of gray-white contrast.

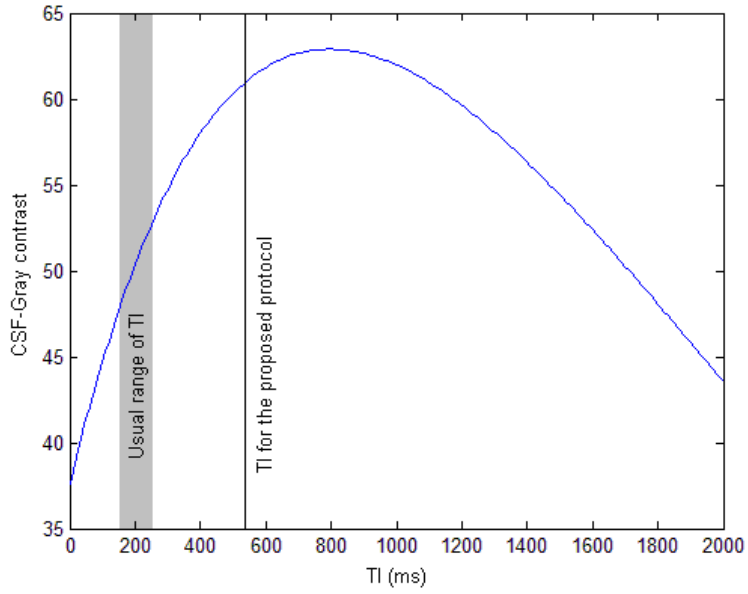

Figure 3.10: CSF-gray contrast as a function of T_I

Justification of T_I value for zero-crossing of gray matter

Fig. 3.10 shows maximum CSF-gray contrast at T_I value of around 800 ms while Figure 3.9 shows the highest gray-white contrast can be achieved at T_I value of around 400 ms. Optimization of T_I value is essential to get the optimum gray-white and CSF-gray contrast instead of the maximum contrast of any one of them. For this optimization, we have designed

a cost function (C_{TI}) based on sum of the absolute difference [70] between maximum contrast and contrast from the current value of T_I for each contrast, namely gray-white and CSF-gray contrast and expressed in equation 3.10.

$$C_{TI} = \left(C_{GW}^{Max} - C_{GW}\right) + \left(C_{CG}^{Max} - C_{CG}\right) \qquad (3.10)$$

Where, C_{GW}^{Max} and C_{CG}^{Max} are the maximum value of gray-white contrast function, C_{GW} and CSF-gray contrast function, C_{CG} respectively. Corresponding T_I for the minima of C_{TI} is the solution for optimum T_I for both the contrast. Minima of C_{TI} is determined by calculus-based approach and solved numerically in order to get the corresponding value of T_I of 625 milliseconds approximately. The curve of C_{TI} is shown in Figure 3.11. It can be noted from Fig. 3.11 that, conventional range of T_I value of 150-200 millisecond is far away from the optimum T_I value while considering gray-white and CSF-gray contrast simultaneously but T_I value of zero-crossing of gray matter, 527 milliseconds is close to this optimum value. Exact optimum value of T_I of 625 milliseconds is not used as gray-white contrast is compromised

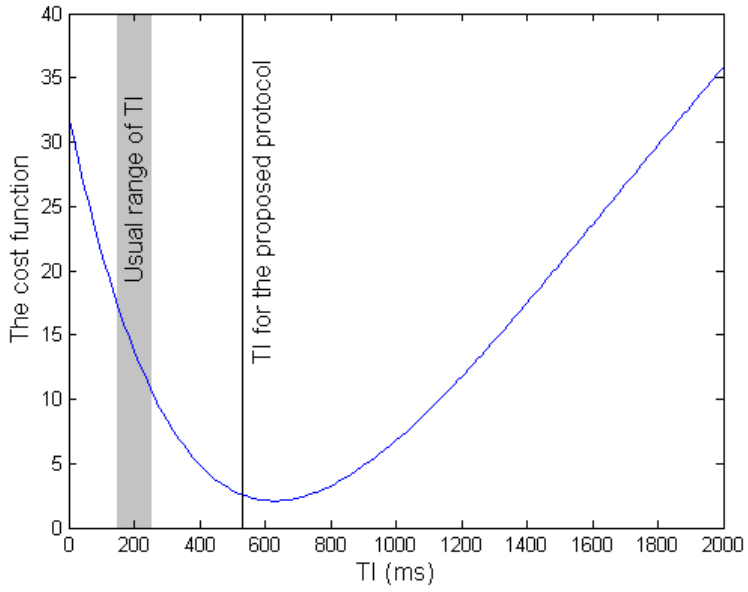

Figure 3.11: T_I for optimum gray-white and CSF-gray contrast

with this T_I without marked improvement of CSF-gray contrast in comparison with T_I value of 527 milliseconds. It is clearly evidenced in Fig. 3.9 and Fig. 3.10 that, shifting of T_I value from theoretical optimum value of 625 milliseconds to zero-crossing of gray matter of 527 milliseconds increases the gray-white contrast at the cost of slight decrease of CSF-gray contrast.

3.2.4 Results

Though the acquisition protocol has been tested with 1.5 T field strength, the same mathematical basis for optimum T_I and T_R can be applicable for any field strength with given T_1 value of gray matter, white matter and CSF for that field. Acquisition parameters are finalized for 1.5 T as follows: inversion-recovery spin echo sequence, coronal, axial and sagittal sections, T_R = 10,000 ms, corresponding T_I = 527 ms, hardware compatible minimum echo time T_E = 11 ms, slice thickness 3 mm, FOV= 210-230 mm and base resolution 256. The protocol has been tested with 1.5 T Siemens and GE scanner on 34 individuals of eastern and south India in the age group of 19 to 32 years after taking written consent with satisfactory outcome. Total scan time varies from 8 to 10 minutes. Unprocessed images of this protocol are illustrated in Figure 3.12.

3.3 Metrics of image quality

3.3.1 Observer assessment

Qualitative assessment

The resulting images of this protocol have brilliant gray-white contrast. Concordance of a group of anatomists on identification of finer details of the gray matters from unprocessed images substantially establishes the potential of this protocol. No post-hoc processing is required for visualization of the delicate gray structures in the images produced by this protocol. This ranges from the gray bridges between the caudate and putamen, intensity variation in globus pallidus and putamen, distinct boundary of the hippocampus and fornix, red nuclei, substantia ferrugenisa of the fourth ventricle, cerebellar folia, to intracerebellar dentate nuclei. Though visual evaluation usually suffers from subjective variations, consistent findings of the intricate details of the structural organization of the brain by the neuroanatomists defy this pitfall of the qualitative evaluation.

Quantitative assessment

Convincing qualitative assessment has been established on objective criteria to eliminate the fuzziness of the subjectivity. In biomedical image, manual segmentation is reasonably unacceptable due to dearth of reproducibility. In case of MR image, source of this error roots in the poor image contrast and resolution that produce ambiguous boundary between two

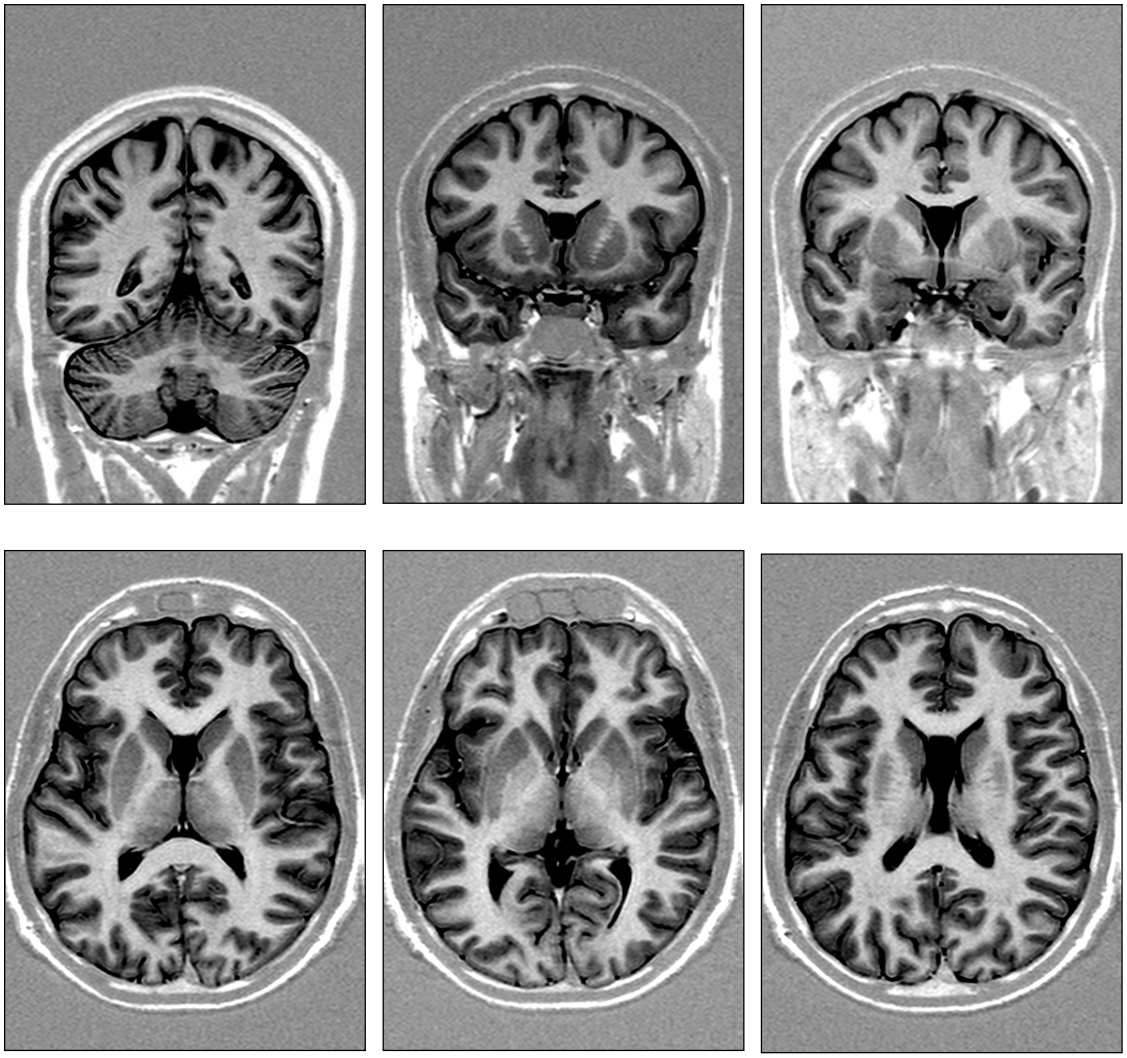

Figure 3.12: MR Image of brain acquired using the proposed protocol

tissue classes [3]. That's why high reproducibility on manual segmentation of unprocessed images is definitely attributed to easily distinguishable boundary of high contrast images.

Manual segmentation of the gray structures by several experts as well as amateurs has been done and their results are analyzed objectively. To measure the similarity quantitatively, we use an index derived from the kappa statistics by Jijdenbos *et. al.*[73]. If area under the segmented region by an expert is denoted as A_1 and the same by another expert is denoted as A_2, then according to [74], the similarity index S is expressed as

$$S = 2\frac{|A_1 \cap A_2|}{|A_1| + |A_2|} \qquad (3.11)$$

where $S \in \{0...1\}$. This index is sensitive to both size and location. It also weights heavily the common area between overlapping regions [73]. In our test result, in all cases the similarity index for two manually segmented structures is inevitably much greater than 0.7, which proves an excellent agreement [3, 74].

1) Agreement between experts: Four neuroanatomists manually segmented the entire brain as well as cortical and subcortical gray structures. The segmented subcortical gray structures include head of the caudate nucleus, globus pallidus and putamen, thalamus, hippocampus, and red nucleus. For a particular structure segmentation is done on the same slice by all the experts and similarity of each pair is established by high similarity index (inevitably more than 0.96).

2) Agreement between expert and amateurs: To eliminate the bias of prior knowledge of neuroanatomy and to emphasize only on the gray-white contrast, we use the same statistical measure to quantify the agreement between the structures segmented by expert and amateur. In this experiment a group of people without any prior knowledge of anatomy is chosen and prompted to delineate a specific structure of the brain solely depending on the gray-white contrast. These segmented structures are quantitatively compared with the same structures segmented by the experts. Excellent agreement in this case is solely attributed to the high contrast between the white and gray structures. TABLE 3.2 shows the quantitative measurement of comparison between segmented images of amateurs and that of expert 1. Better delineation of the boundary of the gray structures reduces subjective bias in manual segmentation by experts and it is quantitatively evidenced by very high similarity index. To eliminate the bias of the prior knowledge and to attribute this credit to the contrast, we compare manual segmentation between expert and amateurs. TABLE 3.2 shows consistent high value of similarity index for all gray structures except hippocampus. Relatively poor index value for this structure can better be explained by the inherent biological property rather than technical inefficiency. Because of gradual transition of hippocampal allocortex to parahippocampal neocortex, proper delineation of the structure depending only on contrast is impossible. This lacuna was masked in comparison of the structures segmented by the experts due to prior anatomical knowledge but become prominent during comparison between structures segmented by expert and amateurs.

TABLE 3.2. Similarity Index

Structures	Case 1	Case 2	Case 3	Case 4
Whole brain	0.98	0.99	0.99	0.97
Cortex	0.98	0.97	0.99	0.98
Caudate head	0.99	0.97	0.96	0.99
GlobusPallidas	0.96	0.95	0.97	0.97
Putamen	0.99	0.94	0.99	0.98
Thalamus	0.89	0.92	0.90	0.84
Red nucleus	0.99	0.98	0.97	0.99
Hippocampus	0.86	0.82	0.80	0.87

3.3.2 Histogram analysis

Global Multilevel Thresholding

Histogram of the image carries some unique but consistent features which are attributed to the high gray-white contrast as well as CSF-gray contrast. Among all structures of the acquired image, main tissue classes are white matter, gray matter, CSF and bone for further evaluation and post hoc processing. In the histogram, pixels of all the aforesaid structures have so distinct and non-overlapping gray levels that they group into dominant modes with prominent valleys in between. It is easy to see that CSF is confined in the lowermost range of the gray scale and the gray matter, background, white matter and bones are distributed in that order towards the lighter direction of the gray scale.

Pixel values of these four anatomical objects and the background are so distinct that five dominant modes are easily identified in the histogram. Global multilevel thresholding by heuristic approach, based on visual inspection on the left most image of the upper row of Figure 3.12 is illustrated in Figure 3.13. Faded out section in the first column denotes

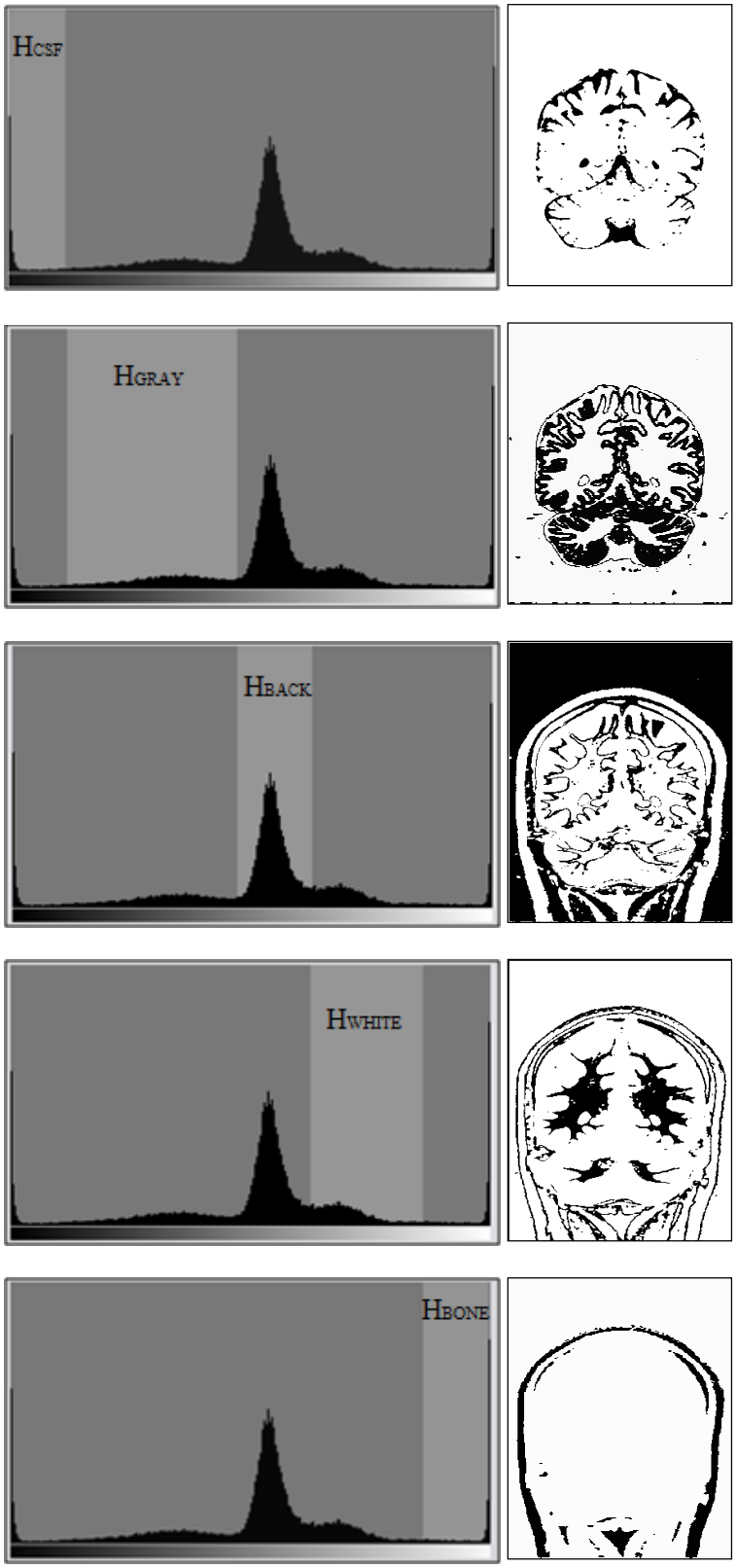

Figure 3.13: Histogram with faded out thresholded region on left and the segmented image on right

thresholded portion and the second column is of the corresponding segmented images. In all the images of our dataset, thresholding of the first mode, H_{CSF} from the lower extreme of the histogram to the nadir of the first valley (gray value 0-30 in Fig. 3.13) is dominated by the CSF. Thresholding of the second mode, H_{GRAY} (30-120 in Fig. 3.13) produces mostly the segmented image of gray matters along with ependymal lining of the ventricles and the dura matter. Thresholding of the third mode, H_{BACK} (120-160 in Fig. 3.13) mainly segments out the background along with some intracranial region. Segmented out image of the fourth mode, H_{WHITE} (160-220 in Fig. 3.13) solely consists of white matter and that of the fifth mode, H_{BONE} (220-255 in Fig. 3.13) represents the bones. This test shows that in the histogram, pixel values of the gray matters ranging over the second mode is far away from the fourth mode, that is, distribution of the white matter, due to marked difference between their absolute pixel values.

It is clearly shown that, from the histogram one can easily identify a mode actually representing a given anatomical structure by simple global thresholding. Very wide gap between distribution of gray structures (H_{GRAY}) and that of white matter (H_{WHITE}) certainly indicates very high gray-white contrast with respect to absolute pixel values of those structures. This is also true for distribution of pixel value of CSF and gray matter. As a consequence outer boundary of the cortical gray matter that is CSF-gray interface and inner boundary of the cortical gray matter that is gray-white interface both are highly distinct. Boundaries of the subcortical gray matters are also very distinct because of optimum gray-white contrast.

Comparison with other image histogram

The proposed acquisition is modification of well known inversion recovery pulse sequence to generate T_1 weighted image of brain. As inversion recovery sequence and its existing modification, FLAIR and T_1-weighted images are well practiced in clinical and research purpose, comparison between those images and their histogram with images of the proposed protocol and its histogram is essential. Every pulse sequence has its own merits and is used in specific purpose. While T1 weighted images and inversion recovery is used in general purpose for visualization of brain tissue and FLAIR is used to suppress the signal from fluid (CSF). The proposed protocol for signal attenuation from the gray matter has been designed for better visualization of cortical and subcortical gray matters for segmentation, morphometric analysis and co-registration with functional brain images. This comparison is to determine prior to any processing task whether any existing protocol can serve the purpose in better way. Figure 3.14

shows images with different protocols in the same field strength (1.5T) and essential parameters of those protocols along with corresponding histograms.

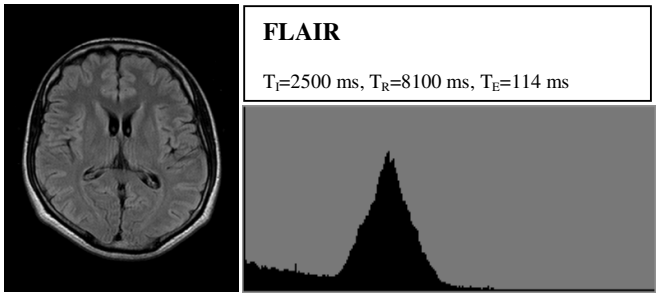

(a)

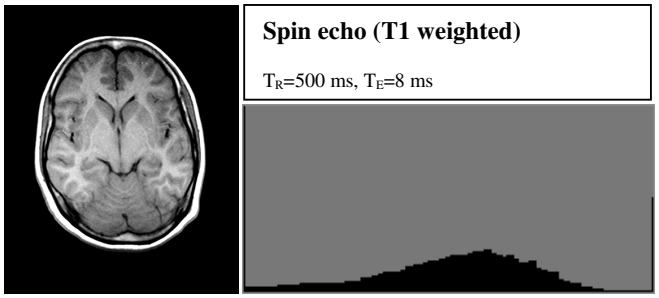

(b)

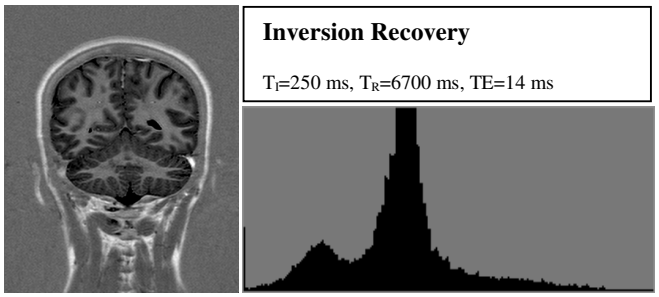

(c)

Figure 3.14: Images from different protocols in same field strength (1.5 T)

High CSF-gray and gray-white contrast is reflected as markedly separated distribution of CSF, gray matter and white matter in the histogram. From the Figure 3.14 (a) and 3.14 (b) it can be noted that no tissue specific information can be obtained from the histogram of FLAIR and T_1 weighted spin echo images because of overlapping pixel values of different tissue classes. In Figure 3.14 (a), two separate distribution is noted, first one for CSF and the background while second distribution mainly comprises of white and gray matters, but separate distribution of white and gray matter as well as CSF is not conspicuous in this

histogram. It is because gray-white contrast is very low while contrast between CSF and the intracranial tissues is high enough due to signal suppression of fluid in this FLAIR sequence. Histogram of the conventional inversion recovery sequence shown in Figure 3.14 (c) and it can be noted that multiple distributions is noted though out the entire gray scale as histogram of the images of our proposed protocol. Further analysis of the histogram of Figure 3.14 (c) reveals CSF is distributed to the lower most limit of the gray scale followed by the distribution of the gray values of the gray matter. Being close to the distribution of the gray matter, gray value distribution of the white matter overlaps the gray value distribution of the background and fails to generate separate conspicuous mode in the histogram. Gray values of CSF, gray matter and white matter are distributed separately but very closely in comparison to the histogram of the images of signal attenuation from the gray matters due to suboptimal gray-white and CSF-gray contrast. Mathematical basis for gray-white and CSF-gray contrast for all these images especially conventional inversion recovery and the proposed modification for signal suppression from the gray matter is discussed in detail in 3.2.3.

In comparison with other images it is noticed that only inversion recovery pulse sequence with usual range of T_I is comparable with the images with suppressed signal from gray matter in terms of multimodal distribution of pixel values in the histogram. But, because of suboptimal contrast CSF-gray and gray-white contrast, modes in the histogram are not distributed wide apart. As a consequence single mode is generated by overlapping pixel values of multiple tissue classes. That's why no tissue specific information can be retrieved from their histogram.

3.3.3. Contrast to noise ratio

In MRI, to assess the relative signal intensity between two relevant tissue classes, contrast to noise ratio (CNR) is more reliable metric than signal to noise ratio (SNR). It is the relationship of signal intensity differences between two regions of interest, scaled to image noise. CNR between gray and white matter, C can be defined as follows:

$$C = \frac{|S_G - S_W|}{\sigma} \qquad (3.12)$$

where, S_G and S_W are signal intensities for gray matter and white matter respectively and is the standard deviation of the image noise. We have compared CNR between gray and white matter of the proposed GrAIR protocol with other standard protocols with commonly used parameters values in the same field strength of 1.5T. TABLE 3 compares CNR of different

TABLE 3.3 CNR between gray and white matter

Acquisition protocol	**Parameters**			**CNR**
	TR	**TE**	**TI**	
GrAIR	10000	11	527	10.11 ± 1.45
FLAIR	8100	114	2500	4.11 ± 0.95
Spin Echo (T1-weighted)	500	8	-	6.21 ± 1.23
Inversion Recovery	6700	14	250	6.62 ± 1.78

images with different protocols and their essential parameters. It is clearly evidenced that, images with GrAIR protocol shows highest CNR.

PART IV
EXTERNAL FORCE FIELD TO OVERCOME PARTIAL VOLUME EFFECT

CHAPTER 4

NEWLY DESIGNED EXTERNAL FORCE FIELD

CONTENTS

4.1 Motivation of Construction

Cortex, the outer most layer of the brain is constituted of gray matter placed between CSF on the outside and white matter inside. The cortical layer of the gray matter is highly convoluted which produces numerous folds and deep narrow fissures called sulci. Cortical reconstruction aims to represent the cortical surface parametrically, preserving the cortical topolology in as much detail as possible. For this purpose two morphological approaches are possible, the first one is detection of CSF/Gray matter interface and the second one is Gray matter/white matter interface. Though both approaches can preserve the cortical topology, only the first approach preserves the entire brain volume in addition. Cortical reconstruction maintaining the topology only has got immense applications like feature extraction, image registration, atlas formation, automated recognition of the sulci, model-based inter subject elastic matching, cortical warping and many more. But preservation of the precise volumetric information along with topological detail is applicable in more extensive domain like morphometric analysis, functional mapping, study of diseases and more in addition to the previously mentioned applications. Though reconstruction of the CSF/Gray interface is appealing and attractive, it is limited by the apparently insurmountable challenge of partial volume effect of the sampled image data. The true CSF/Gray matter interface is difficult to trace when cortical fold is narrow with respect to image resolution due to the partial volume effect or sampling artifact (shown in Fig. 4.1).

In order to avoid this problem, most of the researchers initiate the primary estimator of the deformable contour close to the gray matter/white matter interface to extract the cortical topology. As an obvious consequence, most of the final results converge at gray matter/white matter interface [52] or half way through the cortical width [57, 58, 61]. Though the deformable models of A. Dale and M. Sereno and that of Teo et al. extracts the outer cortical surface at CSF/gray matter interface, both models are dependent on some statistical

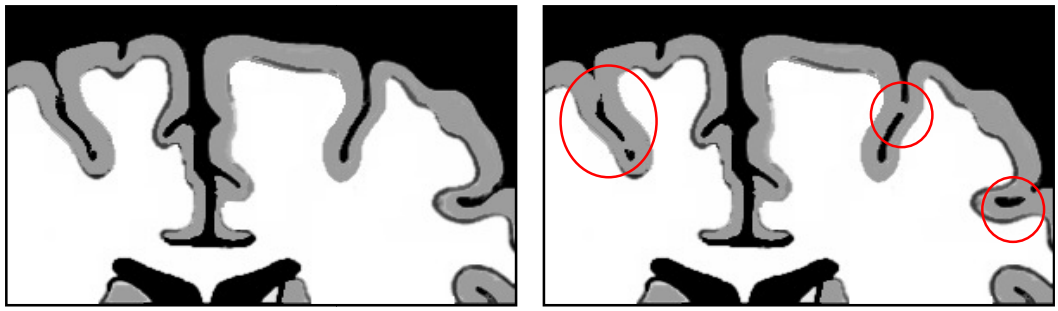

(a) (b)

Fig. 4.1: Resolution problem in sampled image data: (a) Schematic representation of real cortical folds (b) Schematic representation of sampled image of the cortical folds, emphasizing the resolution problem due to partial volume effect at narrow region (red circle)

reference values (reference pixel value of the gray matter and reference range of the cortical thickness respectively) which cannot be derived from image information and may introduce gross approximation when considering the image of an individual as it may not reflect the *in vivo* anatomy of the subject under investigation. Similar type of approximation may affect the accuracy of the models proposed by McDonald *et al.* and Zeng *et al.* where both CSF/Gray matter interface and Gray matter/White matter interface are extracted with inter-surface proximity constraints. Apart from the accuracy and validation of the end results, all models require varied amount of manual intervention. Accurate and automatic propagation of the deformable models into even deeper parts of the narrow sulci overcoming the challenge of partial volume effect is the main driving force for construction of this force field. It is specifically designed for this cortical reconstruction preserving the entire brain volume when the initial deformable estimator approaches from outside to define the CSF/Gray matter interface parametrically.

4.2 Mathematical Foundation of the Force Field

The force field is designed to force the parametric active contour to penetrate beyond sampling artefacts caused by the partial volume effect. This force field is not meant for cortical reconstruction independently, but it is obviously an essential part of the algorithm for fully automated reconstruction of cortex described in detail in section V as the AAGHD model. Mathematical foundation of this force field is based on the GGVF field proposed by C. Xu et al. with relevant modification in its data term. GGVF field has been chosen for this force field because of two reasons:

1. Computational diffusion process of the force field increases the capture range to attract the contour towards the strong points of the images predefined by the data term from far away.
2. Better convergence of the contour with the boundary concavity, especially at long and thin boundary indentation which is crucial for this application.

A typical GGVF model uses gradient of the edge map as its data term for convergence of the contour with object boundary. But the problem here starts where standard algorithms finish. Actually, the initial estimator of this problem resides on spurious but strong edges formed by the sampling artifacts. As the brain is submerged in CSF with its covering called meninges, the entire cortical surface including its convoluted sulcal network is to be ideally in contact with the CSF. But this artifact disrupts the continuity of the CSF breaking it into discrete CSF clusters in the narrow sulcal fold. The phenomenon can be exemplified as a dam placed in a narrow, continuous tunnel that splits it into small reservoirs. In this problem, the deformable contour is initialized at the margin of the dam and is aimed to be pulled into the next reservoir, breaching the dam. That's why at first the force field is directed to propagate the contour towards centre instead of boundary of the adjacent reservoir (CSF cluster in this case). For this reason, the data term of the gradient of edge map for GGVF field is replaced by a new data term pointing the vectors towards the centre. The force field is constructed as a function of the distance of zero to nearest non-zero pixel, and named as Zero-Non-Zero Distance (ZNZD) vector field. The field is constructed in two steps as follows:

1. Tissue classification determining the CSF clusters

2. Designing of the ZNZD vector field.

4.2.1 Tissue classification determining the CSF clusters

In section 3.3.2 in part III, we have the resulting image histogram (Fig. 3.13) of the proposed protocol. It shows that CSF (H_{CSF}), gray matter (H_{GRAY}), background (H_{BACK}), white matter (H_{WHITE}) and bones (H_{BONE}) are distributed progressively in the lighter direction of the gray scale with a prominent valley between two adjacent tissue classes [75, 76, 77]. Automated multilevel thresholding of this histogram can produce specific tissue classes. The CSF distribution (I_{CSF}) on uniform background has been produced by an automated optimal global thresholding [78, 79] of the first mode, i.e., H_{CSF} and the second mode, i.e., H_{GRAY} which extends up to lower limit of H_{BACK}. At the very first step lower level of the third mode, H_{BACK} is to be found out automatically. It is determined by the background removal algorithm [80] as follows:

In reconstructed MR image, background noise manifests as a Rayleigh distribution [81] in the histogram, I_{BRAIN}, of given image, and is expressed as

$$P_{noise}(f) = \frac{f}{\sigma^2}\exp\left(-\frac{f^2}{2\sigma^2}\right) \qquad (4.1)$$

where σ is the standard deviation of the normally distributed white channel noise.

Global maxima or height, $r_{\max}$ of any Rayleigh curve is related to standard deviation of the channel noise as

$$\sigma = 0.607/r_{\max} \qquad (4.2)$$

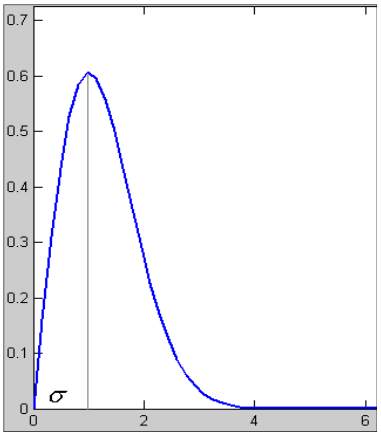

Fig 4.2: Rayleigh curve

All maxima $h(f_i)$ of the histogram function $h(f)$ and the corresponding gray values f_i are traced. Using each value of $h(f_i)$ in (4.2), initially a Rayleigh curve $r_i(f)$ is generated at each maximum. Similarity of $r_i(f)$ in the range σ_i to $2\sigma_i$ is measured with the original histogram in the same range using a similarity index derived from the Kappa statistic as proposed by Zijdenbos *et al.* [73]. If area under $r_i(f)$ in the mentioned range is denoted as R_i and area under the original histogram in the same range is denoted as H_i, then the similarity index S_i becomes

$$S_i = 2\frac{|R_i \cap H_i|}{|R_i| + |H_i|} \qquad \text{where } S_i \in \{0...1\} \qquad (4.3)$$

The corresponding $r_i(f)$ for the highest similarity is considered as the Rayleigh for the noise distribution $r_{noise}(f)$. Peak of the curve $r_{noise}(f)$ coincides with the noise peak of the original histogram. Then $r_{noise}(f)$ is scaled by a constant K and a least square fit is performed by minimizing the error expression

$$\sum_{f=\sigma}^{2\sigma}\left(h(f) - K\frac{f}{\sigma^2}\exp\left(-\frac{f^2}{2\sigma^2}\right)\right)^2 \qquad (4.4)$$

to get the best fit Rayleigh curve $r(f)$. Lower limit of $r(f)$ is considered as the lower limit of the third mode that is image background i.e., H_{BACK} or the upper limit of the second mode i.e., H_{GRAY}.

Part of the histogram below this threshold is clearly bimodal with well-defined peaks and valleys for our image dataset. The first mode represents the CSF and the second mode the gray matter. Because of this distinct bimodal distribution, automated optimal global thresholding of the histogram up to lower threshold of the third mode by the algorithm proposed by Otsu [78. 79] efficiently segments out the distributed CSF in the given image. Given the distinct bimodal nature of the distribution up to upper limit of H_{GRAY} by thresholding proposed by Otsu produces I_{CSF} from I_{BRAIN}. Simple global thresholding upto this point may misclassify some non-brain region. As CSF is included in the region of the least gray value, only the 8-connected set of the least gray value of the image is included during thresholding. This allows growth of the CSF by incorporating the lighter region of CSF and adjacent gray matter which complete the outer boundary of the brain but never

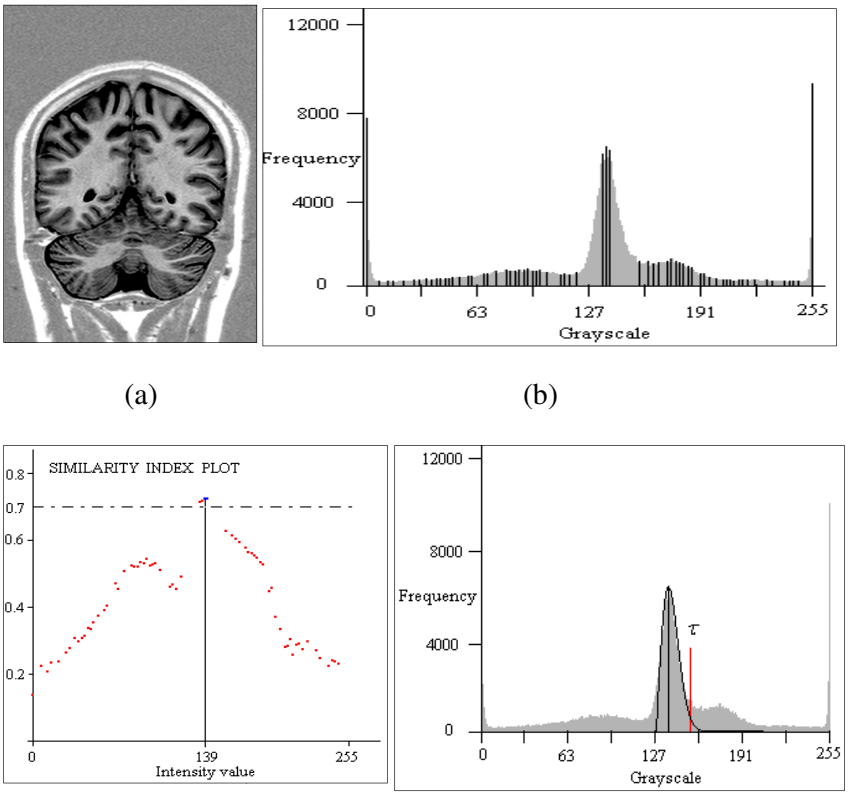

Fig. 4.3: (a) Brain image (b) Noise peak at 139, (c) maximum similarity index 0.72. (d) best fit Rayleigh curve with lower limit 128, upper limit 153

allows growth and coalescing of any discrete region, inside or outside the brain boundary with gray values between the least gray value and the selected threshold.

As the smallest valued pixels serve as seeds for growth during constrained thresholding, if each discrete set of CSF is denoted as C_i, then

$$I_{CSF} = \coprod_{i=1,n} C_i \qquad (4.5)$$

Fig.4.4 shows an example of segmentation of CSF with intermediate result of lower limit of H_{BACK} or upper limit of H_{GRAY} and optimal global thresholding between H_{CSF} and H_{GRAY}.

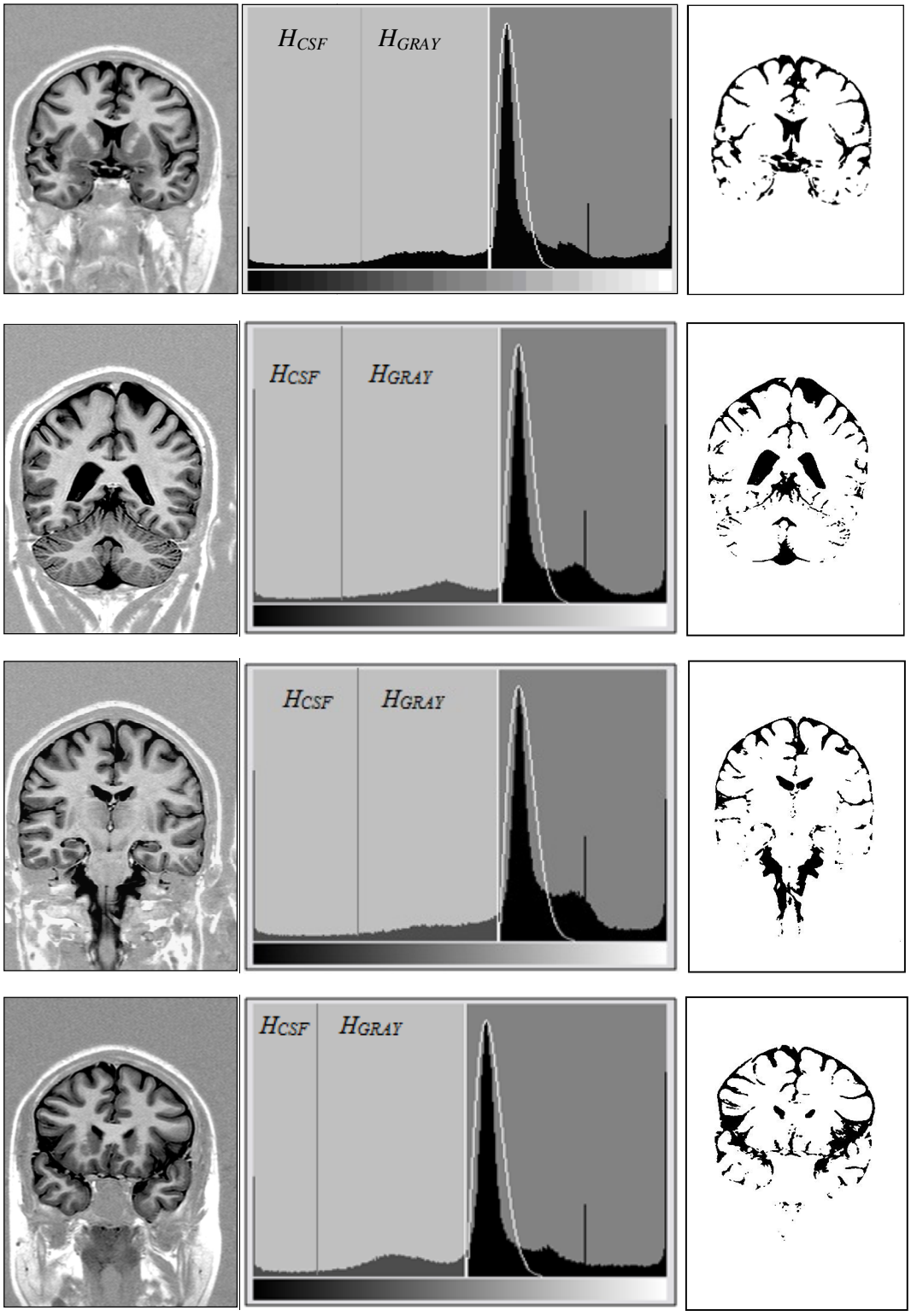

Fig. 4.4: CSF distribution: (a) Given image I_{BRAIN} (b) Histogram with best fit Rayleigh curve, faded out part for optimal global thresholding and the threshold for CSF distribution and (c) the segmented CSF distribution, I_{CSF}

4.2.2 Designing of the ZNZD vector field

Now logical AND of I_{CSF}, the classified image of CSF regions with I_{BRAIN}, the original image forces the entire CSF region to zero instead of a range of gray values in the output image, $I_{BRAIN\text{-}CSF}$. It thus produces a sharp and distinct boundary at the meninges/CSF interface and CSF/gray matter interface with an enhanced gradient. In $I_{BRAIN\text{-}CSF}$ any pixel of zero value must be in the set of CSF, C_i. In narrow grooves of the deep sulci, two juxtaposed sides of the cortical fold may erroneously breach the continuity of this CSF region in sampled image due to partial volume effect. The ZNZD force field, v is designed to pull the deformable contour from one CSF set to another adjacent CSF set instead of pushing the contour towards the object boundary as traditional objective of deformable models. The vector field is similar to GGVF vector field and constructed similarly with smoothing and data terms each scaled with weighting functions. Here the data term is designed as a ZNZD map (ϕ) which is a multivariate function of $D_{Z\text{-}NZ}(x,y)$, the distance of a pixel, Z(x,y) with value zero from the nearest non-zero pixel with value V ($\neq 0$) and the corresponding non-zero pixel value (V) in $I_{BRAIN\text{-}CSF}$. It acts as an external force in this model. If the distance function is $\phi(V, D_{Z\text{-}NZ})$

$$\phi(x,y) = \Psi(V, D_{Z-NZ}(x,y)) \tag{4.6}$$

then $\psi(\cdot)$ can be designed according to application and for our application we have designed the function as follows

$$\phi(x,y) = CV^{-1}\left|D_{Z-NZ}(x,y)\right|^2 \tag{4.7}$$

where C is a scaling constant. Relevant properties of the ZNZD map are

1. The gradient of the ZNZD map $\nabla\phi$ has a vector pointing away from the non-zero pixel value.
2. Magnitude of the vector increases with distance between zero and non-zero pixel value but decreases with the value of that non-zero pixel value.
3. In the region of non-zero pixels, where no Z(x,y) is located, $\nabla\phi$ is zero.

Because of these properties, deformable contour initialized on non-zero region but close to the set of zero, C_i tends to move into C_i depending on the pixel value of the non-zero pixels (V) separating that contour and C_i. Here the component V^{-1} controls fragility of the barrier

between the initial deformable contour and the nearby C_i. Higher pixel value shows less fragility. A computational diffusion process similar to GGVF is used to extend the vector field beyond the sets of zero pixel value. With the help of this ZNZD map in our 2D application, we define the ZNZD vector field, $v(x,y)$ that minimizes the energy functional

$$E_{ZNZD} = \iint m\left(|\nabla \phi|\right)|\nabla v|^2 + n\left(|\nabla \phi|\right)|v - \nabla \phi|^2 \, dxdy \tag{4.8}$$

The gradient operator is applied to each component of v separately. The first term is referred to as smoothing term since it alone will produce a smoothly varying vector field. The smoothing term is designed as GVF field [12], originated from the smoothing term used by Horn and Schunk in their classical formulation of optical flow [12, 82]. The second term is referred as the data term since it encourages the vector field v to be close to $\nabla\phi$ computed from the ZNZD map. The weighting functions $m(\cdot)$ and $n(\cdot)$ are applied to the smoothing and data terms, respectively. We have adjusted these weighting functions in such a way that $m(\cdot)$ gets smaller as $n(\cdot)$ becomes larger for progression of the deformable contour into long thin indention like CSF sets in narrow sulci [12]. That is why, the weighting functions in our application are similar to the weighting functions of GGVF model and expressed as

$$m\left(|\nabla \phi|\right) = \exp - \left(\frac{|\nabla \phi|}{\kappa} \right)^2$$

$$n\left(|\nabla \phi|\right) = 1 - m\left(|\nabla \phi|\right) \tag{4.9}$$

Using calculus of variation, the vector field must satisfy the Euler equation

$$\exp - \left(\frac{|\nabla \phi|}{\kappa} \right)^2 \nabla^2 v - \left(1 - \exp - \left(\frac{|\nabla \phi|}{\kappa} \right)^2 \right)\left(v - \nabla \phi\right) = 0 \tag{4.10}$$

Laplacian is applied to each component of the vector field v separately. A solution to this Euler equation can be found by introducing a time variable t and finding the steady state solution of the following linear parabolic partial differential equation

$$v_t = \exp - \left(\frac{|\nabla \phi|}{\kappa} \right)^2 \nabla^2 v_Z - \left(1 - \exp - \left(\frac{|\nabla \phi|}{\kappa} \right)^2 \right)\left(v_Z - \nabla \phi\right) \tag{4.11}$$

where v_t denotes the partial derivatives of v with respect to t.

4.3 Discussion

As an overview, it can be stated that ZNZD vector field stems from the GGVF vector field proposed by Xu *et al*. designed to overcome the unacceptable convergence of the contour at the spurious boundary due to partial volume effect at narrow sulci. The basic difference of the field with other deformable model is that it never converges with the desired object boundary; it just breaks the barrier of spurious edges. Some stopping criteria is to be set to control the propagation of the deformable contour and further processing is required to find out the final object boundary. Intuitively it can be said that ZNZD field pushes the contour by breaking the fragile barrier of spurious edges to other side where another processing scheme is waiting to propagate the contour to its final destination. Being function of the pixel value (V) of the obstructing pixels of the spurious edges, the field has got an inherent property to be spatially

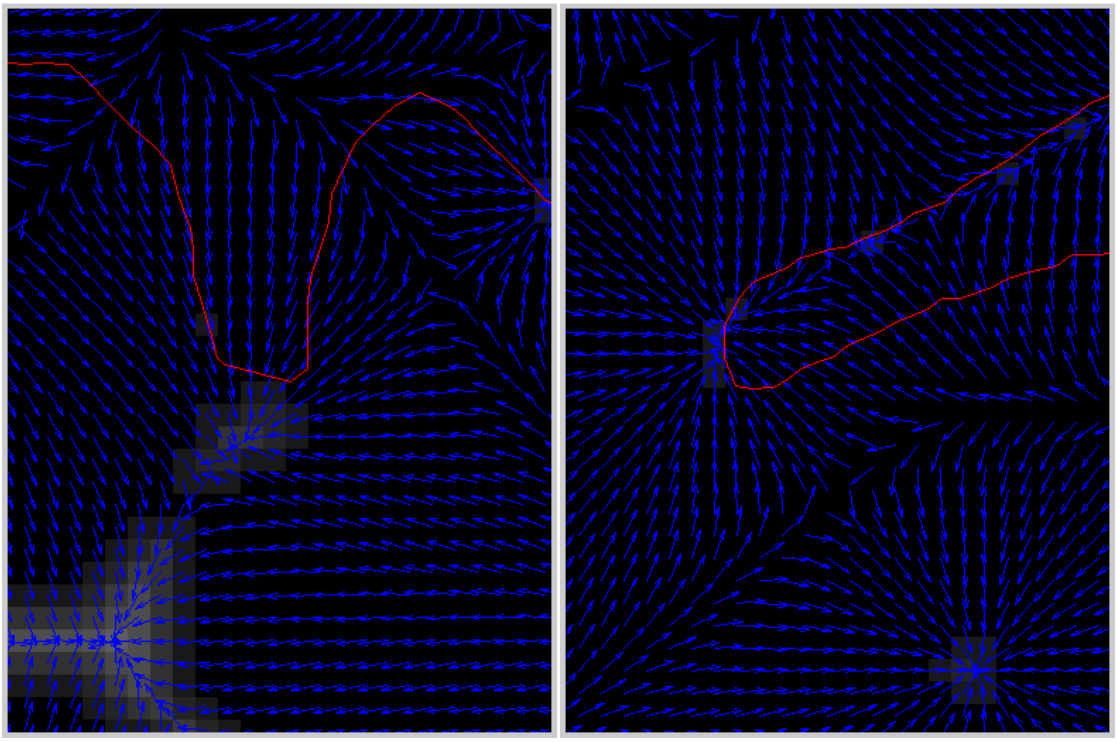

Fig 4.5: ZNZD vector fields showing vectors are not pointing towards edges; red lines are initialized deformable contours

varying in its strength depending on the image information. This property controls fragility or spuriousness of the edge. In our application of cortical reconstruction, to overcome the partial volume effect at deep cortical sulci adjacent to CSF, spurious edges form by pixels of low range of values (close to gray matter). If the initial estimator in the narrow sulci is obstructed with pixels of very high values, then these are invariably not attributable to partial volume effect and should not be considered as spurious edge. The force field is not strong enough to push the contour by breaking such barriers. The data term of the vector field thus varies spatially based on the image information. Though the vectors are only present in the sets of zero valued pixels (C_i) with inward direction, the field is diffused uniformly into the region of nonzero pixel values by adding the smoothing term. Weighting factors for the smoothing term and that of the data term are spatially varying and designed to propagate along the deep narrow indentation. Application of this ZNZD vector field is discussed in section V as an essential part of the fully automated cortical reconstruction algorithm.

PART V
CORTICAL RECONSTRUCTION WITH AAGHD MODEL

CHAPTER 5

ADVANCED ANATOMY GUIDED HYBRID DEFORMABLE MODEL

CONTENTS

Cortical reconstruction has been studied by several researchers in last few decades or so. However, there is no standardized approach nor is there any efficient algorithm in terms of automation and validation of results. Actually, attempts to completely automate the processing of medical images would require a high degree of application and model specificity respectively. In some medical image analysis applications, the presence of various structures with different properties suggests the use of a customized sequence of multiple segmentation techniques. For example, initial steps can use fundamental techniques to reduce the data, and subsequent steps can apply more elaborate techniques that are robust but more time consuming. The best choice of techniques and their order depends typically on the problem as well as computing resources.

A new algorithm called Advanced Anatomy Guided Hybrid Deformable model (AAGHD) is proposed for cortical reconstruction at CSF/Gray interface preserving the brain volume in its entirety and maintaining the cortical topology precisely. The model is highly application specific and consists of a sequential stepwise approach to achieve the final

objective of CSF/Gray matter interface in fully automatic fashion. Most cortical reconstruction algorithms consist explicitly of two step approaches – tissue classification to determine the initial estimator and convergence criteria for deformable models followed by evolution of deformable models. The sequential steps of AAGHD model also includes tissue classification for determination of CSF distribution by using histogram statistics and hybridization of classical snake and GGVF deformable model in an automatically evolving external force field under the guidance of a prior knowledge of anatomy. Initialization of the deformable contour of this model was done outside the cortical gray matter and that's why the model inherently possesses the property to address the challenge of partial volume effect at deep, narrow sulcal fold.

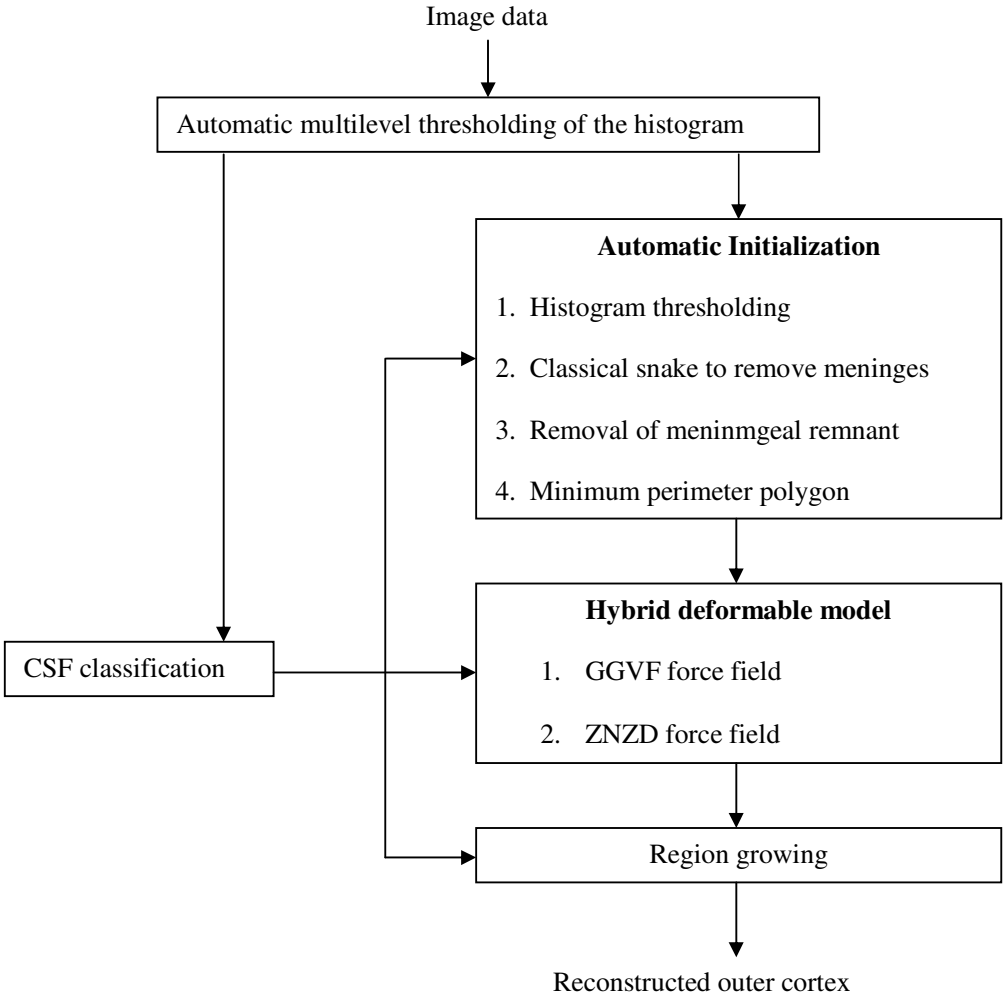

Fig. 5.1: Block diagram of AAGHD model for cortical reconstruction

The name of the model explains itself. Called hybrid deformable model, it assembles the merits of multiple deformable models; and the deformable contour goes through several

external force fields, evolving with the deformable curve itself according to some preset criteria. The term anatomy guided is justified with usage of prior knowledge of anatomy from initialization of the deformable contour to overcome the partial volume effect. Initially name of the model was coined as Anatomy Guided Hybrid Deformable (AGHD) model [30], but further advancement for evolution of the external force field overcoming the partial volume effect has finalized the name as Advanced Anatomy Guided Hybrid Deformable (AAGHD) model. Detail of this model is discussed in this section.

5.1 Step 1: Tissue classification for determination of CSF distribution

CSF distribution is first determined from the given image histogram statistics. Because of high contrast acquisition, images of the proposed protocol require no pre-processing prior to this step. Details of this step have already been discussed in section 4.2.1 and the algorithm can be summarized as follows:

1. Histogram of the given image I_{BRAIN} is generated and the histogram function $h(f)$ is drawn. Mere visual inspection shows a distinct pentamodal nature of the histogram for CSF (H_{CSF}), gray matter (H_{GRAY}), background (H_{BACK}), white matter (H_{WHITE}) and bones (H_{BONE}), distributed progressively in the lighter direction of the gray scale with prominent valleys between adjacent tissue classes.
2. All maxima $h(f_i)$ of the histogram function $h(f)$ and the corresponding gray values f_i are traced.
3. Using each value of $h(f_i)$ in (4.2), a Rayleigh curve $r_i(f)$ is generated initially at each maximum.
4. Similarity of $r_i(f)$ is measured with the original histogram in the range σ_i (Standard deviation) to $2\sigma_i$ using the similarity index proposed by Zijdenbos *et al.*
5. The $r_i(f)$ that corresponds with the highest similarity is considered as the Rayleigh for the noise distribution $r_{noise}(f)$.
6. To get the best fit Rayleigh curve, $r_{noise}(f)$ is scaled by a constant K and a least square fit is performed by minimizing the error expression of (4.4).
7. Lower limit of $r_{noise}(f)$ is considered as the lower limit of the third mode, the image background i.e. H_{BACK} or the upper limit of the second mode i.e. H_{GRAY}.
8. Given the distinct bimodal nature of the distribution upto the upper limit of H_{GRAY} by thresholding proposed by Otsu [78, 79] produces the image of CSF cluster, I_{CSF}

from the original image, I_{BRAIN}. If each discrete set of CSF is denoted as C_i, then I_{CSF} is expressed in (4.5) as

$$I_{CSF} = \coprod_{i=1,n} C_i$$

This tissue classification of CSF along with prior knowledge of anatomy will guide subsequent steps of this model, from determination of the initial estimator to designing of the force field as well as final tuning with region growing.

5.2 Step 2: Automatic Initialization

Initialization is the most crucial part for successful convergence of the deformable model. Close initialization is essential for accurate convergence with minimum computational burden. Fully automatic initialization especially for application like reconstruction of CSF/Gray matter interface is highly challenging. We have addressed this challenge in multistep approach from low level processing of histogram thresholding to incorporation of classical snake to overcome the hindrance of anatomical barriers. The steps are as follows:

5.2.1 Histogram thresholding

At first, third mode of the histogram, that is background (H_{BACK}), is thresholded out automatically using histogram statistics as described in previous section of 5.1. Pixels containing gray values lower than the lower threshold of the background must be part of CSF and the gray matters (Cortical and subcortical) as first and second mode of the histogram are representative of CSF and gray matter respectively. So, mere global thresholding of the entire image with lower threshold of the background produce boundary of the intracranial tissue consisting of CSF and cortical gray matter. Since meninges shares the same gray value as gray matter, the segmented brain contour is encapsulated with meninges of varied thickness. Thus, the brain contour surrounded by CSF and encapsulated by meninges is extracted automatically eliminating the extracranial tissues of bone, fat etc. One pixel thick outer boundary of the meninges, Ω_{MI} serves as the initializing contour for the KWT snake. Logical AND of CSF clusters, I_{CSF} with the original image, I_{BRAIN} forces the entire CSF region to zero instead of a range of gray values in the output image, $I_{BRAIN\text{-}CSF}$. It thus produces a sharp and distinct boundary at the meninges/CSF interface and CSF/gray matter interface with an enhanced gradient. Initialization of the deformable contour is done in $I_{BRAIN\text{-}CSF}$ instead of the original image, I_{BRAIN}. Results of this automated histogram based segmentation of intracranial

tissues bounded by meninges and its one pixel thick outer margin Ω_{MI}, spanning the entire brain from posterior to anterior are shown in Fig 5.2.

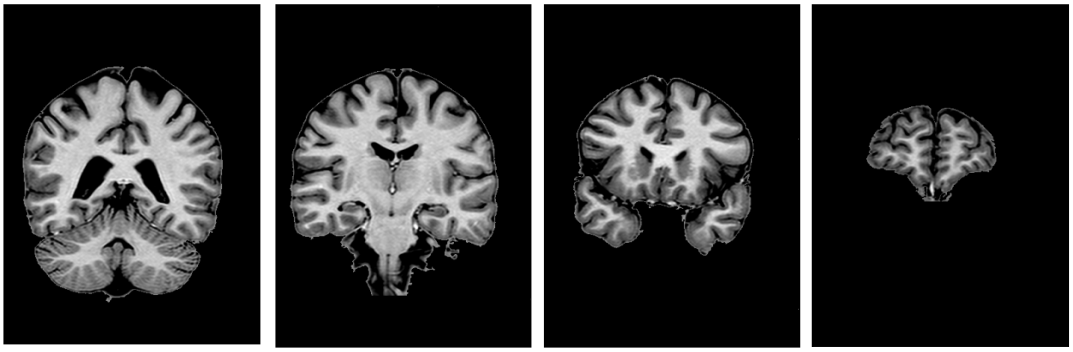

Fig 5.2: Initial contour: Initial contour for deformable model derived by automated histogram based segmentation

5.2.2 Classical snake to remove meninges

Though the tissue specific information, especially the pixel value of specific tissue class is very distinct in the images of the proposed protocol and so evidenced in the image histogram, mere automated thresholding is not enough to segment out the CSF/gray matter interface. Apart from the problem of discontinuity of the cortical boundary, other tissues, namely, meninges share the pixel values of the gray matter. As a consequence, elimination of the meninges becomes the most crucial part to make the reconstruction algorithm fully automatic and accurate. It is done by means of classical KWT snake deformable model in the typical edge based external force field [27].

The basic objective of classical deformable model is to bring the initial contour, Ω_{MI} in the area containing CSF or in other words to drive the initial contour, Ω_{MI} towards inner margins of the meninges that is meninges/CSF interface. For this reason, we have designed an external force field by using topological guidance of distributed CSF derived at step 1. External potential is designed whose local minima coincide with step edges and expressed as

$$\mathrm{E}_{ext}(x,y) = -\left|\nabla I(x,y)\right|^2 \qquad (5.1)$$

In the image $I_{BRAIN\text{-}CSF}$ sharp and distinct boundary at the meninges/CSF interface with an enhanced gradient markedly increases the magnitude of this external force. This external force couples the contour Ω_{MI} which is represented in the image plane $(x,y) \in \Re^2$ as

$v(s) = (x(s), y(s))^{\mathrm{T}}$, where x and y are the coordinate functions and $s \in [0,1]$ in the parametric domain. The shape of the contour is typically determined by variational formulation expressed as

$$\mathrm{E} = \int_s \mathrm{E}_{\mathrm{int}}(v(s)) + \mathrm{E}_{ext}(v(s))ds. \qquad (5.2)$$

The functional can be viewed as a representation of the energy of the contour, and the final shape of the contour corresponds to the minimum of this energy. The first term prescribes the *a priori* knowledge about the model such as its elasticity and rigidity and can be expressed as

$$\mathrm{E}_{\mathrm{int}} = \int_0^1 w_1(s)\left|\frac{\partial v}{\partial s}\right|^2 + w_2(s)\left|\frac{\partial^2 v}{\partial s^2}\right|^2 ds\,. \qquad (5.3)$$

$w_1(s)$ and $w_2(s)$ are the two parameters that dictate the simulated physical characteristics of the contour. In accordance with the calculus of variations, the contour $v(s)$ that minimizes the energy E must satisfy the Euler-Lagrange equation

$$\frac{\partial}{\partial s}\left(w_1 \frac{\partial v}{\partial s}\right) - \frac{\partial^2}{\partial s^2}\left(w_2 \frac{\partial^2 v}{\partial s^2}\right) - \nabla \mathrm{E}_{ext} = 0 \qquad (5.4)$$

A numerical solution of (5.4) is found by discretizing the equation and solving the discrete system iteratively. Fig 5.3 shows the final result of evolution of the classical energy-minimizing snake, Ω_{MF}.

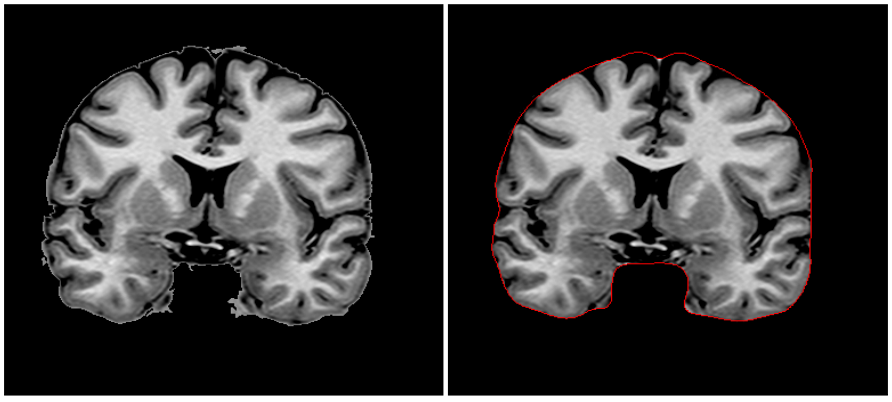

(a) (b)

Fig. 5.3: Removal of meninges: Classical deformable model started with initial contour over outer boundary of the meninges (a) and the final contour, red line in (b) resides over inner boundary of the meninges

5.2.3 Removal of meningeal remnants

This part is designed to overcome the failure of classical energy-minimizing snake in an attempt to eliminate the meninges completely. As meninges have got spatially varied thickness, Ω_{MI} may fail to come completely inside the meninges depending on the sharpness of the edge gradient and the chosen parameters for the internal force. This failure can also be attributable to the property of limited capture range of the classical deformable model. This is most prominent at the saggital sulcal fold. Besides these, in some areas, cortical surface may be attached to the meninges leaving no visible subarachnoid space for CSF. Fig. 5.4 is an example of failure of Ω_{MF} to completely converge at meninges/CSF interface at saggital sulcus.

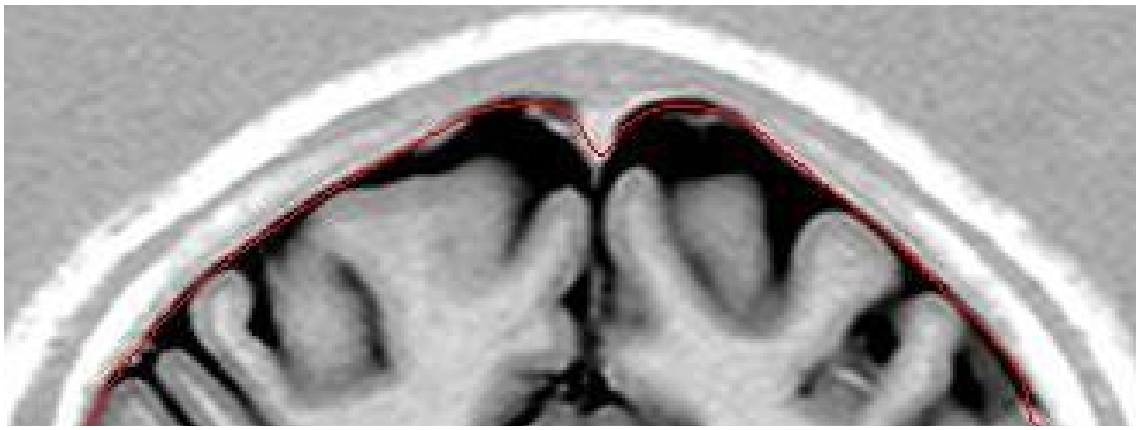

Fig. 5.4: KWT snake trapped in thick meningeal fold

Topological guidance from I_{CSF} along with prior knowledge of neuroanatomy is used to eliminate this thick part of the meninges. Since we have clear distribution of CSF in $I_{BRAIN\text{-}CSF}$, the final contour, Ω_{MF} (shown in red line in Fig. 5.4) of the classical snake is scanned pixel by pixel along its length with inspection of surrounding eight neighbours of each pixel. If any neighbour of the scanned pixel contains a zero pixel value then it is denoted as P_i and it must be part of CSF. Corresponding CSF set is traced by extraction of connected component, X_{Ki} of P_i [83]. If two pixels on the length of the contour, Ω_{MF} are adjacent to the common CSF set, connected component of non-zero pixel value between them is invariably part of meningeal remnant and is turned to zero in order to eliminate those sets. That is, connected component of non-zero pixel value in between P_m and P_n is turned to zero in case of

$$X_{Km} = X_{Kn} \quad (m \neq n) \qquad (5.5)$$

In Fig. 5.5 schematic representation of this problem and the proposed solution has been shown. In Fig. 5.5a initial estimator, Ω_{MI} (yellow pixels) has evolved as the final contour, Ω_{MF} (red pixels) traversing through the meninges (gray pixels), but does not converge with the meninges/CSF (black pixels) interface along its entire length. The Ω_{MF} is scanned along the red line and sets of the non-zero pixels values attached with it are identified as sets of green pixels of meningeal remnants in Fig. 5.5b and turned into zero in Fig. 5.5c.

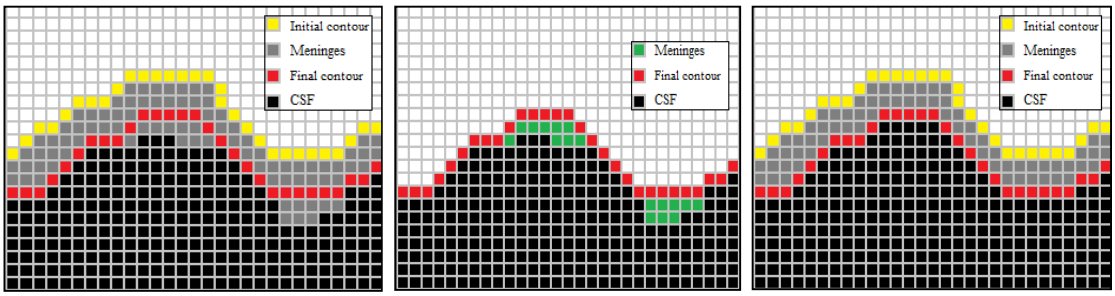

(a) (b) (c)

Fig. 5.5: Schematic representation of the problem in eliminating the thick meningeal fold. (a) shows initial (yellow line) and final contour (red line) of the model of Kass *et. al.* (b) shows the final contour does not converge with the CSF/menigeal interface.

In the thick meningeal fold where the classical snake could not touch the meninges/CSF interface, meningeal remnants are eliminated in this way allowing the cerebrum and cerebellum the only tissue with non-zero pixel value.

5.2.4 Minimum perimeter polygon

At the end of this stage, we have removed extracranial tissues along with meninges from the given brain image, I_{BRAIN}. For this step, we are starting with the images containing only cerebrum and cerebellum as intracranial tissues surrounded by CSF region with the pixel value forcibly set to zero which is bounded by Ω_{MF}. Before implementation of the final hybrid deformable model, presence of the initial estimator must be ensured in the capture range of the force field. As the set of non-zero pixel values is surrounded with the CSF region of uniformly zero pixel value, no force field can be generated in this region with the help of image information only. The contour must be initialized at close proximity of the intracranial brain tissue. For this purpose, boundary of the cluster of non-zero pixel set (containing

cerebrum and cerebellum) residing within Ω_{MF} is approximated by a polygon with a method for finding minimum perimeter polygons proposed by Kim and Sklansky [83, 84]. In this procedure boundary of the cluster is enclosed by a set of two-pixel thick concatenated cells and the boundary is considered as a rubber band contained within the walls of a cell. If the rubber band is allowed to shrink, it produces a polygon of minimum perimeter that fits the geometry established by the cell strip. This minimum perimeter polygon serves as the initial estimator, $\Omega_{INITIAL}$ of the CSF/Gray interface for the deformable model for next step.

5.3 Step 3: Reconstruction of CSF/Gray interface

In this step we will implement a hybrid deformable model to meet the objective of reconstruction of CSF/Gray interface. The basic nature of the deformable model is similar to that of GGVF proposed by Xu et. al., but during its course of evolution, it experiences different external force fields which are also evolving with maturation of the deformable contour. The contour passes different probability spaces to get even into the deep narrow sulcus and finally tuned with region growing for accurate reconstruction of CSF/Gray interface.

5.3.1 Mathematical Basis of the force field

Mathematical foundation of the proposed force field is similar to the energy-minimizing parametric deformable model, but it evolves through a series of external force field instead of single external force field. The external force fields, in turn, evolve along with the evolving contour itself. The contour is represented as $v(s) = (x(s), y(s))^{\mathrm{T}}$ where x and y are the coordinate functions and $s \in [0,1]$ in the parametric domain at a given time in a specific probability space *i* (*i=1,2,...n*). Probability space is designed on the basis of prior knowledge of the application and switched from one to another depending of the predefined controlling parameters based on the maturation of the contour. The shape of the contour is typically determined by variational formulation expressed in (5.2). Here the first term prescribes a *priori* knowledge about the model for a specific probability space and can be expressed as

$$E_{\text{int}} = \int_0^1 \left\{ w1_i(s) \left| \frac{\partial v}{\partial s} \right|^2 + w2_i(s) \left| \frac{\partial^2 v}{\partial s^2} \right|^2 \right\} ds \qquad (5.6)$$

where, $w_{1i}(s)$ and $w_{2i}(s)$ are two parameters that dictate the simulated physical characteristics of the contour in a specific probability space (i). The external force in this model for a specific probability space i is expressed as

$$E_{i.ext} = \sum_{j=1}^{n} \beta_j(\eta) \int_0^1 E_j(v(s))ds \quad (5.7)$$

$E_j(v(s))$ is designed on the basis of prior knowledge about the application for a specific probability space . $\beta_j(\eta)$ is a scaling parameter and the probability space i is updated according to the controlling parameter η which is based on deformation of the parametric contour itself and expressed as

$$\eta = \int_s |v(s)|ds \quad (5.8)$$

The general form of the external force $E_{i.ext}$ is to be adapted according to the application. In our application, it is predesigned with prior knowledge of anatomy and image information according to objectives. Evolution of initial estimator, $\Omega_{INITIAL}$ to the final contour at CSF/Gray matter interface, $\Omega_{CSF\ /\ GRAY}$ requires two probability spaces ($i=1,2$) and the updating criterion of i is $\eta = 0$. It is also assumed in this application that $i=j$. Thus, for two probability spaces the expression (5.7) can be rewritten as

$$E_{i.ext} = \beta_1(\eta) \int E_1(v(s))ds + \beta_2(\eta) \int E_2(v(s))ds \qquad i = 1,2 \quad (5.9)$$

In this application, the first part, $E_1(v(s))=E_{GGVF}$ is defined by the vector field similar to GGVF force field of Xu *et. al*. Construction of this vector field begins from an edge map $f(x,y)$ derived from $I_{BRAIN\text{-}CSF.}$ In our application we have used Canny edge detector [85] to define the edge map with very high gradient at CSF/gray matter interface because of distinct topological guidance of CSF distribution. The gradient of the edge map ∇f has vectors pointing towards the edges, which are normal to the edges. In 2D image plane, the energy functional E_1 can be expressed as

$$E_{GGVF} = \iint g(|\nabla f|)|\nabla v|^2 + h(|\nabla f|)|v - \nabla f|^2 dxdy \quad (5.10)$$

The first term is smoothing term and the second term is data term [12]. Spatially varying weighting functions $g(\cdot)$ and $h(\cdot)$ are designed exactly the same way as GGVF field to maintain the force field in the long, thin indentation like structure where two edges are in close proximity. For better progression of the deformable contour in long, thin indentation along the cortical boundary weighting functions are selected such that $g(\cdot)$ gets smaller as $h(\cdot)$ becomes larger [12, 39, 54]. For this application, the weighting functions are as follows

$$g(|\nabla f|) = \exp - \left(\frac{|\nabla f|}{\kappa_1} \right)^2 \qquad (5.11)$$

$$h(|\nabla f|) = 1 - g(|\nabla f|) \qquad (5.12)$$

The specification of κ_1 determines to some extent the degree of tradeoff between field smoothness and gradient conformity.

The second part, $E_2(v(s))=E_{ZNZD}$ is the newly designed ZNZD vector field, detailed in section IV. Here the data term is designed as a ZNZD map (ϕ) which is a multivariate function of $D_{Z\text{-}NZ}(x,y)$, the distance of a pixel, Z(x,y) with value zero of set C_i from the nearest non-zero pixel with value V ($V \neq 0$) and the corresponding non-zero pixel value (V) in $I_{BRAIN\text{-}CSF}$. A computational diffusion process similar to GGVF is used to extend the vector field beyond the sets of zero pixel values. ZNZD vector field, $v(x,y)$ that minimizes the energy functional is expressed as

$$\begin{aligned} E_{ZNZD} &= \iint m(|\nabla \phi|)|\nabla v|^2 + n(|\nabla \phi|)|v - \nabla \phi|^2 \, dxdy \\ \textit{where} \quad & \phi(x,y) = CV^{-1}|D_{Z-NZ}(x,y)|^2 \\ \textit{and} \quad & m(|\nabla \phi|) = \exp - \left(\frac{|\nabla \phi|}{\kappa_2} \right)^2 \\ \textit{and} \quad & n(|\nabla \phi|) = 1 - m(|\nabla \phi|) \end{aligned} \qquad (5.13)$$

C is a scaling constant and κ_2 behaves similarly as that of GGVF force field. Now, for each probability space, i, sum of these two vector fields, E_{GGVF} and E_{ZNZD} can be expressed as follows:

$$E_{i,ext} = \beta_1(\eta)\iint g\left(|\nabla f|\right)|\nabla v|^2 + h\left(|\nabla f|\right)|v - \nabla f|^2\, dxdy + \beta_2(\eta)\iint m\left(|\nabla \phi|\right)|\nabla v|^2 + n\left(|\nabla \phi|\right)|v - \nabla \phi|^2\, dxdy$$

or

$$E_{i,ext} = \iint \left(\beta_1(\eta)\, g\left(|\nabla f|\right) + \beta_2(\eta) m\left(|\nabla \phi|\right)\right)|\nabla v|^2 + \left(\beta_1(\eta) h\left(|\nabla f|\right) + \beta_2(\eta) n\left(|\nabla \phi|\right)\right)|v - \nabla f|^2\, dxdy \qquad (5.14)$$

$B_1(\eta)$ and $\beta_2(\eta)$ are two scaling functions associated with E_{GGVF} and E_{ZNZD} force field respectively and adjusted according to application. Adjustment of these two scaling functions is discussed in the following curve evolution section for our application. In accordance with the calculus of variations the contour $v(s)$ that minimizes the energy $E_{i,ext}$ must satisfy the Euler-Lagrange equation

$$\frac{\partial}{\partial s}\left(w1_i \frac{\partial v}{\partial s}\right) - \frac{\partial^2}{\partial s^2}\left(w2_i \frac{\partial^2 v}{\partial s^2}\right) - \nabla E_{i,ext} = 0 \qquad (i = 1, 2) \qquad (5.15)$$

5.3.2 Curve evolution

Initial estimator, $\Omega_{INITIAL}$ is automatically derived from the algorithm of minimum polygon of the intracranial brain tissue and it is evolved through two probability spaces with different characteristics of internal force model by satisfying energy minimizing equation of (5.15) under predefined constrains.

Initially, for first probability space (*i=1*) we have $\beta_2(\eta) = 0$ and $\beta_1(\eta) = 1$. Thereby, in this case the external force is defined by the edge map *f(x,y)* as E_{GGVF} only. Propagation of $\Omega_{INITIAL}$ in this force field is determined by Generalized Gradient Vector Flow (GGVF) proposed by Xu. et.al.[12, 39, 54]. With the help of this edge map, GGVF field v is defined as the equilibrium solution of the following vector partial differential equation

$$v_t = \exp\left(-\left(\frac{|\nabla f|}{\kappa}\right)\right)\nabla^2 v - \left\{1 - \exp\left(-\left(\frac{|\nabla f|}{\kappa}\right)\right)\right\}(v - \nabla f) \qquad (5.16)$$

The specification of κ determines to some extent the degree of tradeoff between field smoothness and gradient conformity. The contour is considered as a closed loop throughout its propagation with boundary condition $v(0) = v(1) = 0, v'(0) = v'(1), v''(0) = v''(1)$. After each iteration η is calculated and *i=1* updated to *i=2* when η becomes zero. $\eta = 0$ indicates that there is no further deformation of the deformable contour with further iteration

under influence of the existing force field. In our application, it is solely attributable to the spurious edges at narrow sulcal fold due to partial volume effect. $\Omega_{INITIAL}$ with edge map and intermediate result (Ω_{x}) at the end of the first probability space is illustrated in Fig. 5.6.

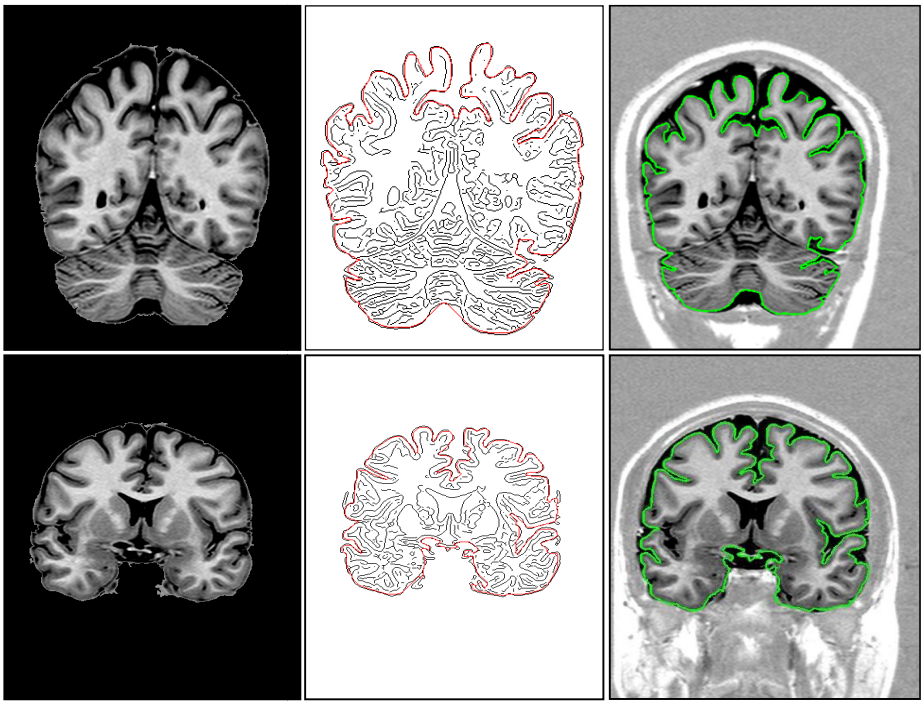

(a) (b) (c)

Fig. 5.6: Propagation in first step: (a) Brain image with meningeal covering, (b) Initial estimator (red line), with canny edge map after removal of non-brain tissues, (c) Intermediate contour (green line) after evolution through first probability space.

For practical purpose deformation of the contour η is measured by the total number of the pixels in the subtracted area between two consecutive iterations. It is determined by XOR logic operation between sets of the pixels of the areas bounded by two consecutive iterations of the contour. In the first probability space, η decreases sharply at initial phase and gradually attains a plateau near zero persistently. The plateau has been determined by the difference of η less than 5 in two consecutive calculations of that parameter. In practice 25 – 30 is the number of iterations for our dataset to meet the criterion. Once η reaches its plateau phase the first probability space is switched to second probability space for further deformation.

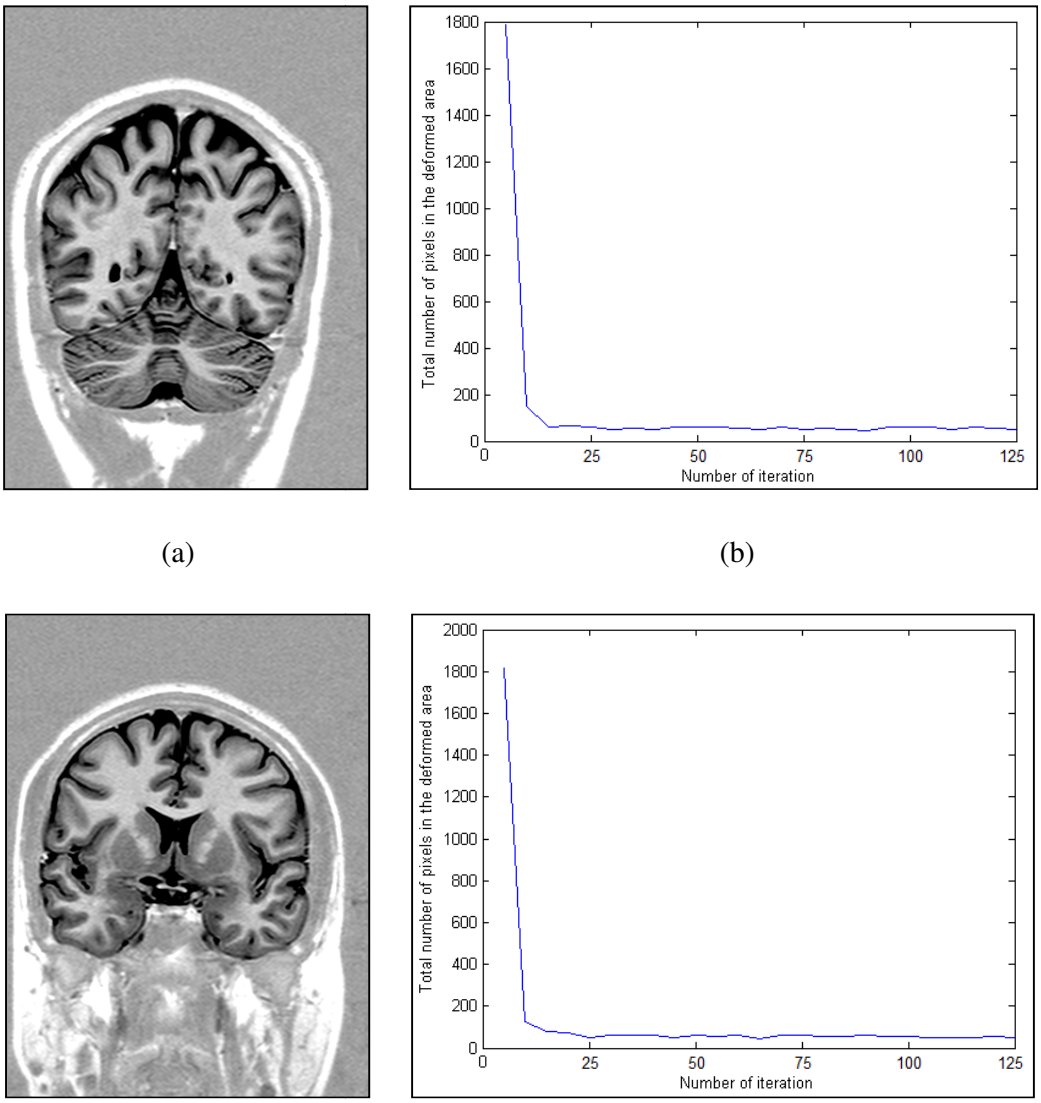

Fig 5.7: Brain image (a) & (c) and their corresponding graph of the parameter η with the number of iteration in the first probability space (b) & (d).

Second probability space is designed to overcome the partial volume effect. For second probability space (i=2), deformable contour is segmented out depending on its geometric features. Using differential geometry, curvature of each point of Ω_x has been determined and lower values are suppressed. Positive and negative signs are assigned to indicate concave and convex points on the contour. Set of concave points (P_c) above the threshold value of

curvature (C_τ) is extracted as target geometric features. A closed interval along Ω_x associated to each concave point P_{ci} is designated as F_i and its length as L_i where

$$F_i = \left[P_{ci} - \frac{L_i}{2}, P_{ci} + \frac{L_i}{2} \right] \qquad (5.17)$$

A local coordinate of F_i is designated as ε which is centred at P_{ci}. Now, only F_i is a deformable contour with boundary condition $v(-1/2) = v(1/2) = 0$ and $v'(-1/2) = v'(1/2) = 0$, while rest of Ω_x remains unaltered. Internal force of the contour for this case can be expressed as

$$\mathrm{E}_{\text{int}} = \int_{-L_i/2}^{L_i/2} w1_2(\varepsilon)\left|\frac{\partial v}{\partial \varepsilon}\right|^2 + w2_2(\varepsilon)\left|\frac{\partial^2 v}{\partial \varepsilon^2}\right|^2 d\varepsilon. \qquad (5.18)$$

In this case it is predefined that $\beta_2(\eta) = 1$ and $\beta_1(\eta) = 0$ for (5.9). Thus, in this case the external force is defined by the ZNZD map $\phi(x,y)$ as E_{ZNZD} only as mentioned in (5.13). A spatially varying constrain force $\rho(\varepsilon)$ is also applied on F_i to push the contour into nearby CSF set C_i, penetrating the spurious edge due to partial volume effect or sampling artifact.

Here $\rho(\varepsilon) = m\varepsilon + a$ where a is a constant and

$$m = \begin{cases} \dfrac{-2a}{L_i} & if \quad \varepsilon > 0 \\ \dfrac{2a}{L_i} & if \quad \varepsilon < 0 \end{cases} \qquad (5.19)$$

Final energy minimizing equation for propagation of F_i in the second probability space is

$$\frac{\partial}{\partial \varepsilon}\left(w1_2 \frac{\partial v}{\partial \varepsilon} \right) - \frac{\partial^2}{\partial \varepsilon^2}\left(w2_2 \frac{\partial^2 v}{\partial \varepsilon^2} \right) - \nabla \mathrm{E}_{ZNZD} - \rho(\varepsilon) = 0 \qquad (5.20)$$

The equation is solved numerically by iteration. Location of P_{ci} and controlling parameter η are checked after every iteration. Contact of P_{ci} with any C_i of I_{CSF} or $\eta=0$ is considered a limiting condition of propagation of corresponding F_i.

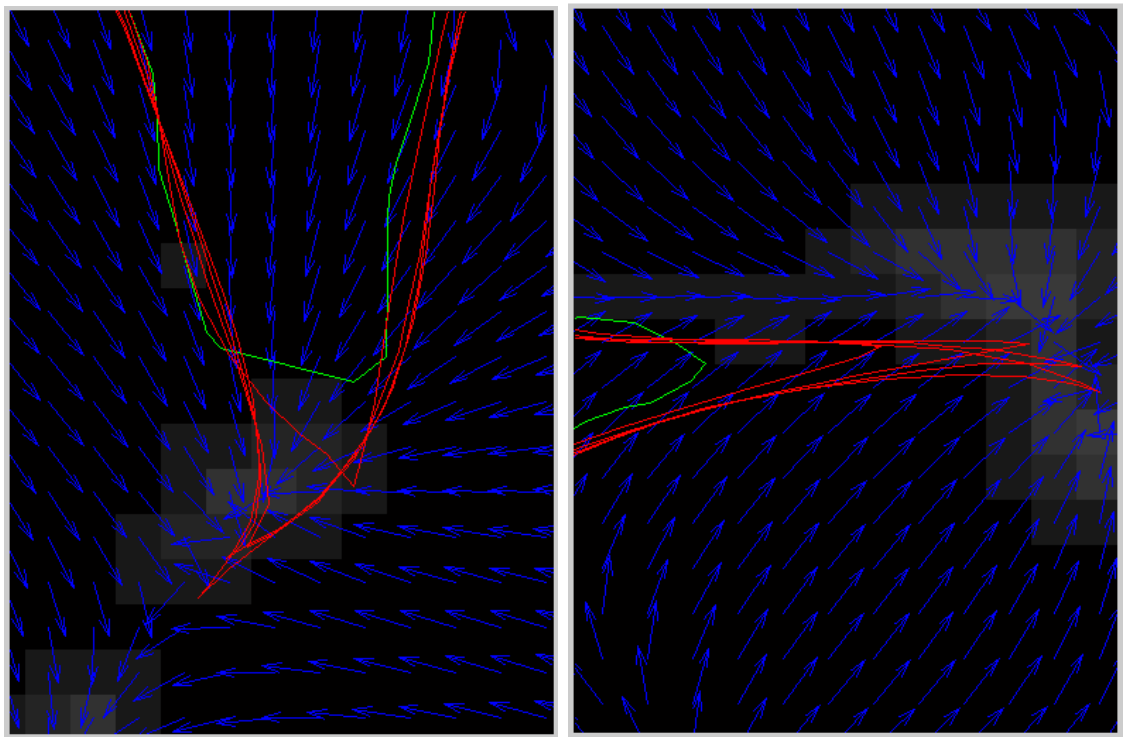

Fig 5.8: Green line is the initial deformable contour (F_i) and red lines are mark of evolution of the contour through ZNZD force field under influence of a spatially varying constrain force $\rho(\varepsilon)$

Gradually, all F_i, initially detached from nearby CSF sets due to spurious edges of partial volume effect, now come to contact with them. Final position of P_{ci} serves as the point of beginning for region filling algorithm [83] to grow Ω_X inside the CSF set only.

Evolution of the deformable contour in second probability space is repeated until propagation of all F_i is restricted by the single criterion $\eta=0$ to get the final contour Ω_{FINAL}. This step confirms overcoming of hindrance from multiple PVE in a single CSF set. Fig. 5.9 compares limitation of the intermediate contour Ω_X after propagation through GGVF force field to overcome PVE and final contour Ω_{FINAL} after propagation through ZNZD force filed and region growing.

5.4 Results

We have applied the AAGHD model for cortical reconstruction at CSF/Gray matter interface to 30 datasets of coronal views of MR image acquired with proposed acquisition protocol.

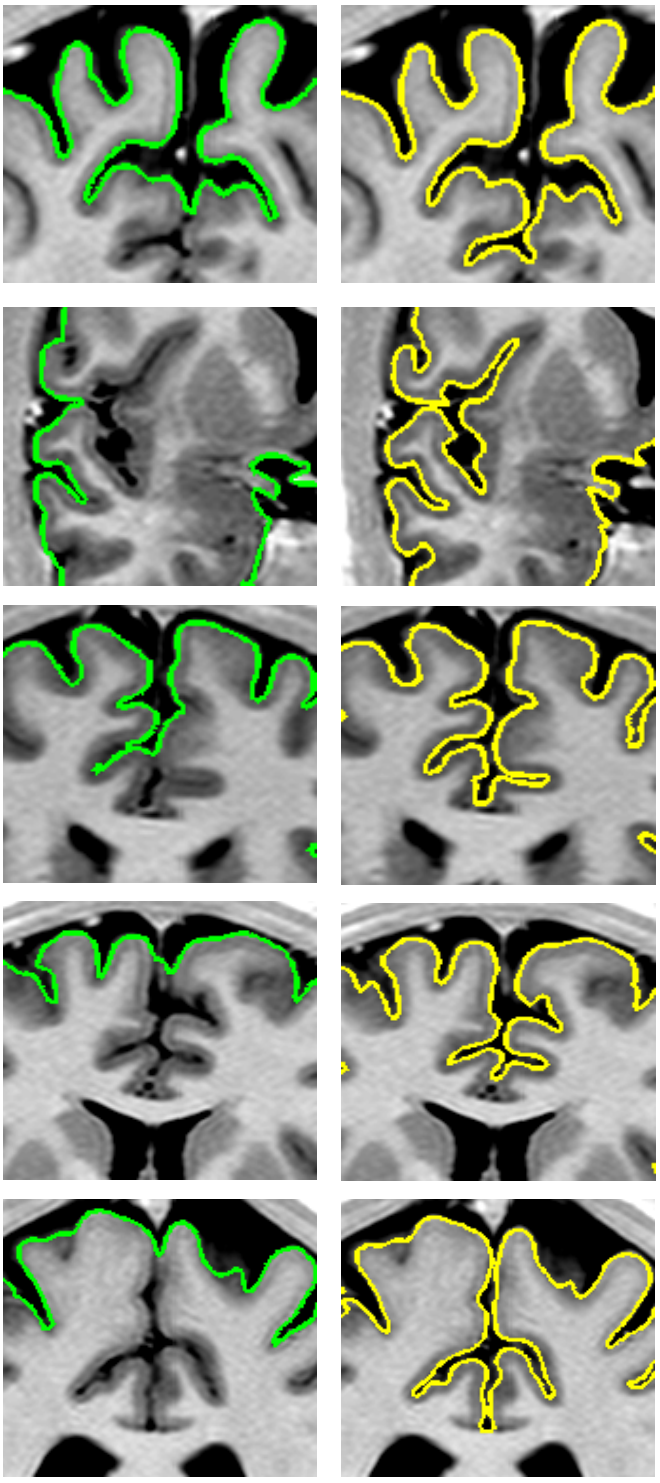

(a) (b)

Fig. 5.9: Evolution of the deformable contour: (a) contour fails to enter into deep sulci due to PVE in first probability space under influence of GGVF field, (b) final result of propagation of the contour into deep sulci beyond PVE under influence of ZNZD force field and region growing operation.

Our AAGHD model is developed only for 2D image and its computations were implemented using MATLAB 7.10.0.499 (R2010a) code. For every N= 384 × 512 pixel image slice on an Intel CORE i3, a typical computation time is 50 seconds. Though a fair number of parameters are to tune in this model, in respect of complete automation, the number of parameters is acceptable and robust as well to change of their values and the image data. Same parameter values are used for all image data sets of 30 subjects and some of the results are produced in the following section. Parameters for traditional KWT snake for removal of non-brain tissue were w_1 =1 and w_2=0; parameters for deformable contour at GGVF force field in the first probability space were $w1_1$ =1, $w2_1$=0 and κ_1=1. We have used Fourier descriptor for smoothening of the contour after convergence at GGVF field to find out the concave points for further propagation at ZNZD field. The parameter for thresholding the curvature, C_τ is 0.2; and parameter for length of the deformable segment, L_i is 3. For deformable contour at ZNZD force field in the second probability space $w1_2$ =0.1, $w2_2$=0.3 and κ_2=1. A spatially varying constraint force is applied over the fragment, F_i with the parameters a=0.5 and m=2. Final outcome of the ZNZD force field and accuracy of the AAGHD model are largely dependent on the above parameters since it is crucial to find out the control points for further propagation of the penetrating part of the contour. We are considering further improvement of performance of the model by making it adaptive in nature.

5.4.1 Qualitative Assessment

Fig. 5.10 shows final results of the reconstructed cortical boundary derived by AAGHD model overlaid on the coronal view of the original brain image. The figure is consisting of coronal slices of a several individuals spanning from anterior to posterior part of the brain. The figure shows that the reconstructed cortical boundary exactly converge with the CSF/Gray matter interface maintaining the entire brain volume as well as detail cortical topology. Excellence of the model reveals in accurate convergence at the deep narrow sulci, namely the lateral sulcus (sylvian fissure) and the central sulcus (Rolandic fissure). Besides propagation of the contour into the deepest part of the sulci, it converges well at other narrow sulci, namely, precentral sulci, postcentral sulci and more. To some extent it also reconstructs the finest detail of the cerebellar folia in the posterior part of the coronal view.

5.4.2 Quantitative Assessment

For validation study, some slices were selected such that the entire brain volume from anterior at one end to posterior at the other was covered. Accuracy and reliability of cortical

Subject1	

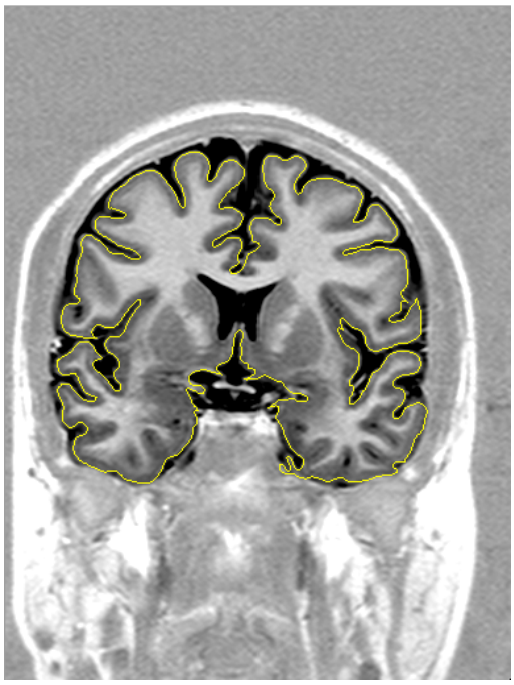

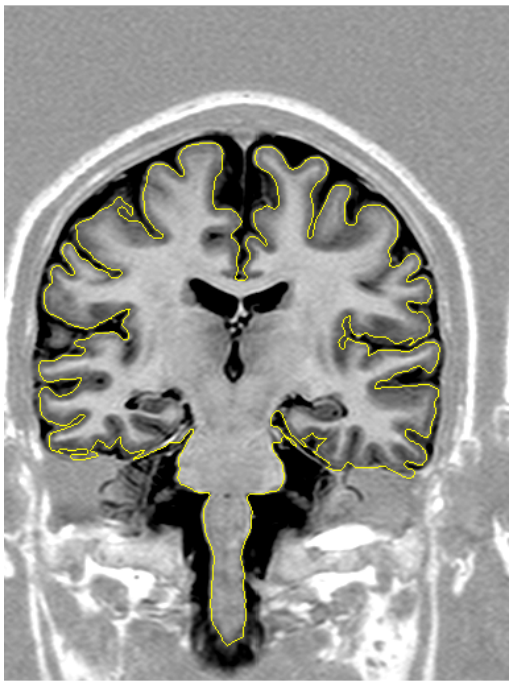

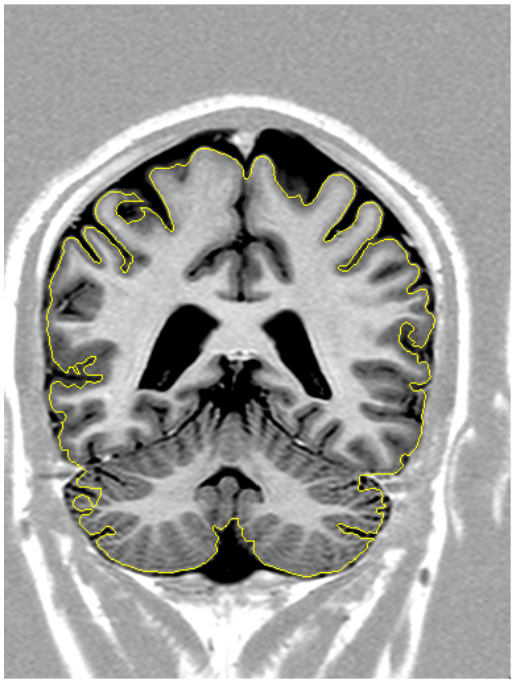

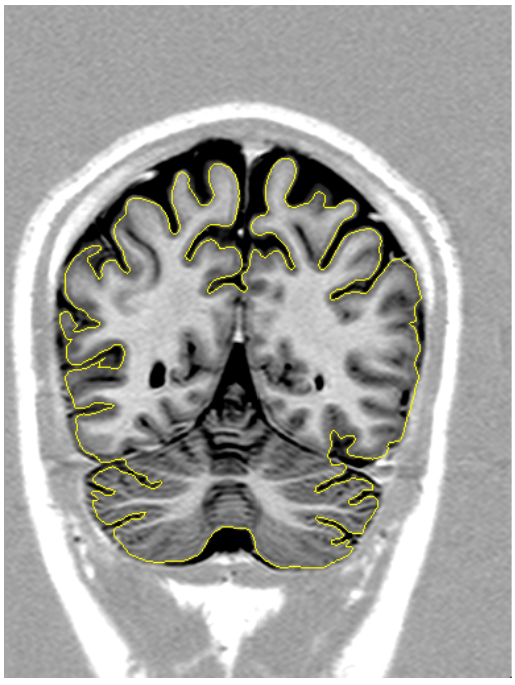

Subject 2	

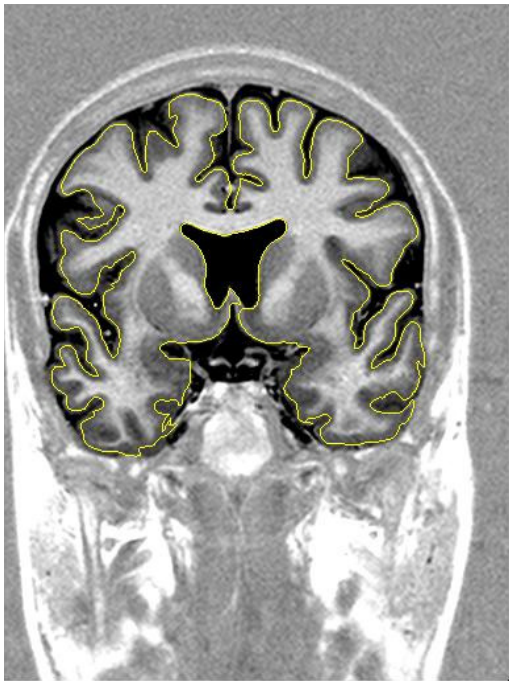

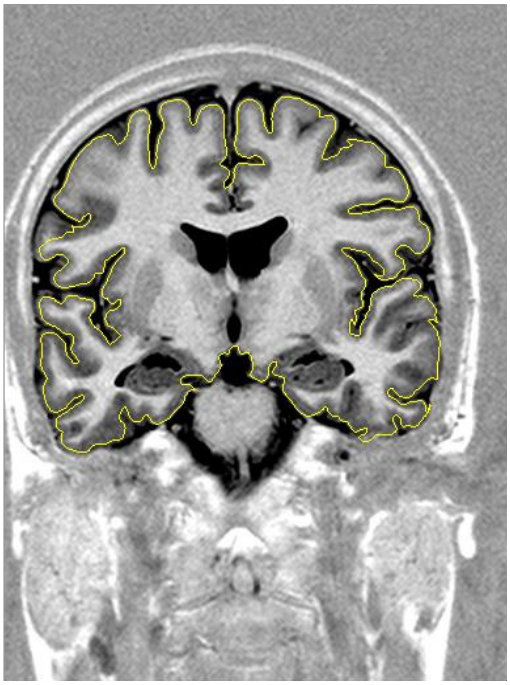

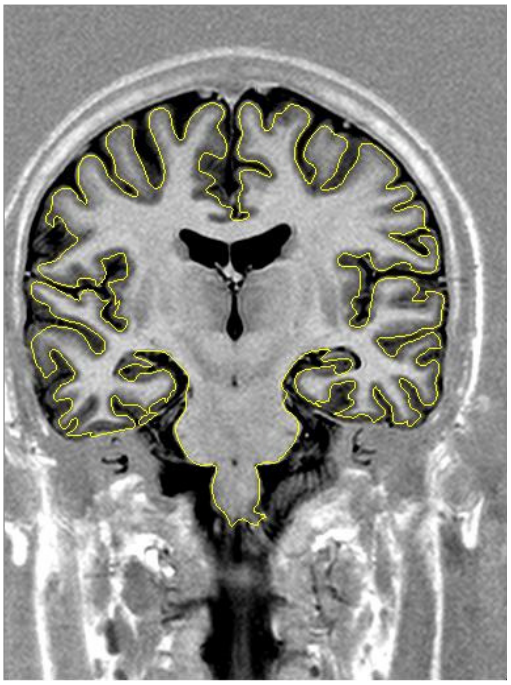

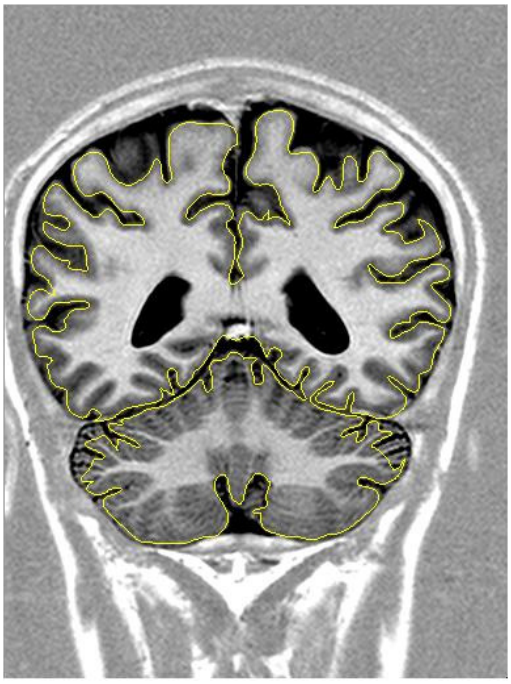

Subject 3	

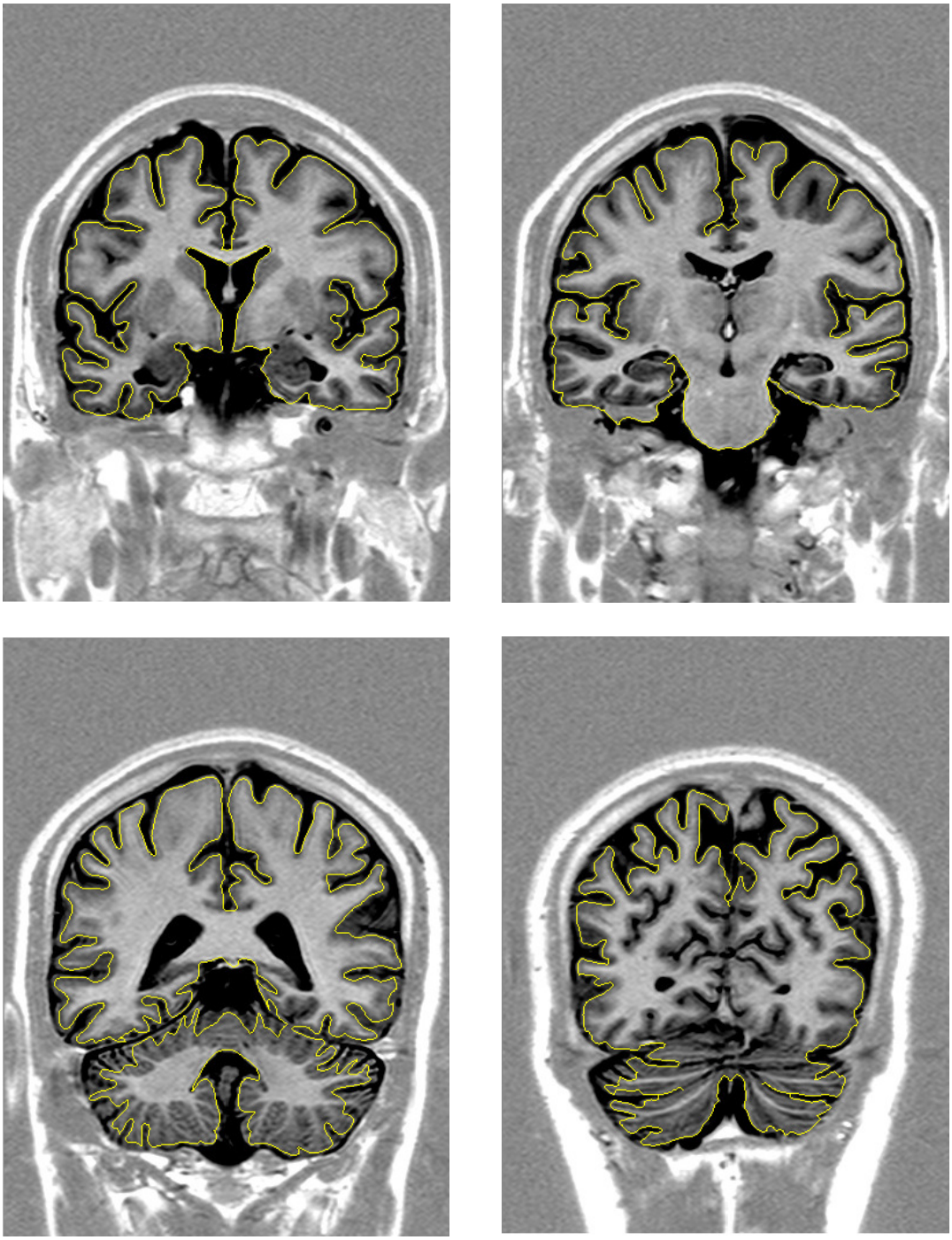

Fig. 5.10: Reconstructed cortical boundary (Yellow line) overlaid on the coronal view of the corresponding MR image

reconstruction with the proposed AAGHD model are computed quantitatively by using two comparison metrics, namely, Dice Similarity Coefficient (DSC) [86, 87] and Symmetrized Hausdorff Distance [88] to manual and automated reconstructed contour.

Dice Similarity Coefficient (DSC):

The DSC value is a simple and useful measure of spatial overlap and applied to study accuracy in image segmentation. The DSC measures the spatial overlap between two segmentations, A and B, of the same target regions, and is defined as

$$\text{DSC}(A,B) = 2(A \cap B)/(A+B) \tag{5.21}$$

Conceptually, the DSC metric is derived from the kappa statistic and commonly used in reliability analysis, when there is a much larger number of background voxels than that of the target voxels, as shown previously by Zijdenbos et al [32].

In our application, a domain expert traced the target manually on each slice and it was compared with the automatically drawn brain contour using DSC. After segmenting coronal view brain images, the manually segmented cortical outer contour was highly comparable to the automated ones and it reflected in high similarity indices, approximately 0.97 ± 0.02. Index for exactly similar patterns is 1 and index of more than 0.700 is considered as very good agreement [41].

Symmetrized Hausdorff Distance:

Examining the surface distances using Hausdorff Distance is another meaningful comparisons between structures as only accuracy of the segmentation boundaries is taken into account [86]. For two non-empty subsets, A and M for automated and manually reconstructed contour respectively, Symmetrized Hausdorff Distance can be expressed as follows:

$$H(A,M) = \max h(A,M), h(M,A). \tag{5.22}$$

where *h(A,M)* is the directed Hausdorff distance and expressed as

$$h(A,M) = \max_{a \in A} \min_{m \in M} d(a,m) \tag{5.23}$$

and *d*(*a, m*) is the euclidean distance between two points on two different contours. *h(M.A)* is also defined similarly. Lower the Hausdorff Distance metric indicates more similarity of the

automated reconstruction to the manual one. This distance for manually segmented cortical contour and the automated reconstructed cortical contour in our data sets is highly encouraging and remains in the range of 1.65 ± 0.31.

5.5 A round up of AAGHD Model

We have tried to meet the basic challenge of reconstructing the outer cortical surface from MR image of brain by developing a novel AAGHD model which is a hybridization of the traditional deformable model with GGVF deformable contour and a newly designed ZNZD deformable model along with prior precise anatomical knowledge. The proposed algorithm claims its excellence in terms of full automation, tuning of minimum number of parameters, accuracy at deep narrow sulci and efficiency in overcoming the partial volume effect. No step of the algorithm, from elimination of bones and soft tissues or initialization of the deformable contour to final convergence at CSF/Gray interface requires any human intervention at all.

Essence of the algorithm emanates from the rich non-overlapping tissue specific information in the acquired datasets. From the image histogram one can easily identify a mode actually representing a given anatomical structure. That is why determination of the initial contour is easily made by global thresholding only. Actually, using global thresholding, segmentation of the brain is possible only because of the high contrast of the adjacent tissues as well as complete control over manipulating it for meeting the objective. As in our dataset pixel values of CSF and gray matter are consistently lower than the background noise, lower threshold of the background is confidently chosen as the upper threshold for segmentation of the initial brain boundary. As the brain is bounded by the bony skull and the background noise never overlaps the distribution of the bones, the chance of misclassification of the bony part as brain is virtually eliminated. The proposed model can not work on images with less tissue contrast as its operation starts on global thresholding on pentamodal distribution of the histogram, which is the feature of proposed acquisition protocol.

The initial brain contour derived in this way is surrounded by CSF and encapsulated by meninges or non-brain tissues with spatially varying thickness. Non-brain tissues are eliminated by using traditional "snake" model and thus the deformable contour is brought to the inner boundary of meninges. To design the external force field for this purpose we again exploit the unique modal distribution feature of specific tissue class in the histogram for

segmentation of topological distribution of Denoting the distributed CSF map with zero and ANDing it with the original image we actually tried to get zero valued CSF and nonzero valued intracranial tissues like cerebrum and cerebellum. This is the most crucial step for success of the algorithm. In this way gradient of CSF/meninges interface and CSF/Gray matter interface become very high which helps in defining the external force field for traditional snake as well as GGVF field in the next step. Besides, it provides precise anatomical guidance for eliminating thick meningeal folds which cannot be removed by the traditional snakes. Though some zero valued CSF remain distributed in the ventricles, being far away from the cortical gray matters they do not affect the following steps of the algorithm anyhow.

Final contour of the traditional snake, Ω_{MF} is scanned pixel by pixel for its adjacency to the zero-valued CSF. In case of any thick isolated meningeal fold, final contour of the traditional snake passes arbitrarily through mid portion and may not be adjacent to CSF. But the first and the last pixel of the fold must be adjacent to the same CSF set. On checking this condition after tracing these extreme points, non-zero set in between is identified and turned to zero value to eliminate it. This situation is more vivid around superior sagittal sinus. This checking is made strategically not to affect the part of the cortical folds which are attached to the meninges leaving no CSF in between them. Thus all discrete non-zero valued meningeal folds turn into zero selectively and the brain remains a set of non-zero value. Polygon of minimum perimeter of that set serves as initial contour, $\Omega_{INITIAL}$ for GGVF deformable model and this initialization ensures starting of the deformable contour in the capture range of the force field. In our GGVF model, we have chosen a pair of weighting function for better convergence of boundary concavity which is very important for our application to reconstruct the highly convoluted cortical surface, proposed by Xu *et. al*. The GGVF field computed using this pair of weighting functions will conform to the edge map gradient at strong edges, but will vary smoothly away from the boundary. In spite of the medialness of the GGVF deformable model, in this application, the final contour perfectly lies over CSF/gay matter interface, since the contour faces a very high gradient at this interface when approached externally. This has occurred due to anatomical guidance of CSF distribution. Instead of having a range of gray values, distributed CSF possesses zero gray value and the gray matter distribution in the gray scale is far away from zero. This produces a very high gradient at their interface and helps in convergence on that interface.

As the deformable contour approaches from the outside, it inevitably faces hindrance due to the PVE especially at narrow sulci. AAGHD model strategically handles this problem automatically and selectively. It switches its external force field from GGVF to ZNZD field, when deformation under influence of GGVF halts according to the guiding parameter η. The new force field is used for fine tuning of the shape of the contour selectively for penetration of the contour at narrow sulcal folds. It does not work on the entire contour; rather selective part of the contour is marked with the help of differential geometry as a fraction or segment adjacent to the concave points of the contour. Spatially varying extra penetrating force is applied over this segment. It is maximum at the central concave point and decreasing linearly on both sides of the selected segment. It augments penetration of the contour through PVE in association with ZNZD force field. The main essence of the ZNZD force field is sensitivity to the PVE. Being a function of the pixel value of spurious edges at the site of the PVE, the force field is spatially varying and allows penetration of the contour through spurious edges formed by the PVE at narrow and adjacent gray matter folds only. This force field never pushes the contour towards boundary; rather attracts the contour at the centre of the nearby CSF set. So, a different strategy has to be applied to push it again toward the boundary. Once the AAGHD model switches from GGVF to ZNZD field there is no need to switch again to GGVF field on seizing deformation in ZNZD field as GGVF is meant for coarse tuning of the contour and ZNZD is meant for fine tuning. But it has to be checked whether any deformation is possible on application of the ZNZD force field repeatedly to overcome multiple obstructions of the PVE at a single CSF set. The contour is finalized as Ω_{FINAL} when no deformation is possible at all at any site on application of ZNZD field after running the region growing algorithm at the sites deformed under influence of ZNZD field in previous attempts. The contour accurately converges with the CSF/Gray interface maintaining cortical topology along with the entire brain volume.

PART VI
CONCLUSION

CHAPTER 6

CONCLUSION AND PERSPECTIVES

CONTENTS

6.1 Synthesis of Contributions

6.1.1 Novel MR image acquisition protocol

Huge advancement in neuroimaging and brain image processing in last few decades has opened many specialized application areas in research and clinical practice beyond conventional role of visualization of anatomical lesion in diseased individuals. Computational neuroanatomy, brain warping, reconstruction of cortical and subcortical structures of brain, image guided neurosurgery and above all localization of functional data in the structural image to explore the neuroanatomical correlation with a precise cognitive task are a few such examples of advanced applications. In biomedical imaging, MRI has extraordinary versatility for generating images of a wide range of different tissues by means of contrast. Though many protocols have been proposed for acquisition of MR image of brain for clinical practice, not one has been standardized for advanced research application like cortical reconstruction or multimodal image registration or brain warping. As a consequence, no standard post-hoc processing has been established for specific application. Besides validation of the final result of such processing tasks are not unquestionable even after huge computational burden and varied amount of manual intervention. Once the objective has been designed, it is imperative that planning of image acquisition and image processing run side by side. To address this problem, our research was aimed to improve the quality of MR image of brain at the

acquisition level going beyond the conventional acquisition protocols. The acquisition protocol was conceptualized from FLAIR or STIR protocols to suppress the signal from the gray matter for better delineation of cortical and subcortical gray structures in normal brain. In our approach, attempts towards optimization of the parameters have developed Gray Matter Attenuated Inversion Recovery protocol which has produced brain images with brilliant gray-white contrast, measured objectively and with comparative histogram analysis. Different tissue classes are distributed in separate modes in the histogram because of their non-overlapping pixel values and this feature is highly promising for post-hoc processing of tissue classification and segmentation with minimum computational burden.

6.1.2 Head segmentation algorithm

Though segmentation of head by means of removal of background is not the integral part of cortical reconstruction or the proposed AAGHD model, it can be done as an intermediate step of the algorithm for a specific application. The proposed algorithm is an improvement on the conventional background removal technique proposed by Brummer *et al*. [71] for MR image of brain and is invariant to image acquisition protocols. As image histograms vary wildly with acquisition protocols, modification is necessary in the algorithm for automatic threshold selection and even the question of feasibility of such automated thresholding may appear in some cases. In their algorithm Brummer *et al.* searched the background noise peak in the histogram by finding the local maxima. Search is proposed to be started from the least intensity level. That is why, when the image is distributed arbitrarily in the lower intensity range than the background noise intensity, the strategy of finding the local maxima may get trapped in the local maxima of the image itself and the image background will remain unidentified. The algorithm proposed by Brummer *et al.* is limited to those images which produce background noise distribution in the lower intensity range with object intensity always higher than the background noise in their histogram. This limitation is also evident in the work of Atkins and Mackiewich [71, 72].

In our datasets background noise is distributed in the intermediate intensity range when image intensity partially drops below the background intensity and partially above that range. So, two thresholds (upper and lower) are to be generated automatically for complete segmentation of the image. But the primary challenge is to identify the peak of the background in such types of histograms. The challenge becomes apparently insurmountable

as neither the histogram p.d.f. is monotonically increasing upto the noise peak nor the noise peak coincides always with the global maxima of the histogram. So, search for the local or global maxima is not enough to address the present problem. As the resulting image histogram of the proposed protocol shows part of the histogram for CSF (H_{CSF}), gray matter (H_{GRAY}), background (H_{BACK}), white matter (H_{WHITE}) and bones (H_{BONE}) are distributed progressively in the lighter direction of the gray scale with prominent valley in between two adjacent tissue classes, automated multilevel thresholding of this histogram can produce the specific tissue class. To determine the CSF distribution for AAGHD model, lower level of the third mode, H_{BACK} is to be found out automatically as background removal algorithm mentioned in part IV. Automated multilevel thresholding of the image with the lower limit and the upper limit of the best fit Rayleigh curve, *r(f)* as mentioned in section IV, segment out the image background efficiently.

In our datasets, background noise and image actually overlap unlike in the test image of the conventional algorithm. Still the algorithm performs efficiently, because noise intensity can never be similar to the intensity value of the cranial boundary that is the bony skull. Intracranial soft tissue may possess the same value of the background noise but the skull is always markedly different form the background noise. For this reason, variable amount of intracranial region is segmented out during segmentation of the head contour. Since boundary of the cranium is well preserved the intracranial portion can easily be retrieved by morphological filling operation. Though the results of the presented algorithm for segmentation of head contour invariant to the datasets are highly encouraging, it has to be asserted that the potentiality of the algorithm is solely dependent on the potentiality of the similarity index.

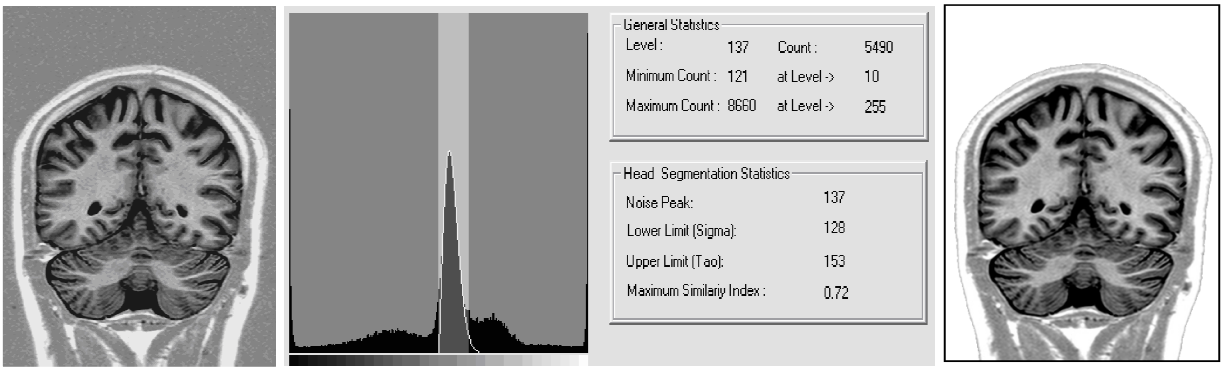

Fig. 6.1: Multilevel thresholding for removal of image background

6.1.3 Novel external force field

We have introduced a novel external force field named Zero-Non-Zero Distance (ZNZD) force field for reconstruction of outer cortical surface that is CSF/Gray matter interface of brain from MR image. The force is designed to address the problem of propagation of the deformable contour across the spurious edge due to partial volume effect at narrow sulci when the contour is initialized outside the cortical surface. This force field is designed with a function of the distance between CSF and the brain tissue instead of conventional gradient of edge map. This force field drives only the deep penetrating part of the contour for fine tuning with the deep sulci. The basic difference of the field with other deformable model is that it never converges with the desired object boundary; it just breaks the barrier of spurious edges. Being function of the pixel value of the obstructing pixels of the spurious edges, the field has got an inherent property to be spatially varying in its strength depending on the image information.

6.1.4 Fully automated cortical reconstruction algorithm

In this thesis we have studied different deformable models aiming to develop a fully automated algorithm for cortical reconstruction without loss of brain volume. In section V, we detail the algorithm which is named as Advanced Anatomy Guided Hybrid Deformable Model (AAGHD). Novel approaches of this model includes initialization of the deformable contour at outside of the cortex then stepwise application of different force field namely GGVF force field of Xu et. al. and a newly developed ZNZD force field in automatic fashion depending on the global deformation of the contour. Initialization algorithm includes histogram statistics to eliminate background and bones and deformable model of Kass et. al. to eliminate other non brain tissue like meninges. Uniqueness of the algorithm includes extensive usage of the anatomical guidance in the form of CSF distribution for accurate convergence with the CSF/Gray interface, complete automation from elimination of the non-brain tissues through initialization of the contour, propagation and switching among different force field to final convergence at the true cortical surface. Performance of the algorithm measures quantitatively with a similarity index proposed by Zijdenbos *et al.* [73] derived from the reliability measures and quantifies the agreement between two measures. We have used this measure since it is sensitive to both size and location and weights heavily the common area between overlapping regions.

6.2 Future Work

Though the algorithm is fully automated and addressed the challenge of accurate convergence to narrow deep sulci, scope of future work includes making some heuristic parameters more adaptive in nature to increase robustness of the algorithm. As the algorithm is efficient on the 2D image to reconstruct the cortical outline as a deformable curve, it has to be extended to voxel based approach in 3D image data to reconstruct the cortical surface as deformable surface. The main essence of the algorithm that is incorporation of prior knowledge of anatomy with deformable models can be extensively used for reconstruction of subcortical gray matters namely thalamus, caudate nucleus, amygdale, hippocampus and more. As detailed analytical description is preserved in the reconstructed cortical map, study of different sulcal folds can be done with help of this algorithm. Above all, as entire brain volume is preserved, localization of the functional data in this reconstructed cortical surface will help to study the relationship between structure and function quantitatively.

It is also noteworthy, that the proposed model can also be extended into the domain of machine learning. The constraints of prior knowledge or curve evolution strategy can be treated as completely supervised learning process. The adaptive learning process can be introduced to accommodate cross subject cortical variability, instead of incorporating more anatomical constraints or rigorous curve evolution strategy. Adaptive machine learning can also be applied for automated detection of cortical sulcal folds. However, machine learning for automatic detection of anatomical features and structural pathology is highly attractive domain of future research. For instance, IBM Watson has already been initiated for automatic medical diagnosis by using deep learning.

6.3 Overall Perspectives

The main goal of the work presented in this thesis is to develop an algorithm for fully automated but accurate reconstruction of the cortical surface by fusing different deformable models, developing new models along with precise application of anatomical guidance as constraints. This idea of fusion of existing algorithms is also reflected in the work of computer vision researcher Monique Thonnat, who has combined the best features of existing algorithms using human interactions [89]. We aim to reconstruct the cortical surface at CSF/Gray matter interface to maintain the entire brain volume with analytical description of the detail topology without any human interaction. For this purpose we address the challenge

of partial volume effect at deep and narrow sulcal folds to converge the contour exactly on the true surface of CSF/Gray matter interface. We also aim to nullify human interactions to make the algorithm fully automated from pre-processing, elimination of non-brain tissue, initialization of the contour, curve propagation to final convergence. It is hoped that the algorithm has explored efficiently the use of anatomical knowledge with the deformable models to fulfil the objective and encourage in extending the application of automated cortical reconstruction to other domain of neuroimaging like morphometric analysis, warping, structural-functional correlation and more.

6.4 Publications

International Conference

[1] "Accurate cortical reconstruction in narrow sulci with a novel external force field"; *17th International Conference on Medical Image Processing and Analysis 2015, WASET, Dubai, UAE*

[2] "Anatomy guided hybrid deformable model for reconstruction of brain cortex from MR image"; *CompBio'10, IASTED Technology Conference 2010, Cambridge, Massachusetts, USA*

[3] "High Resolution MR Image of Brain With Signal Attenuation of Gray Matter"; *IST 2010, IEEE Instrumentation and Measurement Society, Thessaloniki, Greece*

[4] "A New Segmentation Technique for Brain and Head from High Resolution MR Image Using Unique Histogram Features", *IPTA2010 (IEEE & EURASIP), Paris, France*

[5] "Segmentation of MR Image of Brain: A New Method Using Unique Histogram Features and Prior Knowledge of Brain Anatomy", *IPCV 2010, WORLDCOMP, Las Vegas, Nevada, USA*

[6] "An improved algorithm for automated segmentation of the head contour from MR image", *VIIP 2009, IASTED Cambridge, UK*

Communicated to International Conference

[1] "A novel external force for propagation of deformable contour into deep sulci of brain for fully automated cortical reconstruction from MR image", *BIOIMAGING 2016 (SCITEPRESS digital library), Rome, Italy*

Communicated to International Journal

[1] "Gray Matter Attenuated Inversion Recovery (GrAIR) for High Contrast MR Image of Brain"; *Journal of Magnetic Resonance Imaging, Wiley online library, Online ISSN: 1522-2586*

APPENDIX A

NMR Phenomenon and MR image signal

Source of signal for MRI is externally measured NMR phenomenon. NMR involves ***N***uclei of an object to be imaged, ***M***agnetic field generated by imager and ***R***esonance phenomenon due to interaction of nuclei with the magnetic field. Nuclei with odd atomic weights and/or odd atomic numbers (e.g. H^+), posses an angular momentum $\vec{J}$, called "spin". In MRI, an ensemble of the nucleic of the same type present in an object is referred to as a (nuclear) Spin system. Property of this spin system is that nuclear magnetism can be created by placing it in an external magnetic field.

Nuclear Magnetic Moments (μ)

A microscopic magnetic field (analogues to microscopic bar magnet) is associated with a nuclear spin. This is the basis of nuclear magnetism of a nuclear spin system. This microscopic magnetic field is represented as vector $\vec{\mu}$, nuclear magnetic dipole moment or magnetic moment, where

$$\vec{\mu} = \gamma \vec{J} \qquad \text{A.1}$$

γ is Gyromagnetic ratio. Its unit is rad/S/T and its value is nucleus dependent. A related constant is $\gamma = \gamma / 2\pi$ (unit is MH_Z/T). For ^1H $\gamma = 42.58$ MH_Z/T

Magnitudes of $\vec{\mu}$

As per theory of quantum mechanics values of nuclear *spin quantum number* (I) depends on mass number and charge number of a nuclei and it may be $0, \frac{1}{2}, 1, \frac{3}{2}, 2, \frac{5}{2}$.

$$|\vec{\mu}| = \mu = \gamma \hbar \sqrt{I(I+1)} \qquad \text{A.2}$$

Where, h is Plank's constant, $\hbar = \frac{\hbar}{2\pi}$ its value is $(6.6\times10^{-34}\ J-s)$. In a sample, nuclei with I =1/2 (e.g. for ^{1}H, ^{13}C, ^{19}F, ^{31}P), the spin system is called 'Spin- ½' system. A nucleus is NMR active if and only if $I \neq 0$

Direction of $\vec{\mu}$

Direction of $\vec{\mu}$ is completely random in the absence of B_o due to thermal random motion. So, no net magnetic field exists around a macroscopic object. To activate macroscopic magnetization the spin vector is to be line up by exposing the object to external static magnetic field B_o applied in z direction.

$$\vec{B}o = B_o\,\vec{k} \qquad \text{A.3}$$

Direction of $\vec{\mu}$ after exposure to is B_o reoriented. As per quantum model, $\vec{\mu}$ can assume one of a discrete set of orientation but not exactly with the direction of the external magnetic field. If μ_Z is the z-component of $\vec{\mu}$ in 3-D space and m_I is magnetic quantum number, then

$$\mu_Z = \gamma m_I \hbar \qquad \text{A.4}$$

If $I \neq 0$, then $m_I = -I, -I+1, -I+2, \ldots\ldots, I$ a set of (2I +1) values. So, there is (2I +1) possible orientation for $\vec{\mu}$ with respect to $\vec{B_o}$. The angle θ between $\vec{\mu}$ and $\vec{B_o}$ can be calculated as follows

$$Cos\theta = \frac{\mu_Z}{\mu} = \frac{\gamma m_I \hbar}{\gamma \hbar(\sqrt{I\ (I+1)})} = \frac{m_I}{\sqrt{I\ (I+1)}} \qquad \text{A.5}$$

$\vec{\mu}$ is quantized along the direction of the external field. Direction of $\vec{\mu}_{xy}$ (Transverse component) remains random and angle between $\vec{\mu}_{xy}$ and μ_x, ξ is random variable, distributed over [0,2π]

$$\vec{\mu}_{xy} = \mu_x\,\vec{i} + \mu_y\,\vec{j}$$

$$\begin{cases} \mu_x = \left|\vec{\mu}_{xy}\right| \cos\xi \\ \mu_y = \left|\vec{\mu}_{xy}\right| \sin\xi \end{cases}$$

Magnitude of $\vec{\mu}_{xy}$ is

$$\left|\vec{\mu}_{xy}\right| = \sqrt{\mu^2 - \mu_z{}^2} = \gamma\hbar\sqrt{I(I+1) - m_I{}^2} \qquad \text{A.6}$$

For Spin-1/2 system, I=1/2 and m_I = +/- ½, then $\theta = \pm 54^\circ 44'$ according to equation A.5 and $\left|\vec{\mu}_{xy}\right| = \frac{\gamma\hbar}{\sqrt{2}}$ according to equation A.6. That is, for spin-1/2 system any μ takes 1of 2 possible orientations, pointing up or parallel and pointing down or antiparallel. Now, motion of $\vec{\mu}$ in B_0 can be calculated according to classical mechanics. The torque that $\vec{\mu}$ experiences from the B_0 is

$$\begin{aligned} &\vec{\mu} \times B_o \vec{k} = \frac{d}{dt}(\vec{J}) \\ &or \frac{d\vec{\mu}}{dt} = \gamma\vec{\mu} \times B_o k \end{aligned} \qquad \text{A.7}$$

Thus precession of $\vec{\mu}$ about the Z axis (B_0 field) is called *nuclear precession.* It is clockwise in direction and its angular frequency is called Larmor frequency, ω_0

$$\omega_0 = \gamma B_0 \qquad \text{A.8}$$

Nuclear precession can be expressed as

$$\mu(t) = R_Z(\omega_0 t)\mu(0) \qquad \text{A.9}$$

Where, $R_Z(\omega_0 t)$ is a rotation matrix and can be expressed as $\begin{bmatrix} \cos(\omega_o t) & \sin(\omega_o t) & 0 \\ \sin(\omega_o t) & \cos(\omega_o t) & 0 \\ 0 & 0 & 1 \end{bmatrix}$

Bulk Magnetization

Collective behavior of $\vec{\mu}$ can be describe by macroscopic magnetization vector $(\overrightarrow{M})$. It is the vector sum of all the microscopic magnetic moment in the object.

$$\overrightarrow{M} = \sum_{n=1}^{N_S} \vec{\mu}_n \qquad \text{A.10}$$

N_S is the total number of spin in the system. For Spin -½ systems, μ_n takes parallel and/or antiparallel orientations with respect to z-axis. Spin in different orientation have different energy of interaction with B_0. As per quantum theory energy E can be expressed as

$$E = -\vec{\mu} . \overrightarrow{B}_0 = -\gamma m_I \hbar B_0 \qquad \text{A.11}$$

For parallel spin, m_I= ½ and their energy $E_\uparrow = -\frac{1}{2}\gamma\hbar B_o$ and for antiparallel spin, m_I = - ½ and their energy $E_\downarrow = \frac{1}{2}\gamma\hbar B_o$. So, spin down is the higher energy state than spin up. This energy difference expressed as

$$\Delta E = E_\downarrow - E_\uparrow = \frac{1}{2}\gamma\hbar B_0 - (-\frac{1}{2}\gamma\hbar B_0) = \gamma\hbar B_0 \qquad \text{A.12}$$

If $\Delta E \neq 0$, there is two states for a spin system. This phenomenon is called Zeeman splitting phenomenon. The spin population difference in this two spin states is related to their energy difference by the following Boltzmann Relationship

$$\frac{number\ of\ up\ spin}{number\ of\ down\ spin} = \frac{N\uparrow}{N\downarrow} = \exp\left(\frac{\Delta E}{KT_s}\right) \qquad \text{A.13}$$

Where K is the Boltzmann constant and its value is 1.38×10^{-23}J/k and T_s is the absolute temperature (273+t). As in practice $\Delta E << KT_s$

$$\left(\frac{\Delta E}{KTs}\right)^n \approx 0 \quad n>1 \text{ (integers)}.$$

$$\therefore \exp\left(\frac{\Delta E}{KTs}\right) \approx 1 + \frac{\Delta E}{KTs} + \left(\frac{\Delta E}{KTs}\right)^2 / 2! \ldots\ldots\infty$$

$$\approx 1 + \frac{\Delta E}{KTs} = \left(1 + \frac{\gamma \hbar B_o}{KTs}\right)$$

So,

$$\frac{N_\uparrow}{N_\downarrow} = 1 + \frac{\gamma \hbar B_0}{KTs}$$

$$\frac{N_\uparrow - N_\downarrow}{N_\uparrow + N_\downarrow} = \frac{KTs + \gamma\hbar B_0 - KTs}{KTs + KTs + \gamma\hbar B_0}$$

$$N_\uparrow - N_\downarrow = Ns \frac{\gamma\hbar B_0}{2KTs + \gamma\hbar B_0}$$

$$N_\uparrow - N_\downarrow = Ns \frac{\gamma\hbar B_0}{2KTs} \quad [\ \gamma\hbar B_0 << KTs\ ]$$

If it is positive, then $N_\uparrow > N_\downarrow$. This uneven distribution occurs as spin is more likely to take the lower energy state with higher stability. Though $(N_\uparrow - N_\downarrow)$ is very small, it generates an observable macroscopic magnetization vector $(\vec{M})$ from a spin system. Such spin system is said to be magnetized. Difference between number of pointing up spin and pointing down spin is essential to produce macroscopic magnetization vector.

Magnitude and direction of the bulk magnetization

$$M = M_x \vec{i} + M_y \vec{j} + M_z \vec{k} = \left(\sum_{n=1}^{Ns} \mu_x, n\right)\vec{i} + \left(\sum_{n=1}^{Ns} \mu_y, n\right)\vec{j} + \left(\sum_{n=1}^{Ns} \mu_z, n\right)\vec{k}$$

Again, $\sum_{n=1}^{Ns} \mu_x, n = \mu_{xy} \sum_{n=1}^{Ns} \cos\xi_n = 0$. As projection of $\vec{\mu}_n$ onto the transverse plane has a random phase while it precesses about z- axis, 'ξ_n' is a random variable uniformly

distributed over [0, 2π]. In the same way $\sum_{n=1}^{Ns} \mu_y, n = 0$, and macroscopic magnetization can be expressed as $M = \left(\sum_{n=1}^{Ns} \mu_z, n \right) \vec{\kappa}$. For spin-½ system $\mu_Z = +\frac{1}{2}\ \gamma\hbar$ for parallel spins and $\mu_Z = -\frac{1}{2}\ \gamma\hbar$ for antiparallel spins. Then the expression becomes

$$M = \left(\sum_{n=1}^{N\uparrow} \frac{1}{2}\ \gamma\hbar - \sum_{n=1}^{N\downarrow} \frac{1}{2}\ \gamma\hbar \right) \vec{\kappa} = \frac{1}{2} \gamma\hbar \left(N_{\uparrow} - N_{\downarrow} \right) \vec{\kappa}$$

Now, putting the value of $\left(N_{\uparrow} - N_{\downarrow}\right) = Ns\ \frac{\gamma\hbar B_0}{2KTs}$ we can get the magnitude for spin -½ systems as follows

$$M_z^{\circ} = \left| \vec{M} \right| = \frac{1}{2} . \gamma\hbar . N_s \frac{\gamma\hbar B_o}{2kTs} = \frac{\gamma^2 \hbar^2 B_o Ns}{4kTs}$$

General form of this expression for Spin-I is given as

$$M_z^{0} = \frac{\gamma^2 \hbar^2 B_o\ \ NsI\,(I+1)}{3KTs} \qquad \text{A.15}$$

Direction of this bulk magnetization at equilibrium state is towards positive direction of z – axis.

RF Excitation and resonance

Bulk magnetization, M is pointing along the B_o. So, for spin -1/2 system in B_o, large no of spins will be set of vectors spreading out two precessing cones. Resonance means establishment of phase coherence among these 'randomly' precessing spins. For this purpose, an external force has to be applied to make the phase coherent. For magnetized spin system, the external force comes from an oscillating magnetic field $\vec{B}_1(t)$ (Transmitter coil of RF

System). To induce a coherent transition of spin for one energy state to another, radiation energy (ΔE) is to be equals to the applied energy by RF system, E_{rf}. If the excitation carrier frequency is ω_{rf}, as per Plank's law, applied energy by RF system $E_{rf} = \hbar\ \omega_{rf}$. For resonance condition,

$$\Delta E = \gamma \hbar B_o = \hbar \omega_{rf}$$
$$\omega_{rf} = \gamma B_o = \omega_o \qquad \text{A.16}$$

RF pulse is a synonymous of B_1 field. It is called "Pulse" as B_1 field is short lived (duration is of ms). It is called "RF" as B_1 field oscillates in radio frequency range. B_1 is very very less than B_o. B_1 field is linearly polarized as it oscillates along the x- axis and it generates an oscillating $\overrightarrow{B_1}(t)$ field perpendicular to $\overrightarrow{B_o}$ field.

$$B_1(t) = B_1^{\ e}(t)\, e^{-i(\omega_{rf} t + \psi)} \qquad \text{A.17}$$

Initial phase angle (Ψ) is constant and exerts no effect on excitation result. The envelop function, $B_1^{\ e}(t)$ uniquely specifies shape and duration of RF pulse and excitation property. RF pulses are named on it. As for example of an rectangular pulse,

$$B_1^{\ e}(t) = B_1 \Pi\left(\frac{t - \tau_p / 2}{\tau_p}\right) = \begin{cases} B_1 & 0 \le + \le \tau_p \\ 0 & otherwise \end{cases} \qquad \text{A.18}$$

The Bloch Equation

Bulk magnetization, *M* is a function of t when B_1 is applied. This time-dependent behavior of $\overrightarrow{M}$ has been quantified by Bloch equation and its general form is

$$\frac{d\overrightarrow{M}}{dt} = \gamma \overrightarrow{M} \times \vec{B} - \frac{M_x \vec{i} + M_y \vec{j}}{T_2} - \frac{(M_Z - M_Z^{\ 0})\vec{k}}{T_1} \qquad \text{A.19}$$

T1 and T2 are time constant for relaxation.

Free precession and relaxations

After perturbation of $\overrightarrow{M}$ from its thermal equilibrium state by an RF pulse, if enough time is given, $\overrightarrow{M}$ returns to previous state as per laws of thermodynamics. This precession of $\overrightarrow{M}$ about B_o field is called *free precession.* Free precession consists of two parts, recovery of M_Z, known as *longitudinal relaxation* and destruction of M_{xy}, known as *Transverse relaxation.* Time evolution for the transverse and longitudinal magnetization components in larmor rotating frame are as follows:

$$M_{x'y'}(t) = M_{x'y'}(0_+)\, e^{-t/T_2}$$
$$M_{z'}(t) = Mz^0(1 - e^{-t/T_1}) + M_{z'}(0_+)\, e^{-t/T_1} \qquad \text{A.20}$$

$M_{x'y'}$ and $M_{Z'}$ are transverse and longitudinal component of bulk magnetization after application of RF pulse. Decay of $M_{x'y'}$ and recovery of $M_{z'}$ both follows an exponential function. This exponential description especially for $M_{x'y'}$ is only applicable for weak spin-spin interaction system, e.g. spin in liquid state molecular. In other cases it is more complicated. Theoretically total time taken for complete destruction of $M_{x'y'}$ is prolonged. But, total regain of Mz^0 is much faster. Theoretically it is more or less instantaneous. But $M_{z'}(0_+)e^{-t/T_1}$ component has a negative impact on $M_{Z'}(t)$, which make the exponential curve much smother than M_{xy} decay curve. T_1 is not the total time taken for longitudinal relaxation and T_2 is not the total time taken for transverse relaxation. After T_1 time interval $M_{Z'}$ will regain 63% of $M_Z{}^0$ and after T_2 time interval $M_{x'y'}$ will lose 37% of M_{xy}. T_1 and T_2 values depend on tissue composition, structures and surrounding. In MRI rotating magnetization of NMR is converted to electrical signals.

Bibliography

[1] Tim McInerney and Demetri Terzopoulos, “Deformable models in medical image analysis: a survey,” *Medical Image Analysis*, 1(2), pp. 91-108, 1996

[2] Stanley Osher, Nikos Paragios, Geometric Level set methods in Imaging, Vision, and Graphics, Springer-Verlag, 2003

[3] Isaac N. Bankman, *Handbook of Medical Imaging Processing and analysis,* Academic Press, 2000

[4] Herbert Goldstein, *Classical Mechanics, Second Edition*, Addition-Wesley/Narosa Indian Student Edition, 1985

[5] S. Osher and J. Sethian, “Front propagating with curvature-dependent speed: Algorithms based on the Hamilton-Jacobi formulation”, Journal of Computational Physics, 79: 12-49, 1988

[6] Arthur W. Toga, *Brain Warping*, Academic Press, 1999

[7] D. Terzopoulos and H. Quin, “Dynamic NURBS with geometric constraints for interactive sculpting”. ACM transaction on Graphics, 13: 103-136, 1994

[8] El-Baz, Acharya, Mirmehdi and Suri, *Multi Modality State-of-the-Art Medical Image Segmentation and Registration Methodologies: Volume 1, Chapter 2*, Springer Science+Business Media, LLC 2011

[9] M J T FitzGerald and Jean Folan-Curran, *Clinical Neuroanatomy and Related Neuroscience, Fourth Edition*, W.B. Saunders, 2002

[10] Richard S. Snell, *Clinical Neuroanatomy for Medical Students, Fourth Edition*, Lippincott-Raven, 1997

[11] Zhi-Pei Liang, & Paul C. Lauterbur, *Principle of Magnetic Resonance Imaging – A signal processing perspective*. IEEE Press, 2000.

[12] C. Xu, “Deformable Models with Application to Human Cerebral Cortex Reconstruction from Magnetic Resonance Images”, Ph.D. thesis, The Johns Hopkins University, Baltimore, MD, January 1999

[13] G. E. Christensen, S. C. Joshi and M. I. Miller, "Volumetric Transformation of Brain Anatomy", *IEEE Transactions on Medical Imaging, 16(6),* pp.864-877, 1997

[14] Chris A. Davatzikos, "Spatial transformation and registration of brain images using elastically deformable models", *Computer Vision and Image Understanding,* 66, pp. 207-222, 1997

[15] W. E. L. Grimson, G. J. Ettinger, T. Kapur, M. E. Leventon, W. M. W. III and R. Kikinis, "Utilizing segmented mri data in image-guided surgery", *Int. J. Pattern Recog. Artif. Intell., 11(8),* pp. 1367-1397, 1996

[16] M. Vaillant, C. Davatzikos, R. H. Taylor and R. N. Bryan, "A path-planning algorithm for image-guided neurosurgery", in *Lecture Notes in Comp. Sci.: CVRMed-MRCAS'97*, 1205, pp.467-476, 1997

[17] S. Joshi, J. Wang, M. I. Miller, D. C. V. Essen and U. Grenander, "On the differential geometry of the cortical surface," in *Proc. Of the SPIE: Vision Geometry IV*, 2573, pp. 304 - 311, Aug. 1995

[18] L. D. Griffin, "The intrinsic geometry of the cerebral cortex", Journal of Theoretical Biology, 166(3), pp. 261-273, 1994

[19] A. M. Dale and M. I. Sereno, "Improved localization of cortical activity combining EEG and MEG with MRI cortical surface reconstruction: A linear approach", *Journal of Cogn. Neuroscience,* 5(2), 162-176, 1993.

[20] H. A. Drury and D. C. V. Essen, "Functional specializations in human cerebral cortex analyzed using the visible man surface-based atlas", *Human Brain Mapping,* 5, pp.233-237, 1997

[21] J. Talairach and P. Tournoux, *"Co-planar stereotaxic atlas of the Human brain, 3-Dimensional proportional system: An approach to cerebral imaging".* Stuttgart, NY: Thieme Medical Publishers, Inc., 1988

[22] F. L. Bookstein, Principal warps: Thin-plate splines and the decomposition of deformations, IEEE transaction on Pattern Anal. Machine Intell., 11(6), 567-585, 1989

[23] C. Davatzikos, Spatial normalization of 3-D images using deformable models, Journal of Computer Assisted Tomography, 20(4), 656-665, 1996

[24] P. M. Thompson and A. W. Toga, Detection, Visualization and animation of abnormal anatomic structure with a deformable probabilistic brain atlas based on random vector field transformations, Medical Image Analysis, 1(4), 271-294, 1997

[25] R. Kikinis, M.E. Shenton, G. Gerig, H. Hokama, J. Haimson, B.F. O'Donnell, C.G. Wible, R.W. McCarley and F.A. Jolesz, Temporal lobe sulco-gyral pattern anomalies in schizophrenia: An in vivo MR three-dimensional surface rendering study, Neuroscience letters, 182, 7-12, 1994

[26] J. Moussai, B.A. Anvar, K.L. Narr, A.F. Cannestra, P.M. Thompson, T. Sharma and A.W. Toga, Three-dimentional analysis of lateral ventricles in schizophrenia, 4th Int. Conf. On Human Brain Mapping, NeuroImage, 7(4): S505.

[27] M. Kass, A. Witkin and D. Terzopoulos, "Snakes: Active contour models", International Journal of Computer Vision, 1(4), pp. 321-331, 1988

[28] Scott Acton and Nilanjan Ray, Biomedical Image Analysis: Segmentation, Morgan and Claypool Publishers, 2009

[29] M. A. Gennert and A. Y. Yuille, "Determining the optimal weights in multiple objective function optimization," in *Proceedings, 2nd International Conference on Computer Vision*, pp.87–89, 1988.

[30] Somojit saha, Rohit K. Chatterkee, Sarit K. Das, Avijit Kar, "Anatomy Guided Hybrid Deformable Model For Reconstruction of Brain Cortex From MR Image" *CompBio 2010, IASTED Cambridge, Massachusetts, USA* pp. 599-606, 2010

[31] X. Ge, X. Ge, and J. Tian, "An automatic active contour model for multiple objects," in

Proceedings of the International Conference on Pattern Recognition, 2002.

[32] C. Li, J. Liu, and M. D. Fox, "Segmentation of external force field for automatic initialization and splitting of snakes," *Pattern Recognition*, vol. 38, pp. 1947, 2005.

[33] B. Li and S. T. Acton, "Automatic active model initialization via Poisson inverse gradient," *IEEE Transactions on Image Processing*, vol. 17, pp. 1406–1420, 2008.

[34] A.A. Amini, T.E. Weymouth, R.C. Jain, Using dynamic programming for solving variational problems in vision, Pattern Analysis and Machine Intelligence, IEEE Transactions on, 12(9), 855-867, 1990

[35] V. Caselles, C. Francine, C. Tomeu and D. Francoise, A geometric model for active contours in image processing, Numerische Mathematik, 66, 1-31, 1993

[36] R. Malladi, J.A. Sethian, B.C. Vemuri, Shape modelling with front propagation: a level set approach, Pattern Analysis and Machine Intelligence, IEEE Transactions on, 17 (2), 158-175, 1995

[37] S. Kichenassamy, A. Kumar, P. Olver, A. Tannenbum, A. Yezzi, Gradient flow and geometric active contour model, IEEE Fifth international conference on computer vision, 810-815, 1995

[38] V. Caselles, R. Kimmel, G. Sapiro, Geodesic Active Contours, International Journal of Computer Vision, 22(1), 61-79, 1997

[39] C. Xu and J.L. Prince, Snakes, Shapes, and Gradient Vector flow, IEEE transaction on Image Processing, 7(3), 359-369, 1998

[40] N. Ray, S. T. Acton, T. Altes, E. E. de Lange, and J. R. Brookeman, "Merging parametric active contours within homogeneous image regions for MRI-based lung segmentation," *IEEE Transactions on Medical Imaging*, 22(1) 189–199, 2003

[41] B. Li and S. T. Acton, "Active contour external force using vector field convolution for image segmentation," *IEEE Transactions on Image Processing*, 16, 2096–2097, 2007

[42] L.D. Cohen and I. Cohen, Finite element methods for active contour models and ballons for 2D and 3D images, IEEE Transaction on Pattern Analysis and Machine Intelligence, 15(11), 1131-1147, 1993

[43] N. Rougon and F. Preteux, Deformable markers: Mathematical morphology for active contour models control, In Image Algebra and Morphological Image Processing II, volume 1568 of SPIE Proc., 78-89, Bellinggham, WA: SPIE

[44] J.M. Gauch, H.H. Pien and J. Shah, Hybrid boundary-based and region-based deformable models for biomedical image segmentation, In Mathematical methods in Medical Imaging III, volume 2299 of SPIE proc., 72-83, San Diego, CA:SPIE.

[45] A. Chakraborty and J.S. Duncan, Game theoretic integration for image segmentation, IEEE transaction on Pattern Analysis and Machine Intellegence, 21(1), 1999

[46] C.S. Poon, M. Braun, R. Fahrig, A. Ginige and A. Dorrell, Segmentation of medical images using an active contour model incorporating region-based images features, In Robb, 90-97, 1994

[47] I.L. Herlin, C. Nguyen and C. Graffigne, A deformable region model using stochastic processes applied to echocardiographic images. IEEE Computer society Conf. Computer Vision and Pattern Recognition (CVPS'92), 534-539, 1992

[48] T. Chen, D. Metaxas, Image segmentation based on the integration of markov random fields and deformable models, International Conference on Medical Imaging Computing and Computer-Assisted Intervention, 2000

[49] S. Zhu and A. Yuille, Region competition: unifying snakes, region growing and Bayes/MDL for multi-band image segmentation, IEEE transaction on Pattern Analysis and Machine Intellegence, 18(9), 884-900, 1996

[50] R. Ronfard, Region-Based strategies for active contour models, International Journal of Computer Vision, 13(2), 229-251, 1994

[51] S.R. Gunn and M.S. Nixon, A robust snake implementation, a dual active contour, IEEE transaction on Pattern Analysis and Machine Intellegence, 19(1), 1997

[52] Tim McInerney and Demetri Terzopoulos, "T – snakes: Topology adaptive snakes", Medical Image Analysis, 4, 73-91, 2000

[53] S. Bischoff and L.P. Kobbelt, Parameterization free active contour models with topology control, The visual computer, 2004

[54] C. Xu and J.L. Prince, Generalized gradient vector flow external forces for active contours, An International Journal of Signal Processing, 71(2), 132-139, 1998

[55] D. MacDonald, D.Avis and A. C. Evans, "Multiple surface identification and matching in magnetic resonance images," in SPIE Proc. VBC'94, 2359, 160-169, 1994

[56] J.F. Mangin, V. Frouin, I. Bloch, J. Regis and J. Lpez-Krahe, From 3D Magnetic Resonance Images to Structural Representations of the Cortex Topography using Topology Preserving Deformations, Journal of Mathematical Imaging and Vision, 5, 297-318, 1995

[57] Chris A. Davatzikos and Jerry L. Prince, "An Active Contour Model for Mapping the Cortex", *IEEE Transactions on Medical Imaging*, *14*(1), 65-80, 1995

[58] Chris A. Davatzikos and R. N. Bryan, "Using a deformable surface model to obtain a shape representation of cortex", *IEEE Transactions on Medical Imaging*, *15*(6), 785-795, 1996

[59] T. Kapur, W. Grimson, W. Wells and R. Kikinis, "Segmentation of brain tissue from magnetic resonance images", *Medical Image Analysis, 1, 109-128, 1996*

[60] P. C. Teo, G. Sapiro and B. A. Wandell, "Creating connected representations of cortical gray matter for functional MRI visualization", *IEEE Transactions on Medical Imaging*, *16*(6), 852-863, 1997

[61] C. Xu, D. L. Pham, M. E. Rettmann, D. N. Yu and J. L. Prince, "Reconstruction of the human cerebral cortex from magnetic resonance images", *IEEE Transactions on Medical Imaging*, *18*(6), 467-480, 1999

[62] X. Zeng, L. H. Staib, R.T. Schultz and J. S. Duncan, "Volumetric Layer segmentation using coupled surface propagation" in Computer vision and Pattern Recognition, pp. 708-715. IEEE Comp. Soc., Los Alamitos, 1998

[63] X. Zeng, L. H. Staib, R.T. Schultz and J. S. Duncan, "Segmentation and measurement of the cortex from 3D MR images using coupled surface propagation", *IEEE Transactions on Medical Imaging*, *18*(10), 100-111, 1999

[64] M. Vaillant and C. Davatzikos, Finding parametric representations of the cortical sulci using an active contour model, Medical Image Analysis, 1(4), 295-315, 1996

[65] X. Zeng, L.H. Staib, R.T. Schultz, H. Tagare, L. Win and J.S. Duncan, A new approach to 3D sulcal ribbon finding from MR Images, Medical Image Computing and Computer-Assisted Intervention – MICCAI'99, Lecture Notes in Computer Science Volume 1679, pp 148-157, 1999

[66] R.H. S. Carpenter, "*Neurophysiology*", Arnold, Fourth edition, 2003

[67] Scott A. Huettel, Allen W. Song, Gregory McCarthy, Functional Magnetic Resonance Imaging, 2nd Edition. Sinauer, 2009.

[68] Beutel, Kundel, Van Metter, Handbook of Medical Imaging, Vol 1. Physics and Psychophysics. SPIE Press, 2000

[69] Robert R. Edelman, John R. Hesselink, M. B. Zlatkin, Hohn V. Crues III, Clinical Magnetic Resonance Imaging. 3rd Edition, Vol 1, Saunders, Elsevier, 2006.

[70] Peter Jezzard, Paul M. Mathews, Stephen M. Smith, Functional MRI: An introduction to Methods, Oxford University press, 2001

[71] Marijn E. Brummer, Russell M. Mersereau, Robert L. Eisner, & Richard R. J. Lewine, Automatic Detection of Brain Contours in MRI Datasets, *IEEE Transactions on Medical Imaging,* 12(2), pp.153-166, 1993

[72] M. S. Atkins, & B. Mackiewich, Fully automatic segmentation of the brain in MRI, *IEEE Transactions on Medical Imaging*, 17(1), pp. 98-107, 1998

[73] A. Zijdenbos, B. Dawant, R. Margolin, & A. Palmer, Mophometric analysis of white matter lesions in MR images: Method and Validation, *IEEE Transactions on Medical Imaging*, *13*(4), 716-724, 1994

[74] John J. Bartko, Measurement and Reliability: Statistical Thinking Considerations, *Schizophrenia Bulletin, 17*(3), 483-489, 1991

[75] Somojit Saha, Sarit K. Das, Avijit Kar, "High Resolution MR Image of Brain With Signal Attenuation of Gray Matter"; *IST, IEEE Instrumentation and Measurement Society, Thessaloniki, Greece*, pp. 311-315, 2010

[76] Somojit Saha, Sarit k Das, Avijit Kar; "Segmentation of MR Image of Brain: A New Method Using Unique Histogram Features and Prior Knowledge of Brain Anatomy," *IPCV , WORLDCOMP, Las Vegas, Nevada, USA,*2010

[77] Somojit Saha, Sarit k Das, Avijit Kar; "A New Segmentation Technique for Brain and Head from High Resolution MR Image Using Unique Histogram Features," *IPTA (IEEE & EURASIP), Paris, France,* 2010

[78] N. Otsu "A threshold selection method from gray level histogram", IEEE transaction on systems, man, and cybernetics, SMC 9, pp 62-66, 1979

[79] R. M. Haralick and L. G. Shapiro, "Computer and Robot Vision, vol. 1, Addison-wesley Publishing company, 1992

[80] Somojit Saha, Sarit k. Das, Subhajit Das, Avijit Kar; "An improved algorithm for automated segmentation of the head contour from MR image", *VIIP, IASTED Cambridge, UK,* pp. 25-32, 2009

[81] M. Henkelman, "Measurement of signal intensities in the presence of noise in MR images", *Medical Physics*, *12*(2), pp. 232-233, 1985

[82] B.K.P. Horn and B.G. Schunk, Determining Optical Flow, Artificial Intelligence, 17, 185-203, 1981

[83] Rafael C. Gonzalez, & Richard E. Woods, *Digital Image Processing* 2nd ed. (Prentice-Hall, 2002)

[84] C. E. Kim and J. Sklansky, "Digital and cellular convexity," *Pattern recognition*, 15(5), pp. 359-367, 1982

[85] J. F. Canny, "A computational approach to edge detection," IEEE Transaction on Pattern Analysis and Machine Intelligence," 8(6), pp. 679-698, 1986

[86] Kelly H. Zou, Simon K. Warfield, Aditya Bharatha, Clare M.C. Tempany, Michael R. Kaus, Steven J. Haker, William M. Wells, III, Ferenc A. Jolesz, and Ron Kikinis, "Statistical Validation of Image Segmentation Quality Based on a Spatial Overlap Index," *Acad Radiol*, 11(2), pp. 178-189, 2004

[87] Dice LR. "Measures of the amount of ecologic association between species," Ecology 26, 297–302, 1945

[88] Ali R. Khana, Lei Wangb, and Mirza Faisal Bega, "FreeSurfer-Initiated Fully-Automated Subcortical Brain Segmentation in MRI Using Large Deformation Diffeomorphic Metric Mapping", *Neuroimage*, 41(3), pp. 735-746, 2008

[89] http://www-sop.inria.fr/members/Monique.Thonnat/#publications